SYNTHESIS AND CHARACTERIZATION OF ZINC OXIDE-TITANIUM DIOXIDE NANOCOMPOSITES CO-DOPED WITH DYSPROSIUM AND EUROPIUM

by

Sefako John Mofokeng

(BSc Hons)

A thesis submitted in partial fulfilment of the requirements for the degree

MAGISTER SCIENTIAE (NANOSCIENCE)

in the

Faculty of Natural and Agricultural Sciences

Department of Physics

at the

University of the Free State

Republic of South Africa

Supervisor: Prof. O.M. Ntwaeaborwa

Co-Supervisor: Prof. R.E. Kroon

January 2016

Declaration

(i) “I, Sefako John Mofokeng, declare that the Master of Science Degree research thesis or interrelated, publishable manuscripts/published articles, or coursework Master of Science Degree mini-thesis that I herewith submit for the Master of Science Degree qualification at the University of the Free State is my independent work, and that I have not previously submitted it for qualification at another institution of higher education.”

(ii) “I, Sefako John Mofokeng, hereby declare that I am aware that the copyright is vested in the University of the Free State.”

(iii) “I, Sefako John Mofokeng, hereby declare that all royalties as regards intellectual property that was developed during the course of and/or in connection with the study at the University of the Free State will accrue to the University.”

In the event of a written agreement between the University and the student, the written agreement must be submitted in lieu of the declaration by the student.

Signature Date

--- ---

Acknowledgements

- ✓ First and foremost, I would like to give thanks to God, Almighty for strength, wisdom and his grace to help me complete this research. With Him, nothing is impossible and without Him I would not have the wisdom and physical abilities to do it especially in difficult times.

- ✓ My deepest gratitude goes to Prof. O.M. Ntwaeaborwa for having accepted to be my supervisor and his encouragement, support and esteemed guidance through the course of this study. Without his good nature and proper supervision, my studies would have not been possible.

- ✓ Special thanks to Prof. R.E. Kroon, my co-supervisor for his support, valuable comments and generous contribution of knowledge during the course of my study.

- ✓ It is my pleasure to express deepest thanks to Dr. Vinod Kumar for introducing me to various synthesis methods and characterization techniques during my experimental work. Most importantly, I thank him for his patience, guidance and suggestions during my experimental work.

- ✓ Many thanks to staff in the Physics Department, members of Ntwaeaborwa Research Group (NRG) and Post-Doctoral students for their assistance and valuable inputs in this study.

- ✓ I am grateful for the MSc nanoscience program (NNPTTP) of South Africa and the financial support from the Department of Science and Technology (DST), National Research Foundation (NRF) and the University of the Free State (UFS).

- ✓ A special mention of thanks to my friends (David Mbongo, Teboho Patrick Mokoena, Pule Edmond Motsepe, Dumisane Vincent Mlotswa and S'busiso Radebe). I greatly value their friendship because their constant support and encouragement helped me to overcome setbacks and stay focused on my study.

- ✓ Most importantly, I would like to thank my family (Lefu David Mofokeng, Mathabo Anna Mofokeng, Ntsoaki Kristina Mofokeng, Tselane Julia Mofokeng, Maserame Jeanette Mofokeng and Tahleho Bennie Mofokeng), to whom this dissertation is dedicated, for their various forms of support, constant source of love and strength which helped sustain me throughout this endeavor. I am also very grateful to my family to be part of my vision and their continuous guidance in my life.

- ✓ Last but not least, I would like to express my heart-felt gratitude to my fiancée Mpinane Lydia Molapo for her everlasting support, encouragements and everyday prayers which enabled me to complete this study. I warmly appreciate endless love and understanding of my fiancée.

Abstract

Recently, the essence of nanocrystalline phosphor materials to enhance the efficiency of solar cells have been the subject of interest in research. To improve the efficiency of solar cells, special attention has been paid to down-conversion based on nanomaterial phosphor doped with rare earth ions which absorb ultraviolet (UV) from the sun and down-convert them into visible photons that could subsequently be absorbed by solar cells.

Titanium dioxide (TiO_2) and zinc oxide (ZnO) nanoparticulate phosphor were activated with Eu^{3+} ions. These nanoparticles powders were successfully synthesized by co-precipitation method. The structural properties of TiO_2 nanoparticulate phosphor were examined with X-ray diffraction (XRD). The XRD confirmed crystallization of both tetragonal anatase and rutile phases and the average crystallite size of undoped and Eu^{3+} doped TiO_2 were 21 and 8 nm, respectively. Scanning electron microscopy showed that the morphology of TiO_2 nanoparticles composed of nanorods with average length and diameter of approximately 410 nm and 73 nm respectively. The optical properties of TiO_2 nanoparticulate phosphors were studied using photoluminescence (PL) spectroscopy and ultraviolet-visible (UV-Vis) spectroscopy. At 325 nm excitation wavelength, PL data showed a broad emission from undoped TiO_2 centred at 455 nm. This broad emission band was assigned to defects in TiO_2. Eu^{3+} doped TiO_2 nanoparticulate phosphors exhibited five emissions which are associated with f→f transitions of Eu^{3+} ions when excited at 466 nm. The band gaps of the nanophosphors were also determined from the UV-Vis reflectance measurement using Tauc's plot.

The XRD analysis of Eu^{3+} doped zinc oxide (ZnO) nanoparticulate phosphor was consistent with wurtzite hexagonal structure of ZnO. In addition, the XRD patterns confirmed the presence of secondary phase of Eu_2O_3. The morphological changes of ZnO nanoparticles due to incorporation of Eu^{3+} ions were observed from the SEM micrographs. The PL emission of undoped ZnO nanoparticulate phosphor excited at 325 nm exhibited weak ultraviolet emission and an intense broad deep level emission (DLE). This DLE is normally related to green, yellow and blue luminescence. The PL emission of ZnO:Eu^{3+} nanoparticulate phosphor excited at 466 nm showed weak and intense emissions at 593 nm, 618 nm, 646 m and 682-696 nm which are attributed to Eu^{3+} transitions: $^5D_0 \rightarrow {}^7F_J$ (J = 1, 2, 3 and 4) respectively.

Nanocomposite (ZnO-TiO_2) phosphors single doped with europium (Eu^{3+}) and co-activated with 0.4 mol% Dy^{3+}-Eu^{3+} with different concentrations of Eu^{3+} ions were synthesized via sol-gel method. The X-ray diffraction (XRD) confirmed crystallization of the wurtzite hexagonal ZnO and tetragonal TiO2 (anatase and rutile) phases. In addition, the XRD data confirmed that secondary phases of $ZnTiO_3$ and Zn_2TiO_4 were formed. ZnO–TiO_2 nanocomposites exhibited a broad band emission ranging from 400 nm to 900 nm and represent the combined emission band of both hexagonal wurtzite ZnO and tetragonal TiO_2 phases when excited at 325 nm. The co-activated nanocomposite were excited in the UV region with excitation wavelength of 248 nm and the corresponding emissions were observed in the visible region at 496, 584, 593 and 614 nm. The emissions at 496 nm and 584 nm were assigned to $^4F_{9/2} \rightarrow {}^6H_{15/2}$ and $^4F_{9/2} \rightarrow {}^6H_{13/2}$ $f \rightarrow f$ transitions of Dy^{3+} transitions while those at 593 nm and 614 nm were assigned to $^5D_0 \rightarrow {}^5F_1$ and $^5D_0 \rightarrow {}^5F_2$ $f \rightarrow f$ transitions of Eu^{3+} activator, respectively. Energy transfer mechanism between host and dopants (Dy^{3+} and Eu^{3+}) was discussed.

Keywords

Nanocomposites, down-conversions, energy transfer, europium, dysprosium, zinc oxide, titanium dioxide

Acronyms

- **XRD** X-ray diffraction
- **UV-Vis** Ultraviolet-visible spectroscopy
- **PL** Photoluminescence
- **FTIR** Fourier transmission infrared
- **FE-SEM** Field emission scanning electron microscopy
- **ET** Energy transfer
- **RE^{3+}** Rare earths
- **Ln^{3+}** Lanthanides
- **LED** Light emitting diode
- **DC** Down-conversion
- **UP** Up-conversion
- **Eu^{3+}** Europium
- **Dy^{3+}** Dysprosium
- **JCPDS** Joint Committee on Powder Diffraction Standard

- **CIE** Commission Internationale de 1’Eclairage
- **DLE** Deep level emission

Table of content

List of Figures

List of Tables

Chapter 1 Introduction

1.1 Nanoscience and nanotechnology

Nanoscience is the study of materials in the range of nanometres scale. “Nano” comes from the Greek “nanos” meaning “Dwarf”, and “Science” means knowledge. The prefix “nano” is used in the metric system to mean 10^{-9}. It is not just one science, but an interdisciplinary field that includes biology, chemistry, physics, medicine, material sciences, computer science etc. that seek to bring about mature nanotechnology focusing on nanoscale. Materials reduced to nanoscale can be classified into four dimensions (0, 1, 2 and 3 dimensions) and exhibit physical and chemical properties and enabling unique applications compared to bulk materials [1]. The reason why properties of structures are different at nanoscale is because the size of the material is inversely proportional to the ratio of surface area-to-volume of the structure. When the size or dimension of a material is continuously reduced, the ratio of surface area-to-volume of the structure increases. Since the chemical reactions takes place on the surface of a particle, the reaction can be very different if there is an increase in the surface area available for the reaction [2].

Nanotechnology provide the opportunity to design, characterize, produce and apply nanostructured materials to device fabrication and it enables us to apply our understating on how materials behave at the nanometre scale. Nanotechnology was first mentioned in a talk, entitled “*there is plenty of Room at the Bottom*” given by Richard Feynman in 1951. There are basically two major approaches for creating material at nanoscale. One is top-down and the other one is bottom up approaches. Top-down approach involves creation of nanomaterials from bulk materials where bottom up approach involves components made of single molecules which are held together by covalent forces. The application of nanotechnology in different fields include transportation, space exploration, energy and environment, electronics, health and medicine [1, 3].

1.2 Overview

Technologies in many different solar cells are considered as alternative for producing electricity as they produce electricity from sunlight without any "green-house" gas emission. Silicon based solar cells are currently dominating photovoltaic market concerning the technological advances over the last few years [4, 5]. In other words, solar cells or photovoltaic (PV) which utilizes sunlight has drawn great attention as a solution to the decreasing energy demand and environmental concerns, such as nitrogen oxides, sulphur dioxide, volatile organic compounds as well as heavy metals. It was reported that the sun provide an approximately 10, 000 times than the global demand (i.e., 3×10^{24} J/year) [4-7]. However, some energy are not absorbed to smaller energy photons that are transparent to the semiconductors and excess of higher energy photons of semiconductor is lost to thermalization. According to the literature, these losses can add up to more than 50% of the utilizable solar energy for solar cells. Down-conversion (DC) and up-conversion (UP) processes are viable option to avoid this energy loss [8].

With down-conversion method, one high energy photon which is absorbed at lower wavelength is converted into two or more lower energy at longer wavelength. Rear earth ions (RE^{3+}) activated metal oxide nanophosphors are considered as the best candidates to achieve down-conversion process [9]. Particularly, down-conversion involves down-converting of ultraviolet (UV) photons to visible (VIS) photons or near-infrared (NIR) photons by pairing rare-earths ions in the host. Because rare earth ions have rich energy level structure, energy transfer between them is also possible and down convert absorbed UV light to visible light by means of photons of different energy [10]. Research activities on down-conversion is focused on pairing different rare earths such as Er^{3+}/Yb^{3+}, Dy^{3+}/Eu^{3+}, Tb^{3+}/Yb^{3+}, Pr^{3+}/Yb^{3+} and Ce^{3+}/Tb^{3+} [11-15]. In this study, our focus was on the study of down-conversion process on the Dy^{3+}-Eu^{3+} co-activated ZnO/TiO_2 nanocomposites. Among rare earths ions, trivalent Eu^{3+} ion is one of the most important activator because of its rich red emission that play an important role in nanophosphors. As a results, Dy^{3+} is coupled with Eu^{3+} in a host materials to study energy transfer (ET) process between these two rare earths ions.

ZnO is a semiconductor material used in photovoltaic because it is easy to couple with TiO_2 to form a composite. These semiconductors tend to be paired to form composite because they have similar wide band gaps, but they have different properties that are advantageous for different

applications. For example, ZnO have higher conductivity compared to TiO_2 while TiO_2 have higher chemical stability and reactivity, much higher dielectric constant and fewer defects states. ZnO can be easily nanostructured. Doping of ZnO and TiO_2 with rare earth ions gives the opportunity to tune optical properties and emission intensities of each oxide in a controlled manner in order to enhance the performance of the solar cells. However, light at shorter wavelength can be used since the rare earths complexes have the ability to down-convert UV light into visible light of near infrared light [16, 17].

1.3 Problem statement

Economy and technology in the world is growing faster, so the demand for energy is also growing and the process of load shedding is taking place in South Africa because of the shortage of power station. Concerning the issue of building more power stations is another source of problem because it will use more coal which is not environmentally friendly. One way of addressing this problem is to enhance the existing solar cells by application of phosphor materials in nanoscale doped with rare earth ions. Therefore, this research aims to prepare and investigate the luminescent properties of nanoparticle phosphors that can be used to enhance the power conversion efficiency of solar cells. However, nanoparticles co-doped with Dy^{3+} and Eu^{3+} can be used to harvest photons at higher energy (shorter wavelength) and emit at lower energy (longer wavelength) though down-conversion process. In addition, the emission efficiency of nanoparticle in this study will be improved by co-doping Dy^{3+} with Eu^{3+} with different concentration of Eu^{3+} and study energy transfer from Dy^{3+} to Eu^{3+}.

1.4 Research Aim

The major aim of this research is to investigate the luminescence properties of UV down-converting ZnO/TiO_2:Dy^{3+}, Eu^{3+} nanocomposites.

1.5 Research objectives

- To synthesize and investigate the luminescence properties of Eu^{3+} ions doped different host namely, ZnO and TiO_2 nanoparticles using co-precipitation method by varying the concentration of Eu^{3+} ions.

- To synthesize and investigate luminescent properties of ZnO/TiO_2 nanocomposites doped with different concentration of Eu^{3+} ions using sol-gel method.
- To investigate luminescent properties of Dy^{3+} co-doped with Eu^{3+} in $ZnO\text{-}TiO_2$ nanocomposites prepared by sol-gel method.
- To study the energy transfer from Dy^{3+} to Eu^{3+} in $ZnO\text{-}TiO_2$ nanocomposites in order to enhance the emission of Eu^{3+}.

1.6 Thesis layout

This thesis is divided into the following eight chapters:

Chapter 1 provides a general introduction about nanoscience and nanotechnology, overview and aims of the study. **Chapter 2** provides the theoretical background on the fundamentals of nanomaterial phosphors, luminescence processes and energy transfer in rare earth activated phosphors mainly for down conversion applications in the nanotechnology. It also provide the information on the structural analysis of ZnO and TiO_2 semiconductors. **Chapter 3** gives a brief description of the synthesis methods and characterization techniques that were used for preparation and characterization of nanomaterial phosphors. **Chapter 4** discusses the luminescent properties of $TiO_2:Eu^{3+}$ nanoparticles prepared by co-precipitation method. In **Chapter 5** the luminescent properties of $ZnO:Eu^{3+}$ nanoparticles prepared by co-precipitation method is discussed. **Chapter 6** presents the luminescent properties of the $ZnO/TiO_2:Eu^{3+}$ nanocomposites synthesized by sol-gel method. Preparation and characterization of UV down-converting ZnO/TiO_2: Dy^{3+}, Eu^{3+} nanocomposites are presented in **Chapter 7**. Finally, **Chapter 8** gives the summary of the thesis and suggestion of the future work.

1.7 References

[1] S.A. Yousaf and S. Ali. Journal of faculty of engineering and technology, **(2008)** 11-20.

[2] Nano in my life, [online], Available from https://nanohub.org/resources/17645/download/NEATEC-Trinity_College_Module_1_What_is_nanoscience__Workbook.pdf [Accessed 28 July 2015]

[3] G.A. Menezes, P.S. Menezes and C. Menezes. Internet Journal of Medical, **6**(1) (**2011**) 16-23.

[4] I. Litzov and C.J. Brabec. Materials, 6 **(2013)** 5796-5820.

[5] Hansen P.A. *Light conversion materials for solar cells by atomic layer deposition*, **2014**, [PhD Thesis], University of Oslo, Norway.

[6] M. Kouhnavard, S. Ikeda, N.A. Ludin, K.N.B. Ahmad, B.V. Ghaffari, M.A. Mat-Teridi, M.A. Ibrahim, S. Sepeai, K. Sopian. Renewable and Sustainable Energy Reviews, 37 **(2014)** 397- 407.

[7] L. Hongzhou, H. Zhiyao, S. Mengmeng, G. Dongling, Z. Yang and L. Jun. Energy, 57 **(2013)** 270-283.

[8] T. Saga. NPG Asia Mater, 2(3) **(2010)** 96–102.

[9] S. Das and K.C. Mandal. Materials Letters, 66 **(2012)** 46–49.

[10] W.G.J.H.M. van Sark, A. Meijerink and R.E.I. Schropp (**2012**). Solar Spectrum Conversion for photovoltaic Using Nanoparticles, Third Generation Photovoltaic, Dr. Vasilis Fthenakis (Ed.), ISBN: 978-953-51-0304-2, InTech, Available from: http://www. Rare earth doped phosphors for improving efficiencies of solar cells intechopen.com/books/third-generation-photovoltaics/solar-spectrumconversion-for-photovoltaics-using-nanoparticles.

[11] J.J. Velázquez, V.D. Rodríguez, A.C. Yanes, J. del-Castillo and J. Méndez-Ramos. Optical Materials, 34 **(2012)** 1994–1997.

[12] V.R. Bandi, B.K. Grandhe, H.J. Woo, K. Jang, D.S. Shin, S.S. Yi and J.H. Jeong. Journal of alloys and compounds, 538 **(2012)** 85–90.

[13] Q.J. Chen, W.J. Zhang, X.Y. Huang, G.P. Dong, M.Y. Peng and Q.Y. Zhang. Journal of alloys and compounds, 513 **(2012)** 139–144.

[14] I.A.A. Terra, L.J. Borrero-Gonza´lez, T.R. Figueredo, J.M.P. Almeida, A.C. Hernandes, L.A.O. Nunes and O.L. Malta. Journal of luminescence, 132 **(2012)** 1678–1682.

[15] P.A. Loiko, N.M. Khaidukov, J. Méndez-Ramos, E.V. Vilejshikova, N.A. Skoptsov and K.V. Yumashev. Journal of Luminescence, 170 **(2016)** 1–7.
[16] B.S. Richards. Solar energy materials and solar cells, 9 **(2006)** 1189 – 1207.
[17] N. Yao, J. Huang, K. Fu, S. Liu, Y Wang, X. Xu, M Zhu and B. Cao. Journal of power sources, 267 **(2014)** 405 – 410.

Chapter 2 Theoretical background

2.1 Introduction

This chapter provides a brief background, characteristics and luminescence properties of phosphor nanomaterials. Furthermore, it briefly presents the theory of energy transfer that may occur between activators and the applications of rare earth ions doped phosphor nanomaterial are also discussed. It also refer to the need for improved luminescence of rare earths and their uses in various kinds of nano-technological applications.

2.2 Fundamentals of phosphor

Phosphor is known as a materials that exhibits the phenomenon of luminescence. The luminescence is the process by which materials absorbs light of a specific spectral range when excited with external energy such as electrons or photons and re-emits light of another spectral range with longer wavelength. When the material absorbs light from the excitation source, electrons jump from the lowest energy level (valence band) to higher energy level (conduction band) and the light may be emitted when these electrons return to the lowest energy level. The materials that emit over a characteristics time $t_c > 10^{-8}$ s are called phosphorescent while those that emit almost instantaneously (characteristic time $t_c < 10^{-8}$ s) are referred to as fluorescent [1]. The phosphor or luminescent materials consists of host lattice (often oxides, sulfides, germinates, oxysulfides, etc.) which are activated by a dopant or activator (usually rare-earth or transition metal elements) to tune the colour of their emission depending on the applications [2]. If the phosphor host is co-doped with two dopants, one of the dopant is called activator and the other one is called sensitizer whereby the sensitizer absorbs the energy and subsequently transfers it to the activator. The sensitizer is used to enhance the emission of the activator when the activator ions show relatively a weak absorption [3]. In line with the objective of this study such as the preparation of

nanomaterials phosphors that can be used as down-conversion luminescent nanomaterials in different applications including white light emission from hybrid LEDs [4], liquid crystal displays (LCDs) systems [5], photovoltaic devices [6] and many more. Figure 2.1 summarizes some applications of up and down-conversion nanomaterials phosphors. Therefore, the main objective of this current research is to study down-conversion method in nanocomposites phosphors based semiconductors (ZnO and TiO_2) couples with rear earths (Dy^{3+} and Eu^{3+}) ions. Semiconductor are considered excellent hosts for rare earth ions in consideration of the preparation of semiconducting nanocomposite phosphors because of, among other things, activating with lanthanides give the opportunity to tune their luminescent properties. In addition, the light which they emit in UV region (shorter wavelength) can be absorbed by lanthanides ions and re-emit in the visible region (longer wavelength) through down-conversion process [7, 8].

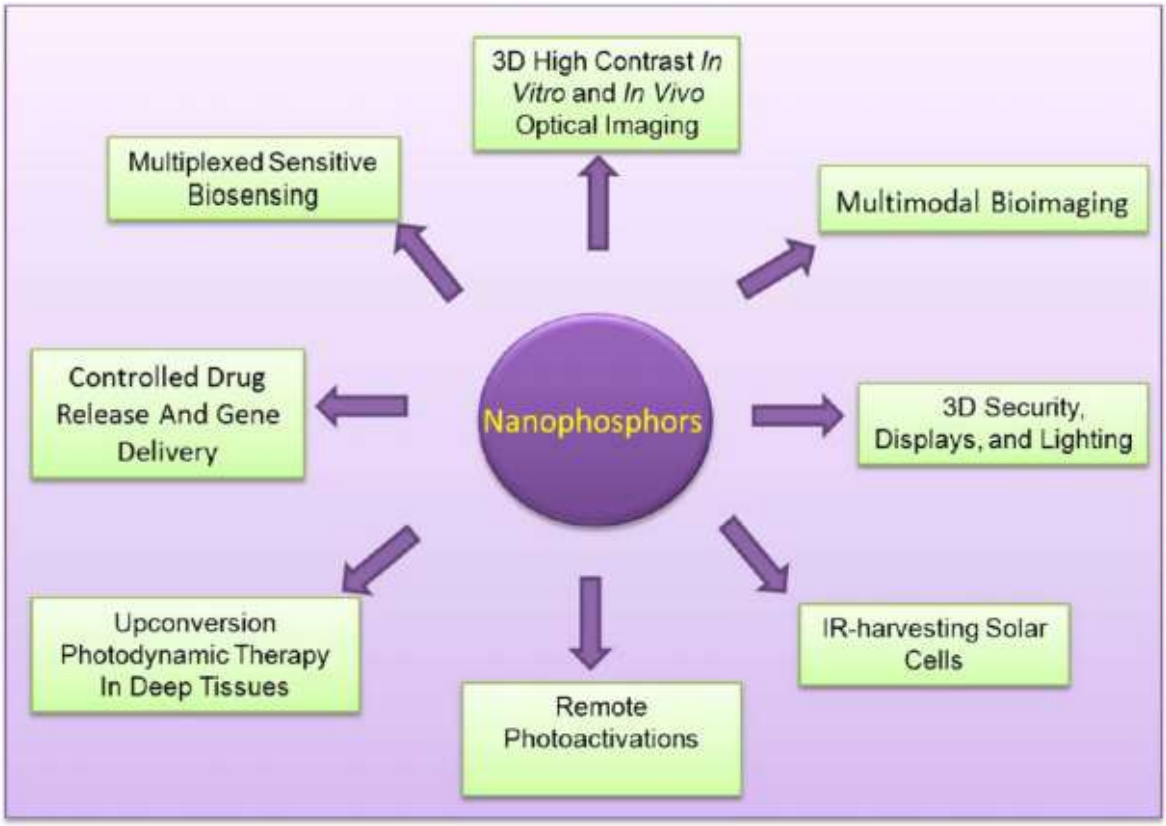

Figure 2.1 Some various applications of up and down-conversion nanomaterial phosphors [9].

2.3 Zinc oxide (ZnO) nanoparticle

Semiconducting zinc oxide (ZnO) has gained considerable attention in physics, chemistry and materials science research due to its physical properties such as wide band gap (3.36 eV) and large exciton binding energy (60 meV) at room temperature [10]. ZnO commonly known as zincite as a mineral has a crystal structure belonging to space group $P6_3mc$ (No.186) with $a = b = 3.24992$ Å and $c = 5.20658$ Å, V = 47.625 Å^3 and Z = 2 [11]. ZnO can crystalize in either hexagonal wurtzite structure or cubic zinc blende in which anion is surrounded by four cations at the corners of a tetrahedron and vice versa. This type of tetrahedral coordination is a typical characteristic of sp^3 covalent bonding nature but experimentally, these materials also have a substantial ionic character that tends to increase the bandgap beyond the one expected from the covalent bonding. Zinc oxide is also classified as one of the II-IV compound semiconductor whose ionicity resides at the borderline between the ionic semiconductors and covalent. Figure 2.2 illustrate the basic crystal structures shared by ZnO, namely: rocksalt or Rochelle, zinc blende and hexagonal wurtzite.

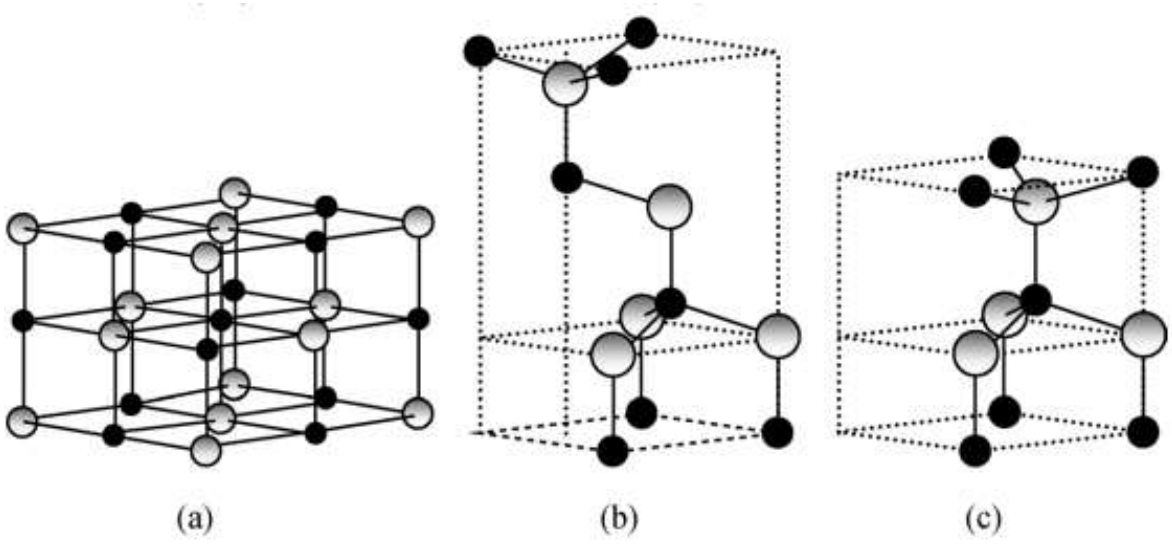

Figure 2.2 ZnO crystal structures represented by stick and balls: (a) cubic rocksalt, (b) cubic zinc blende, and (c) hexagonal wurtzite. Black and shaded grey lack spheres denote Zn and O atoms, respectively [12].

In the normal crystal structure of ZnO, the thermodynamically stable phase is that of wurtzite symmetry under ambient conditions while the zinc blende phase can be stabilized only by growth on cubic substrate. Figure 2.3 (a) shows the schematic representation of the wurtzite structures of the most common crystallization state of ZnO with details (figure 2.3 (b)) on the lattice parameters [13]. The basic wurtzite structure of ZnO consists of alternating stacking arrangements of tetrahedrally coordinated zinc (Zn^{2+}) and oxygen (O^{2-}) along *c*-axis direction. Each anion in wurtzite hexagonal structure of ZnO is surrounded by four cations at the corners of the tetrahedron. Similarly, each cation is surrounded by four anion with the cation at the centre. Zinc oxide is a widely known semiconductor employed in variety of applications in sensing, cosmetics, energy storage, optics etc. Recently, various synthesis methods have been employed to grow a variety of ZnO nanostructures due to its wide areas of applications. ZnO nanostructures include nanowires, nanorods, nanoparticles, nanobelts, nanotubes and other complex morphologies. In this study, we synthesized and investigated the structure and optical properties of undoped and Eu^{3+} doped ZnO nanoparticles because nanoparticles semiconductors offer useful properties such fluorescence and magnetic behavior [14].

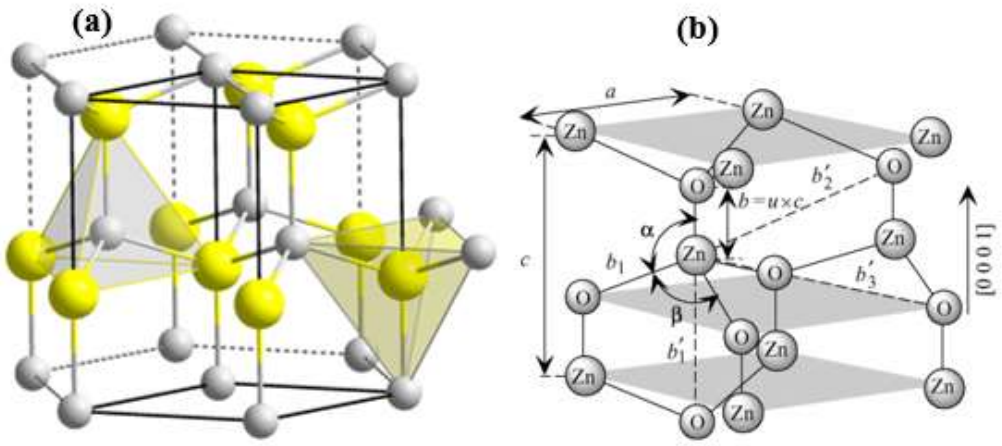

Figure 2.3 (a) Crystal structure of a hexagonal wurtzite ZnO [13] and (b) schematic representation of a wurtzitic ZnO structure with lattice constants "*a*" in the basal plane and "*c*" in the basal direction, "*u*" parameter, which is expressed as the bond length or the nearest-neighbour distance *b* divided by *c* (0.375 in ideal crystal), *a* and *b* (109.47 in ideal crystal) bond angles, and three types of second-nearest-neighbour distances b'$_1$, b'$_2$, and b'$_3$ [12].

2.4 Titanium dioxide (TiO_2) nanoparticle

Titanium dioxide (TiO_2) also known as titania is the most considerable metal oxide which commonly used for environmental and energy applications due to its tunable valence and conduction positions, chemical stability, cost-effectiveness, non-toxicity and strong oxidizing power. Titania can crystalize into three polymorphs, namely, stable rutile phase, metastable anatase and brookite phases as shown in figure 2.4 [15].

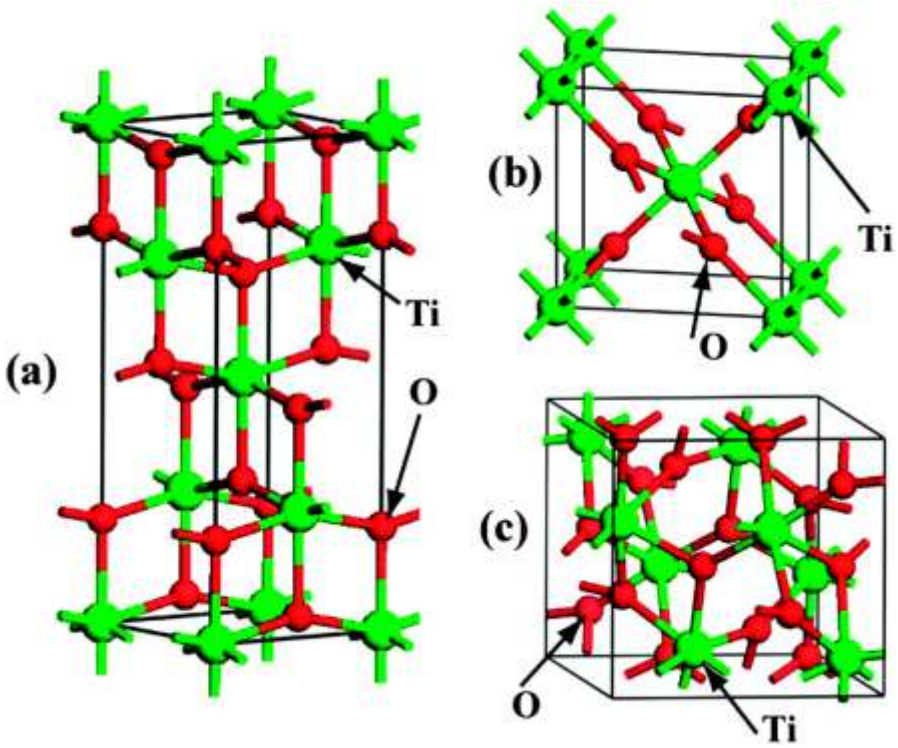

Figure 2.4 Conventional cells for anatase (a), rutile (b) and brookite (c) TiO_2. The big green and the small red spheres represent Ti and O atoms, respectively [15].

Both the rutile and anatase phases have a tetragonal structure which is described in terms of chains of TiO_2 octahedra, where each Ti^{4+} ion is surrounded by an octahedron of six O^{2-} ions and brookite has an orthorhombic structure. The structure of brookite is composed of octrahedra where the Ti^{4+} ions at its centre and O^{2-} ions at its corner [16]. It can exist in crystalline and amorphous forms. It is often investigated in nanometre range because it has good electrical, optical and magnetic properties that are different from their bulk counterparts. The amorphous TiO_2 gel that form during aging process crystallizes into anatase while phase transformation (anatase to rutile) in titania

occurs at higher temperature or during annealing which undergoes substantial aggregation and grain growth [17]. Among the unique properties of titania is that in nanometre range it has been considered as a suitable candidate for solar energy based on photovoltaic and photocatalytic process due to its tunable band gap energy by intentional impurities. Figure 2.5 shows the band gap energies of common semiconductors that plays a significant role in the photocatalytic process. TiO_2 and ZnO have a similar band gap energy (~3.2 eV) which shows that near ultraviolet irradiation (UV) is needed for photo activation of both semiconductors. Since these semiconductors have a similar band gap energies, TiO_2 can be mixed easily with ZnO to form a composite to obtained efficient photocatalysis process compared to the single element of ZnO and TiO_2 [18]. In this study, TiO_2 doped with Eu^{3+} and ZnO-TiO_2 co-doped with Dy^{3+} and Eu^{3+} were investigated. In addition, the energy transfer through down-conversion process between Dy^{3+} and Eu^{3+} was investigated.

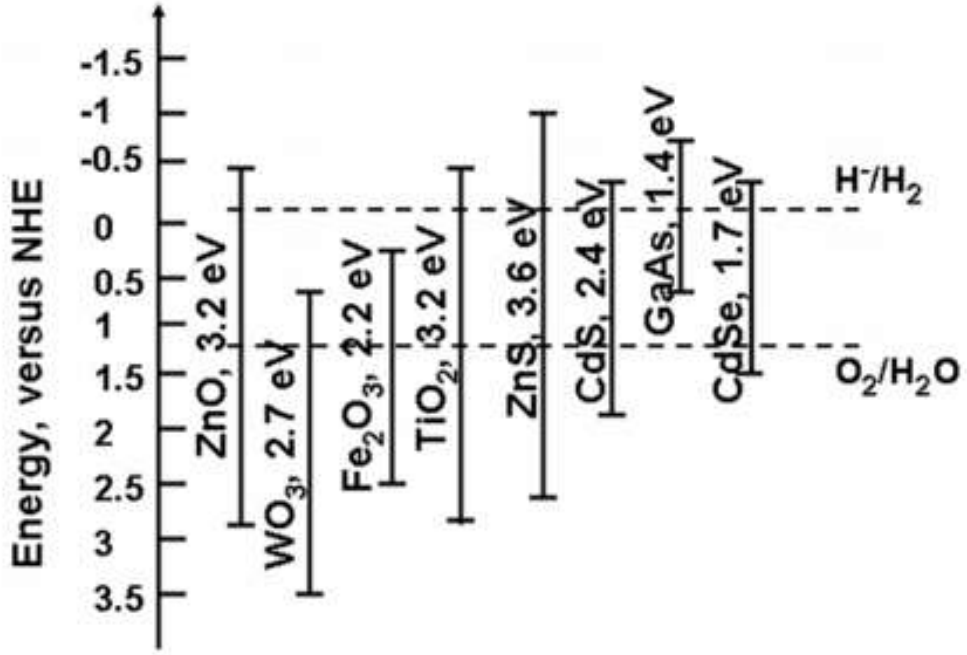

Figure 2.5 Band edge positions of common semiconductor for photocatalytic process versus normal hydrogen electrode (NHE) [18].

2.5 Trivalent Lanthanides ions

Lanthanides (Ln^{3+}) ions, known as lighting elements refers to a series of 15 consecutive elements in the periodic table ranging from lanthanum (atomic number Z = 57) to lutetium (atomic number

Z=71). The term "rare earth" (RE^{3+}) ions is commonly applied in more restricted sense as a synonym for the lanthanides coupled with scandium (atomic number Z= 21) and yttrium (atomic number Z=39) elements. The electronic configuration of trivalent Ln^{3+} ions is given as follows: [Xe]$4f^n$. The $4f^n$ electrons shell structure of all trivalent Ln^{3+} ions are filled gradually from n = 0 to 14 electrons and lies inside the shell and therefore are efficiently shielded by the filled $5s^2$ and $5p^6$ electrons shells so that the 4*f* electrons are less influenced by the environment of the lanthanide ions even in solid materials. Table 2.1 present electronic structure of the trivalent Ln^{3+} ions [19]. A characteristic feature of lanthanides ions is their line-like emission in ultraviolet, visible or near infrared spectral regions which results in high purity the colour of emissions. The emission colour depend on the respective lanthanides ions as shown in figure 2.6. The emission from lanthanides are due to optical transition inside the $4f^n$ electron shell, thus intra-configurational $f \rightarrow f$ transition [20]. As a result, $f \rightarrow f$ emission lines of these lanthanides ions are characteristic since the rearrangement consecutive to the promotion of an electron into a 4*f* electron shell of higher energy does not disturb the binding pattern in the molecular because 4*f* electron shell do not participate much in this binding [21]. Figure 2.7 present the Dieke diagram giving more details about the $4f^n$ configuration as a function of atomic number.

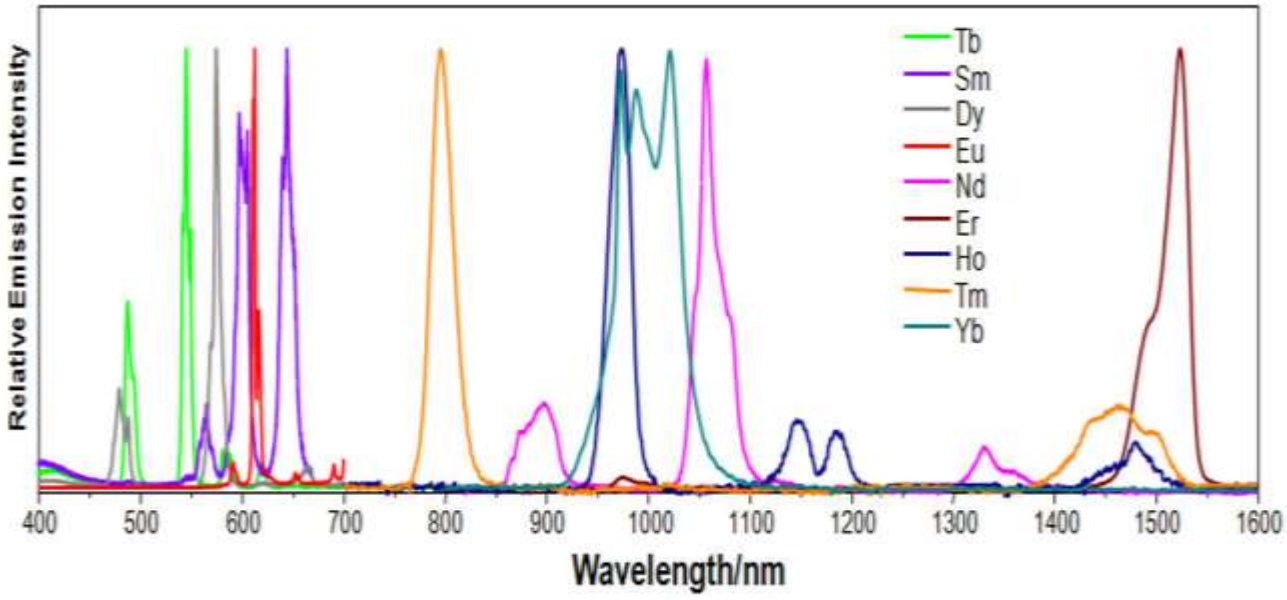

Figure 2.6 Characteristics emission bands of some lanthanide ions [22].

Table 2.1 Electronic structure of trivalent lanthanides ions [20].

element	symbol	atomic number (Z)	configuration Ln^{3+}	ground state Ln^{3+}
lanthanum	La	57	[Xe]	$^1S_0$
cerium	Ce	58	[Xe]$4f^1$	$^2F_{5/2}$
praseodymium	Pr	59	[Xe]$4f^2$	$^3H_4$
neodymium	Nd	60	[Xe]$4f^3$	$^4I_{9/2}$
promethium	*Pm*	61	[Xe]$4f^4$	$^5I_4$
samarium	Sm	62	[Xe]$4f^5$	$^6H_{5/2}$
europium	Eu	63	[Xe]$4f^6$	$^7F_0$
gadolinium	Gd	64	[Xe]$4f^7$	$^8S_{7/2}$
terbium	Tb	65	[Xe]$4f^8$	$^7F_6$
dysprosium	Dy	66	[Xe]$4f^9$	$^6H_{15/2}$
holmium	Ho	67	[Xe]$4f^{10}$	$^5I_8$
erbium	Er	68	[Xe]$4f^{11}$	$^4I_{15/2}$
thulium	Tm	69	[Xe]$4f^{12}$	$^3H_6$
ytterbium	Yb	70	[Xe]$4f^{13}$	$^2F_{7/2}$
lutetium	Lu	71	[Xe]$4f^{14}$	$^1S_0$

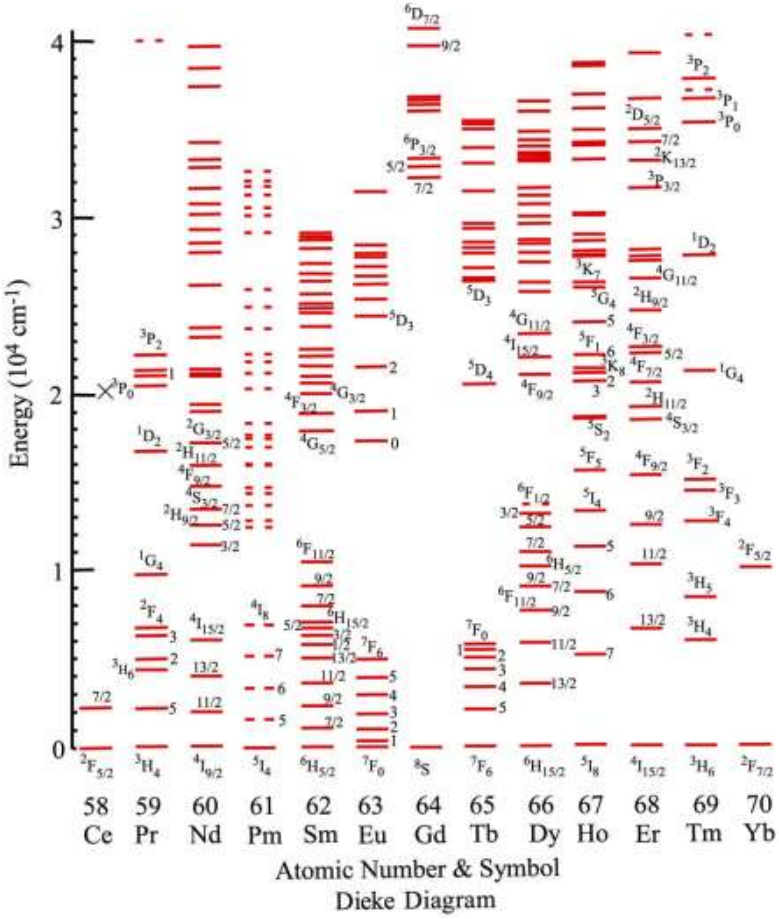

Figure 2.7 Dieke energy-level diagram of trivalent rare earth (RE^{3+}) ions [23].

2.6 Luminescence centres

Luminescence centre is a crystal defects such as activators or interstitial atoms and ions induced in crystal phosphors. These centre can be single atoms or coupled atoms that are so closed to one another so that they absorb and emit light as a single-mechanical system. The luminescence centre that results from the dopants/activators is so called activator centre and the luminescence centre result from crystal defects is known as host crystal centre. A well-known characteristics of luminescent centres are their sharp emissions and absorption spectrum. The spectra of luminescent centre from rare earth ions doped phosphor turn out to be line spectra produced by quantum transition in the inner electron shell of the ions. Broadening of the bands are caused by lattice when the phosphor is activated by atoms of elements whose spectra produced by transition in an outer electron shell [24]. Figure 2.8 depicts the basic luminescence mechanism in luminescent centres. During the excitation in the host lattice with dopant/activator, the dopant is directly excited by incoming photon energy whereby these energy is being absorbed by electrons and is raised to an excited state. Then the electron relaxes non-radiatively the lowest vibrational level of the excited state and therefore radiatively decay to the ground state by means of emission [25].

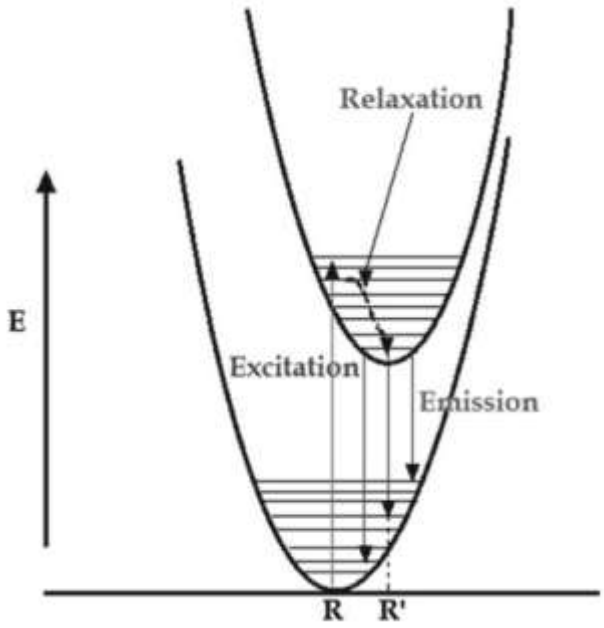

Figure 2.8 Configurational coordinate diagram showing mechanism in a luminescent centre [25].

2.7 Trivalent europium (Eu^{3+}) ions

Europium (III) ions is a well-known rare earth ions that exhibit narrowband red photoluminescence in the visible region upon irradiation with ultraviolet (UV) radiation. The other typical characteristics of europium (III) ions is the narrow transitions in the absorption and photoluminescence spectra. The energy level structure of europium (III) ions is given by [Xe]$4f^6$ configuration. This configuration has 60 electrons whereby 54 electron are in the same closed shells as xenon atoms and the other 6 electrons in the $4f$ shell which is shielded from environment and the closed $5s^2$ and $5p^6$ outer shells. The emission spectra of europium (III) ions shows intense photoluminescence due to transition from $^5D_0$ level to the ^7F_j (j = 0, 1, 2, 3, 4, 5, 6) levels [26]. The most common transitions are $^5D_0 \rightarrow {}^7F_j$ (j = 0 - 4) transitions as shown in figure 2.9.

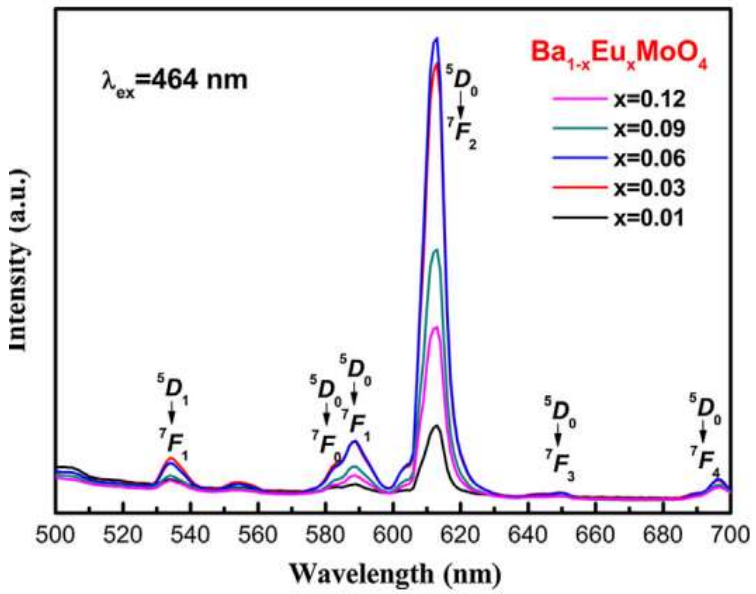

Figure 2.9 Emission spectrum of Eu^{3+} ions doped $BaMoO_4$ [27].

In most cases, the $^5D_0 \rightarrow {}^7F_0$ transitions is known to be strictly forbidden according to the standard Judd-Ofelt theory. The occurrence of this transition is due to J-mixing or to mixing of low –lying charge-transfer states into the wave functions of the $4f^6$ configuration. The intensity emission of the magnetic dipole transition $^5D_0 \rightarrow {}^7F_1$ is not dependent on the environment of europium (III) ions whereas the intensity emission of the electric dipole transition $^5D_0 \rightarrow {}^7F_2$ depends on strongly on the sites symmetry sites in the crystal. The emission intensity of magnetic dipole transition

$^5D_0 \rightarrow {}^7F_1$ transition is dominant when europium (III) occupy the inversion symmetry in the crystal sites. On the other hand, the emission intensity of $^5D_0 \rightarrow {}^7F_1$ transition is dominant when europium (III) does not occupy the inversion symmetry in the crystal sites. The $^5D_0 \rightarrow {}^7F_1$ transition is generally weak and its intensity depend on the J-mixing and the $^5D_0 \rightarrow {}^7F_4$ transition lies in the spectroscopic region in which most of photomultiplier tubes have a low sensitivity [26].

2.8 Trivalent dysprosium (Dy^{3+}) ions

Trivalent dysprosium (III) ions is one of the rare-earth ions used as an energy sensitizer due to its relatively long decay time with $^4F_{9/2}$ level for many technological applications. Dysprosium (III) ions activated materials have several luminescence wavelength between the available f→ f transitions in the visible region which depend on the type of host matrix. The luminescent materials activated by dysprosium (III) ions are normally used for generation of white light. The energy level structure of dysprosium (III) ions is given by [Xe]$4f^9$ configuration with two main luminescence transitions which are $^4F_{9/2} \rightarrow {}^6H_{15/2}$ (blue emission) at 489 nm and $^4F_{9/2} \rightarrow {}^6H_{13/2}$ (yellow emission) transitions at 575 nm [28]. The $^4F_{9/2} \rightarrow {}^6H_{13/2}$ transition is highly hypersensitive, which strongly depend on the crystal-field environment. Dysprosium (III) ions also exhibit weak emission that is assigned to $^4F_{9/2} \rightarrow {}^6H_{13/2}$ transition at 668 nm and figure 2.10 shows the emission spectra of Dy^{3+} doped sodium lead borophospahate glasses (SLBPD) [29].

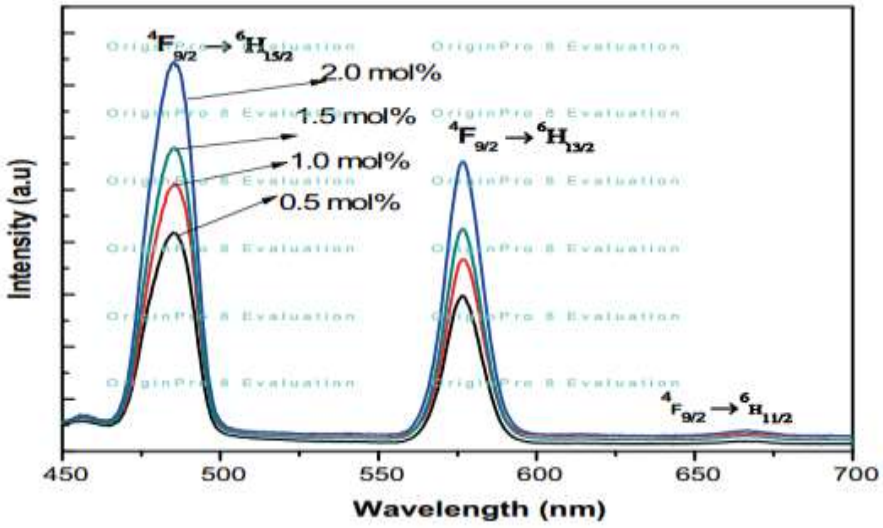

Figure 2.10 Emission spectrum of SLBPDDy10 glass [30].

2.9 Down-conversion technique

The use of rare-earths (RE^{3+}) ions to convert light to different useful wavelengths in the spectrum is well-known in the present days from different applications (e.g. sensors, LEDs devices, solar cells). Based on that, down-conversion and up-conversion mechanisms based on nanomaterials doped with rare-earths are usually exploited to convert UV light and IR light into visible region [31]. In these research, we focus on the down-conversion mechanism in which rare earths absorbs UV photons and convert into visible region through energy transfer between rare-earths ions. It has been reported that single junction solar cell efficiency is 30% and this limit is known as Shockely-Queisser limit. Different method have been implemented to break the Shockely-Queisser limit in the past few years to enhance the efficiency of the solar cells through down-conversion. The idea of down-conversion method is motivated by the fact that some of photons are lost to the thermalization of higher energy photons in solar cell [32]. The characteristics of rare earths ions is that they have a rich and well separated energy levels structure. In addition, rare earth ions have as many energy levels available in its energy structure which allows electrons to transfer freely between them to be used for high efficiency down conversion applications [33]. The down-conversion processes, have been efficiently achieved to down convert ultraviolet light into visible emission by using the following coupled rare earths, Er^{3+}/Yb^{3+}, Tb^{3+}/Yb^{3+}, Pr^{3+}/Yb^{3+} and Ce^{3+}/Tb^{3+} [34-37]. In this work, our aim is to study down-conversion process on the Eu^{3+}/Dy^{3+} coupled in the ZnO/TiO_2 nanocomposites.

2.10 Energy transfer nanophosphor

Energy transfer is a process that occur normally in a system in which the excited state transitions of the sensitizer ions overlap with the ground state transition absorption of the acceptor ions. In phosphor, the energy transfer can happen between the host lattice and the single activator ion or between different activators in the host lattice [38]. Energy transfer between a sensitizer ion (S) and an activator ion (A) can be written as a chemical reaction

$$S^* + A \rightarrow S + A^* \quad (2.1)$$

where the asterisk indicates the excited state.

The mechanism of energy transfer requires the physical interaction between the sensitizer and the activator. However, during the physical interaction, this energy transfer can be able to find its origin in electrostatic or exchange interaction. Therefore, spectral overlap between absorption spectrum of the activator and emission spectrum of the sensitizer have to be observed, respectively, targeting energy conversion [39]. The dominant mechanism of the energy transfer is usually dipole-dipole interaction whereby the ions get spatially closer one another with the increase in dopant concentration and there are some few criteria that lead to action of energy transfer in materials. This kind of process must be proportional to R^{-6} where R is the distance between the two centres. Additionally, the rate at which energy is transferred must also be proportional to the spectral overlap between emission spectrum of sensitizer and the absorption spectrum of the activator. During the process of energy transfer, the transfer rate is faster from the broad band sensitizer to broad band activator compared to transfer rate from broad band sensitizer to a narrow line acceptor. This whole process is due to anticipated larger spectral overlap in band to band process. In addition, energy transfer is believed to take place when the transition between the sensitizer and the activator are parallel to each other (i.e. ground state and excited state of sensitizer and activator are in resonance condition or equal) [40, 41]. Figure 2.11 shows the spectral overlap that must be satisfied in order for the process of energy transfer to take place.

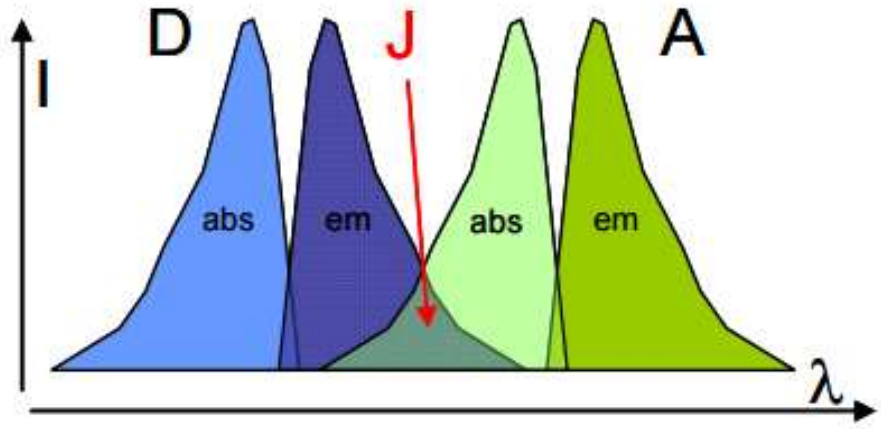

Fig. 2.11 Schematic diagram of the spectral overlap of a donor emission and acceptor absorption. J represent the spectral overlap, D is the donor emission and A is the acceptor absorption [42].

2.11 References

[1] M. Zollers. Phosphor Modeling in LightTools, 2011, Sypnosis predictable success, United States.

[2] M. Cates and S. Allison, *http://web.ornl.gov/sci/phosphors/Pdfs/tutorial.pdf.* [accessed 17 November 2015].

[3] D.L. Dexter, J. Chem. Phys, 21 (1953) 836.

[4] J.N. Findlay, J. Bruckbauer, A.R. Inigo, B. Breig, S. Arumugam, D.J. Wallis, R.W. Martin, and P.J. Skabara. Adv. Mater, 26 (**2014)** 7290–7294.

[5] S. Coe-Sullivan, W. Liu, P. Allen, and J.S. Steckel. ECS Journal of Solid State Science and Technology, 2 (2) **(2013)** R3026-R3030.

[6] B.S. Richards, A. Ivaturi, S.K.W. MacDougall and J. Marques-Hueso. ResearchGate, 1 **(2012)** 1-8.

[7]. B.S. Richards. Solar Energy Materials & Solar cells, 90 **(2006)** 1189-1207.

[8] N. Yao, J. Huang, K. Fu, S. Liu, Y Wang, X. Xu, M Zhu and B. Cao. Journal of power sources, 267 **(2014)** 405- 410.

[9] G. Chen, C. Yang and P.N. Prasad. Account of chemical research, 46(7) **(2013)** 1474–1486.

[10] T. Rossi, T. J. Penfold, M. H. Rittmann-Frank, M. Reinhard, J. Rittmann, C. N. Borca, D. Grolimund, C. J. Milne, and M. Chergui. J. Phys. Chem. C, 118 **(2014)** 19422−19430.

[11]ZnO crystal structure, [online]. Available from http://www.rug.nl/research/portal/files/9818571/appendix.pdf [accessed 18 November 2015].

[12] Zinc Oxide*: Fundamentals, Materials and Device Technology*. Hadis Morkoç and Ümit Özgur Copyright © **2009** WILEY-VCH Verlag GmbH & Co. KGaA, Weinheim ISBN: 978-3-527-40813-9.

[13] ZnO crystal structure, [online]. Available from https://upload.wikimedia.org/wikipedia/commons/8/8e/Wurtzite_polyhedra.png [accessed 18 November 2015].

[14] M. Vaseem, A. Umar and Y.B. Hahn. Metal oxide nanostructures and their applications, 5 **(2010)** 1-36.

[15] J. Zhang, P. Zhou, J. Liub and J. Yu. Phys. Chem. Chem. Phys., 16 (**2014)** 20382—20386.

[16] A.D. Paola, M. Bellardita and L. Palmisano. Catalysts, 3 **(2013)** 36-73.

[17] R. SharmilaDevi, Dr.R. Venckatesh, Dr. RajeshwariSivaraj. International Journal of Innovative Research in Science, Engineering and Technology, 3(8) **(2014)** 1506-1511.

[18] L. K. Krasteva, K. I. Papazova, A. S. Bojinova, N. V. Kaneva, and A. A. Apostolov. 45(4) **(2013)** 625–630.

[19] X. Chen, Y. Liu and D. Tu. **(2014)**. *Lanthanide-Doped Luminescent Nanomaterials*. New York: Springer Heidelberg New York Dordrecht London.

[20] K. Binnemans. Lanthanide-Based Luminescent Hybrid, Mater Chem Rev., 109 (9) **(2009)** 4283–4374.

[21] Jean-Claude G. Bunzli and Svetlana V. Eliseeva, Basics of Lanthanide Photophysics in Lanthanide Luminescence: Photophysical, Analyticaland Biological Aspects, Springer SerFluoresc, Springer-Verlag Berlin Heidelberg **(2010)**.

[22] Polumetallic lanthanides complex and nanocrystals emitting in the visible in the near-infrared [Online]. Available from *http://oasys2.confex.com/acs/236nm/techprogram/P1206923.HTM*. [Accessed 21 November 2015]

[23] K.A. Gschneidner Jr., J.G. Bünzli and V.K. Pecharsky. Handbook on the Physics and Chemistry of Rare Earths, North-Halland, Vol. 37 **(2007)**.

[24] Luminescent centres, [online]. Available from http://encyclopedia2.thefreedictionary.com/Luminescent+Centre [accessed 29 November 2015].

[25] K. N. Shinde S.J.Dhoble, H.C Swart and K. Park., *Phosphate Phosphors for Solid-State Lighting*, Springer Series in Materials Science 174, Springer-Verlag Berlin Heidelberg **(2013).**

[26] K. Binnemans. Coordination Chemistry Reviews 295 **(2015)** 1– 45.

[27] B. Wu, W. Yang, H. Liu, L. Huang, B. Zhao, C. Wang, G. Xu and Y. Lin. Spectrochimica Acta Part A: Molecular and Biomolecular Spectroscopy 123 **(2014)** 12–17.

[28] D. Rajesh, K. Brahmachary, Y.C. Ratnakaram, N. Kiran, A.P. Baker and G.G. Wang. Journal of Alloys and Compounds, 646 **(2015)** 1096 – 1103.

[29] N. Kumam, N.P. Singh, L.P. Singh and S.K. Srivastava. Nanoscale Research Letters, 10 **(2015)** 347.

[30] N. Kiran and A.S. Kumar. Journal of Molecular Structure, 1054–1055 **(2013)** 6–11.

[31] F. Liu, Q. Han, T. Liu, Y. Chen, Y. Du, Y. Yao. Optical Materials 46 **(2015)** 77–81.

[32] M.B. Spitzer, H.P. Jenssen and A. Cassanho. Solar energy materials and solar cells, 108 **(2013)** 241 – 245.

[33] M. Alkiswani. Spectrum conversion in solar cells industry (**2015)**, [Master's Thesis], Halmstad university, Sweden.

[34] J.J. Velázquez, V.D. Rodríguez, A.C. Yanes, J. del-Castillo and J. Méndez-Ramos. Optical Materials, 34 **(2012)** 1994–1997.

[35] Q.J. Chen, W.J. Zhang, X.Y. Huang, G.P. Dong, M.Y. Peng and Q.Y. Zhang. Journal of Alloys and Compounds, 513 **(2012)** 139–144.

[36] I.A.A. Terra, L.J. Borrero-Gonza´lez, T.R. Figueredo, J.M.P. Almeida, A.C. Hernandes, L.A.O. Nunes and O.L. Malta. Journal of Luminescence, 132 **(2012)** 1678–1682.

[37] P.A. Loiko, N.M. Khaidukov, J. Méndez-Ramos, E.V. Vilejshikova, N.A. Skoptsov and K.V. Yumashev. Journal of Luminescence, 170 **(2016)** 1–7.

[38] J. Ganem and S.R. Bowman. Nanoscale Research Letters, 8 **(2013)** 455.

[39] C.R. Ronda. Luminescence: From Theory to Applications **(2008)**, WILEY-VCH Verlag GmbH & Co. KGaA, Weinheim, ISBN: 978-3-527-31402-7.

[40] L. Agazzi. Spectroscopic Excitation and Quenching Processes in Rare-Earth-Ion-Doped Al_2O_3 and their Impact on Amplifier and Laser Performance. The Netherlands (**2012)**, Enschede.

[41] P.P. Mokoena, H.C. Swart and O.M. Ntwaeaborwa. *Narrowband Ultraviolet B emission from gadolinium and praseodymium co-activated calcium phosphate phosphors for phototherapy lamps*. [Master's Thesis], University of the Free State, South Africa.

[42] Förster resonance energy transfer, [online]. Available from http://www.horiba.com/fileadmin/uploads/Scientific/Documents/Fluorescence/TechNote-3b-Foerster_resonce_energy_transfer__FRET_.pdf.

Chapter 3 Synthesis Methods and Characterization Techniques

3.1 Introduction

There are two methods that play a very important role in the modern synthesis of nanomaterial and fabrication of nanostructures. The methods of synthesis include bottom up and top down. Bottom up method involves the buildup of a material from bottom: atom by atom, molecule by molecule or cluster by cluster while top up method involves breaking of a bulk material to get nano-sized particles. Attrition or milling is a common top-up method while pyrolysis, inert gas condensation, solvothermal reaction, sol-gel method and structured media are typical bottom-up methods used in the synthesis of nanomaterials [1, 2]. The schematic of both top down and bottom up methods is presented in figure 3.1. In this chapter, a brief description of the methods and the characterization techniques used to synthesize and characterize, respectively, nanomaterials investigated in this study are presented. The methods used are co-precipitation and sol-gel and they were used to synthesize rare earths ions (Eu^{3+} and Dy^{3+}) doped ZnO and TiO_2 nanoparticles as well as Eu^{3+} co-doped $ZnO/TiO_2:Dy^{3+}$ nanocomposites. Among other things, the characterization techniques used are X-ray diffraction, scanning electron microscopy, UV-Vis spectrophotometer, photoluminescence/fluorescence spectroscopy, and Fourier transform infrared spectroscopy.

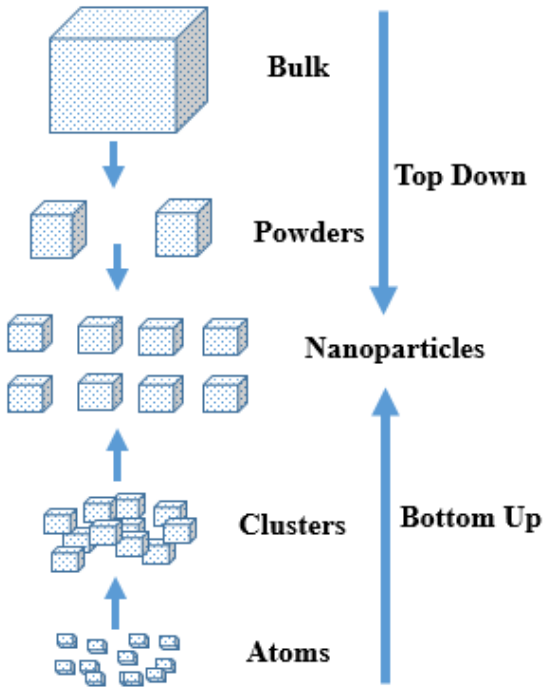

Figure 3.1 Schematic diagram of the bottom-up and top-down approaches for the synthesis of nanomaterials.

3.2 SYNTHESIS METHODS

3.2.1 Co-precipitation method

Co-precipitation synthesis, also known as wet chemical technique is a synthesis method that occur through a reaction between, for example, oxide precursors. It comprises an aqueous solution which contains the precipitate agents (solutes) and a liquid (solvent). The precipitates is separated from the liquid by centrifugation or filtering, dried and thermally decomposed to the desired compound. In co-precipitation method, there are several parameters that have to be controlled to produce required properties of the products. Such parameters are temperature, mixing rate, concentration and degree of alkalinity and acidity or pH of the reaction. By controlling these preparation parameters, this method can produce products with high purity and fine particle size at relatively moderate cost [3]. The basic steps involved in co-precipitation method are shown in the flow diagram of figure 3.2.

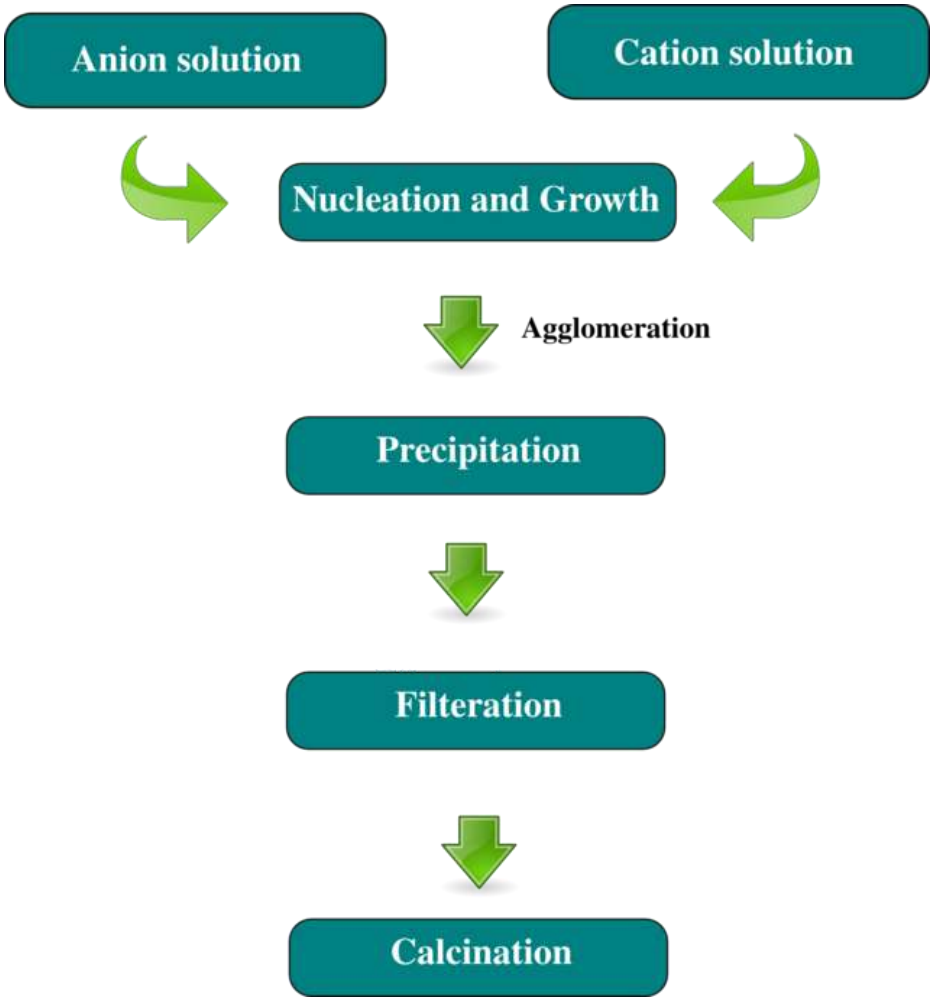

Figure 3.2 Typical co-precipitation method for synthesis of nanomaterials [4].

The schematic diagram for the preparation of Eu^{3+} and Dy^{3+} doped ZnO nanoparticles in this study is shown in figure 3.3. We used a method similar to [5] for synthesis of ZnO nanoparticles doped with Eu^{3+}. ZnO:Eu^{3+} nanoparticle was prepared from analytical grade zinc acetate dihydrate ($Zn(CH_3COO)_3{\cdot}2H_2O$), sodium hydroxide pellets (NaOH) and europium acetate dihydrate ($Eu(CH_3COO)_3{\cdot}2H_2O$). In a typical preparation, zinc acetate dehydrate and europium acetate dehudrate was dissolved in 100 ml de-ionized water followed by stirring for 30 minutes. Sodium hydroxide pellets were dissolved in de-ionized water by stirring for 15 minutes. This solution was added drop-wise to the above prepared zinc solution to control the pH in the solution and we achieved a pH value of 10 using pH strips. A homogeneous solution was further stirred for 1 hour and a precipitate was obtained. The precipitate was centrifugally (5000 rpm) separated and washed several times with de-ionized water to remove excess Zn^{2+} and Na^{+} ions for 15 minutes. Then,

using oven, the precipitate was dried at 60 ℃ overnight and finally the Eu^{3+} doped ZnO nano-powders were obtained. The powder were cooled down to room temperature and ground gently using a pestle and mortar.

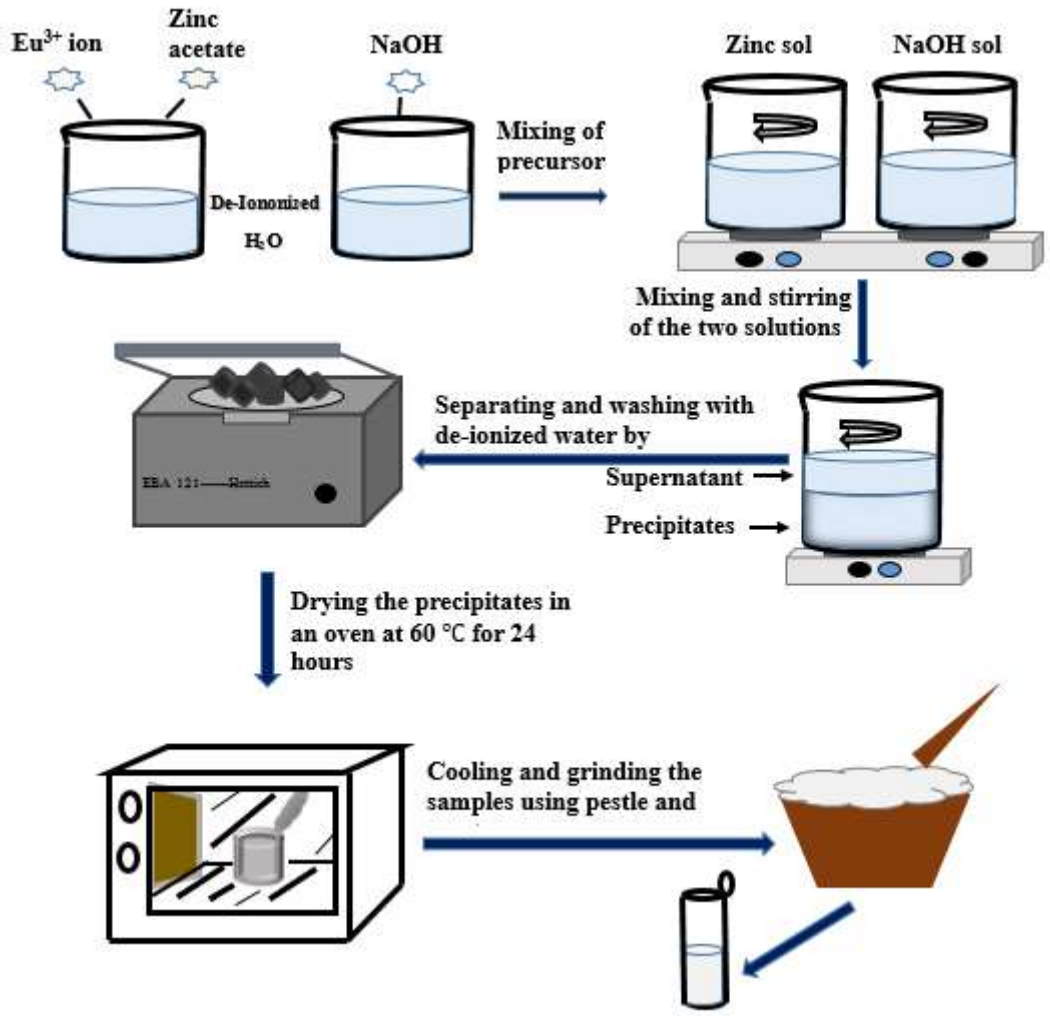

Figure 3.3 Schematic diagram for the synthesis of Eu^{3+} and Dy^{3+} doped ZnO nanoparticles by co-precipitation method.

The schematic diagram of the procedure for the preparation of Eu^{3+} doped TiO_2 nanoparticles by co-precipitation method is presented in figure 3.4. We used a method based on the recipe given by [6] but with some changes due to chemical available. TiO_2:Eu^{3+} nanoparticles were prepared from analytical grade titanium (IV) butoxide, acetic acid (CH_3COOH) ReagentPlus® ≥99% and europium acetate dehydrate ($Eu(CH_3COO)_3 \cdot 2H_2O$). In a typical preparation, a mixture of acetic

acid and ethanol were stirred for 5 min followed by addition of titanium (IV) butoxide and europium acetate dehydrate into the solution under vigorous stirring for 1 hour. After stirring for 1 hour, the reaction was stopped and the resulting grey solution was aged for 2 hours. Then, the solution containing precipitates was dried at 70 ℃ using oven to evaporate the solvent for 24 hours and cooled down to room temperature. Finally the Eu^{3+} activated TiO_2 nano-powders were obtained and ground gently using a pestle and mortar. The powders were annealed at 600 ℃ for 2 hours to improve crystallinity.

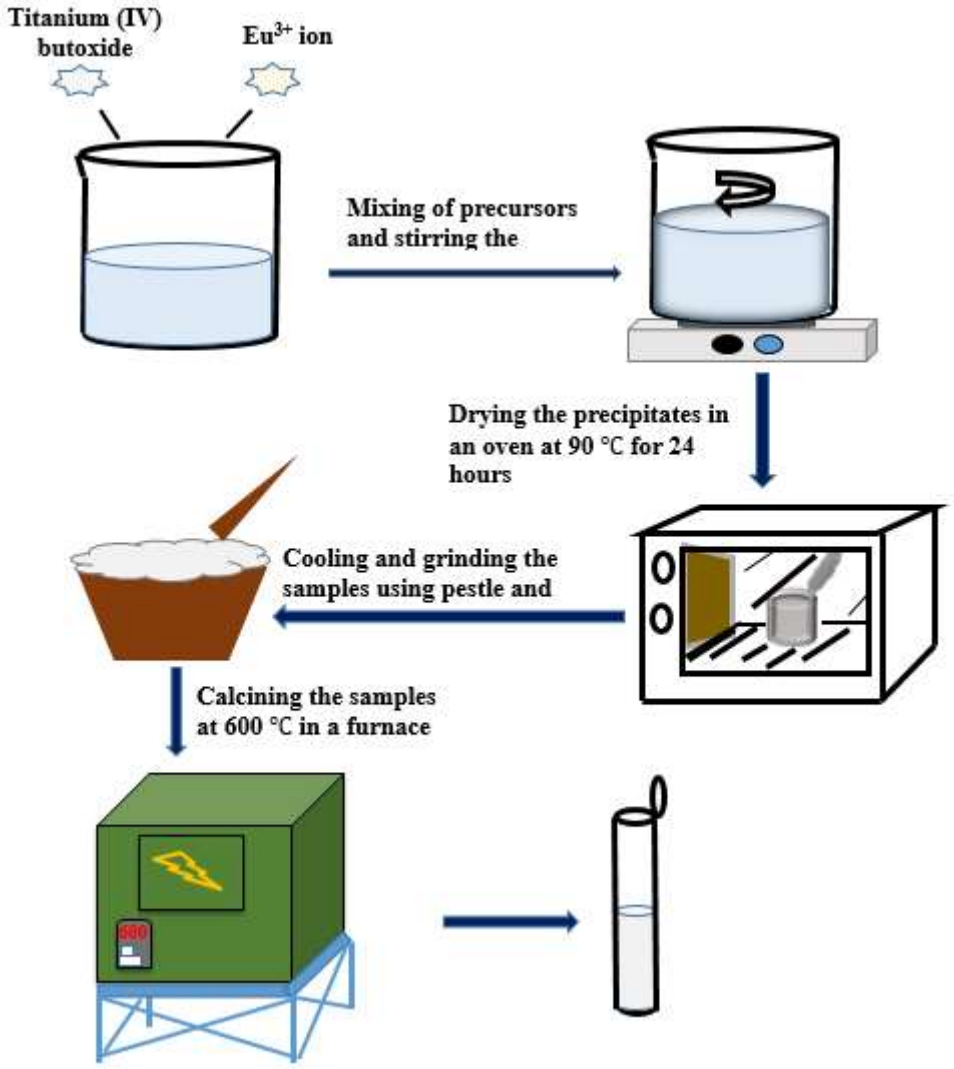

Figure 3.4 Schematic diagram for the synthesis of Dy^{3+} and Eu^{3+} doped TiO_2 nanoparticles by co-precipitation method.

3.2.2. Sol-gel method

Sol-gel, also known as chemical solution deposition is a wet chemical technique widely used in the field of materials science and other disciplines to prepare nanomaterials [1]. It involves the formation of a gel from a solution followed by its dehydration at elevated temperature [2]. The method usually starts from the solution of all compounds in the form of soluble precursors compounds and at a molecular level the mixing of precursors is retained through the formation of a gel. This method involve three steps as follows:

Step 1: Metal organic precursors are normally used in this method where various precursors are mixed together in a solvent to form solution. The multicomponent composition in this solution is a molecular mixture which ensures the homogenization of the precursors/components in the sol-gel method. The solutes in this method may be inorganic nitrates, inorganic chlorides or a wide variety of metal organic molecules while the solvent for the majority of the oxide gel is water or short chain alcohol.

Step 2: This step comprises the formation of a solution and conversion of it to a gel in order to retain the chemical homogeneity of the sample during the desiccation. The gelation of the solution in this case is controlled by pH, temperature and ionic strength of the mixture of the precursors.

Step 3: This step is the last step of the process and it involves desiccation and heat-treatment of the gel of the samples [3].

Sol-gel method has several advantages as follows:

- It is a cheap method and uses relatively low temperature that allows fine control of the chemical composition of the product.
- Small quantities (organic and rare earth metals) can be easily introduced in the solution and end up uniformly dispersed in the final product [2].

The basic steps in sol-gel synthesis of nanomaterials is shown in figure 3.5.

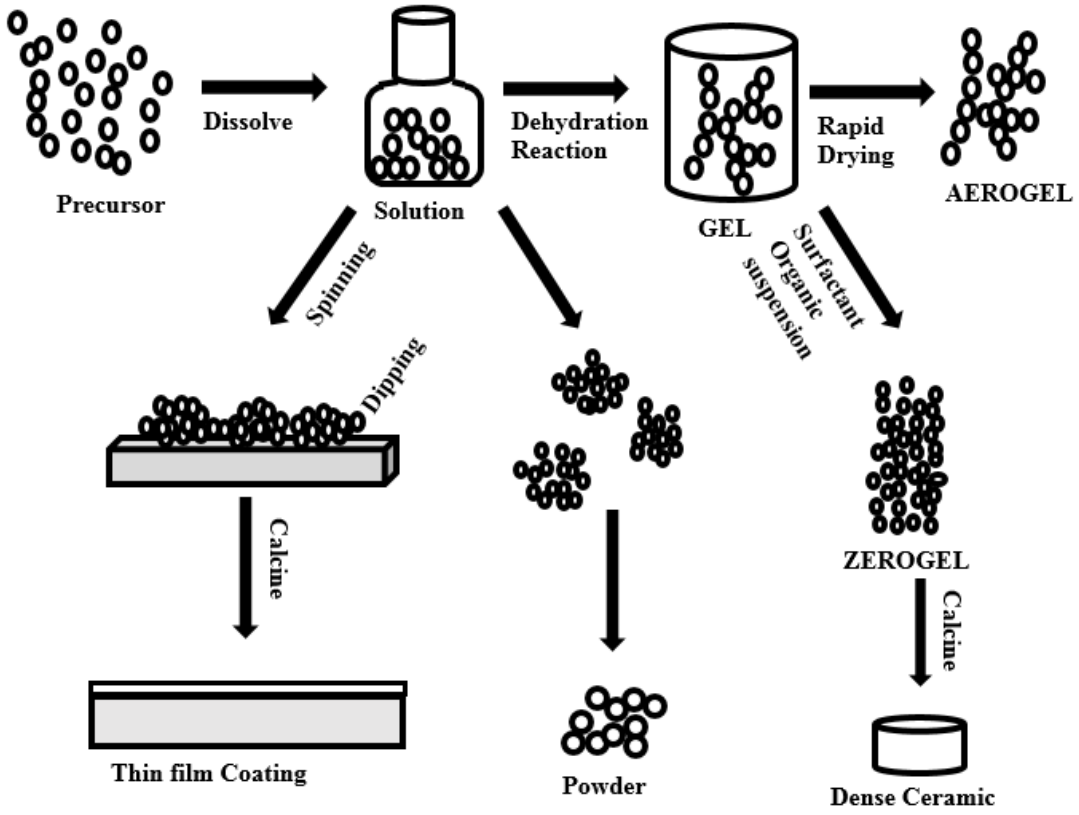

Figure 3.5 Schematic diagram of sol-gel method for synthesis of nanomaterials [7].

The schematic diagram for the preparation of Eu^{3+} co-doped ZnO-TiO_2: Dy^{3+} nanocomposites in this study is shown in figure 3.6. We based synthesis recipe on [8] with some changes due to doping and co-doping with rare earth ions. ZnO-TiO_2: RE (RE = Eu^{3+} and Dy^{3+}) nanocomposites were prepared from analytical grade zinc acetate dehydrate ($Zn(CH_3COO)_2{\cdot}H_2O$), monoethanolamine (C_2H_7NO), titanium (IV) butoxide, nitric acid 70% (HNO_3), lithium hydroxide (LiOH), europium acetate dehydrate ($Eu(CH_3COO)_3{\cdot}2H_2O$) and dysprosium nitrate pentahydrate (($Dy(NO_3)3{\cdot}5H_2O$)). In a typical preparation of nanocomposites, titanium (IV)-butoxide was dissolved in ethanol and the solution was stirred for 30 minutes to form what we refer to as solution 1. Nitric acid was added drop-wise in the solution as a catalyst followed by vigorous stirring for 2 hours. For the preparation of what we refer to as solution 2, zinc acetate dehydrate was dissolved in a mixture of ethanol and monoethanolamine at 60℃. The solution was stirred for 20 minutes. After one day of aging, the two solutions were combined followed by addition of rare earth (RE)

ions precursor solutions and vigorous stirring. Then, the solution was stirred for 2 hours. The molar ratio of Ti: Zn was 1:1. Lithium hydroxide was added into a transparent solution followed by vigorous stirring at 80℃ for 1 hour and a gel was formed. Then, using an oven, the obtained gel was dried at 90°C for 24 hours. The resulting rare-earth ions doped nanocomposite powders were annealed at 600°C for 2 hours.

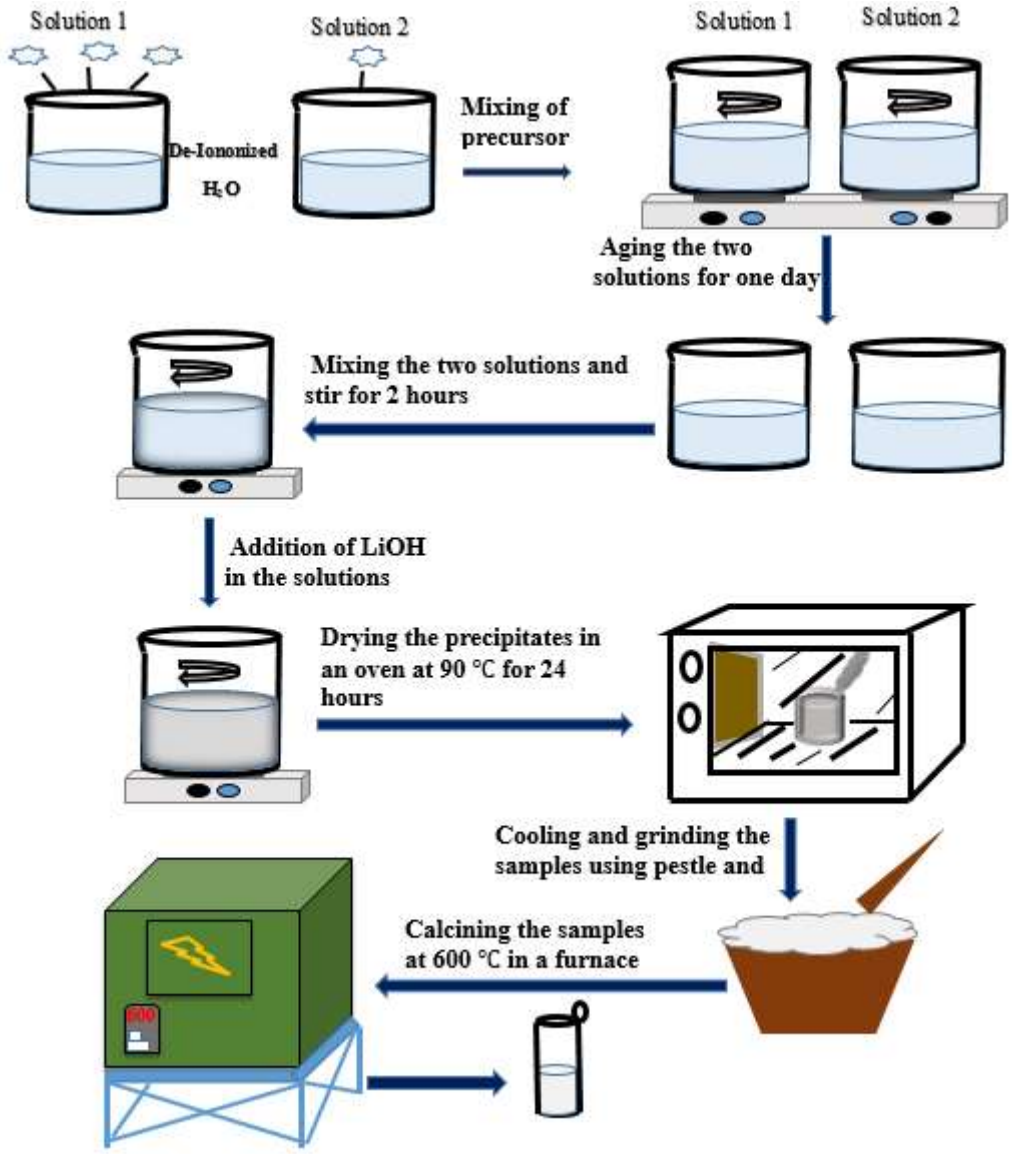

Figure 3.6 Schematic diagram of the sol-gel method for the synthesis of Eu^{3+} and Dy^{3+} co-doped ZnO-TiO_2 nanocomposites.

3.3 Characterization Techniques

3.3.1 Introduction

This section presents an overview and brief description of different research techniques used in this study to characterize the samples: ZnO:Dy^{3+}, ZnO:Eu^{3+}, TiO_2:Dy^{3+}, TiO_2:Eu^{3+}, ZnO/TiO_2:Dy^{3+}, ZnO/TiO_2:Eu^{3+} and ZnO/TiO_2:Dy^{3+}, Eu^{3+}. The techniques include X-ray diffraction (XRD), Scanning electron microscopy (SEM), photoluminescence (PL) spectroscopy, and UV-Vis spectrophotometry and Fourier transform infrared spectrometer (FTIR).

3.3.2 X-Ray Diffraction

XRD is a powerful non-destructive technique used for structural studies of crystalline materials or unknown materials. It is used to identify the phases of the materials, measuring the mean spacing between layers of atoms, determination of crystallite size and the orientation of a single crystal, lattice constants for unknown cubic samples and the degree of the crystallinity of the materials [9, 10]. One of the advantages of the XRD technique is that the sample need not be in an evacuated chamber since the x-rays are not easily absorbed very much by air while its disadvantage is that the interaction with lighter materials is very weak [11]. This characterization tool consists of three basic components which are: an X-ray source/tube, a sample holder, and an X-ray detector. X-rays are generated in a cathode ray tube by heating up a filament to produce electrons which are accelerated towards the specimen by application of certain voltage. Then the target is then bombarded with the electrons generated by cathode ray tube. When these electrons have sufficient energy to knock out the inner shell electrons of the specimen/ target material, characteristics X-ray spectra are produced [9]. However, the interaction of incident x-rays with the specimen produce extreme reflected X-rays by constructive interference when the condition satisfy Bragg's law:

$$n\lambda = 2d_{hkl}\, sin\theta_{hkl} \qquad (1)$$

where n is an integer that indicates the order of the reflection, λ is the wavelength of the incident light rays, d is the distance between lattice planes and θ is the angle of reflection. The value of n from equation 1 is taken as 1 in all calculation because from the set of crystallographic planes, first order reflections (n=1) are always represent the higher order reflections (n > 1). The law

mentioned above relate the wavelength and the x-rays, the incident angle of the beam and the spacing between the crystal lattice planes of an atom as shown if figure 3.7 [12,13].

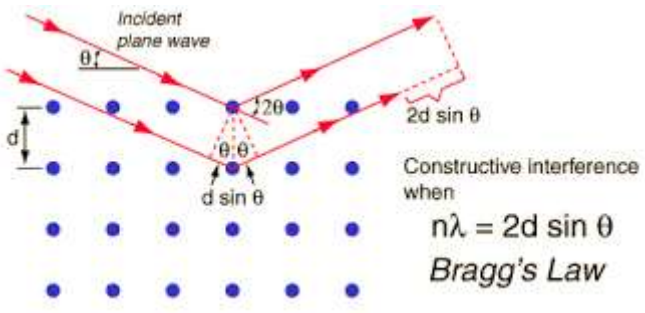

Figure 3.7 Schematic diagram of Bragg reflection from a set of parallel planes [14].

Crystals are regular arrays of atoms and X-ray crystallography is the method used to determine the arrangement of atoms within a crystal by scanning the sample through a range of 2θ angle when the detector is rotated at double angular velocity. The recorded characteristic x-ray spectra consist of several components, the most common being K_α and K_β. There are specific characteristics wavelength for each components such as copper (Cu), iron (Fe), molybdenum (Mo), and chromium (Cr). Copper (Cu) is the most commonly used target material for single crystal and powder diffraction, with the wavelength of Cu K_α radiation = 1.5406 Å [9]. As the x-rays are collimated and directed onto rotating or stationary samples, the rotating detector record the intensity of the reflected x-rays. Constructive interference occurs and diffraction peaks of the sample are observed when the geometry of the incident x-rays impinging on the samples satisfies equation (1). The crystalline phases are determined from the diffraction peaks of the spectrum. The average crystallite size is calculated from the width of the diffraction peaks using the Scherrer's equation:

$$D = \frac{0.89\lambda}{\beta cos\theta} \tag{2}$$

where D is the particle diameter, θ is the diffraction angle and β is the full width at half maximum (FWHM) of an XRD peak [5, 16]. The XRD patterns for this study were recorded in the 2θ angle of 10^o - 80° at a scan speed of 0.02^o s^{-1}, accelerating voltage of 40 kV and current of 40 mA using Bruker D8 Advance x-ray diffractometer equipped with a copper anode x-ray tube. The D8 Advanced AXS GmbH X-ray diffractometer is shown in figure 3.8.

Figure 3.8 Bruker D8 Advance x-ray diffractometer.

3.3.3 Scanning Electron Microscopy

Scanning electron microscopy (SEM) is a powerful tool to observe tiny object in a stereographic image with a magnified scale by scanning them point-by-point from a region of interest with a focused beam of electron. Figure 3.9 shows the basic construction of a SEM. The microscope operate at high vacuum and the high spatial resolution of this microscope make it easy to characterize a wide range of samples at the nanometre and micrometer length scale. During measurements, a beam of electrons are generated in a column above the sample chamber. Electrons are produced by a thermal emission source which is a heated tungsten filaments, or by a field emission cathode and are focused into a small beam by a series of electromagnetic lenses in the SEM column. Accelerated electrons carry significant amounts of kinetic energy whereby this energy is dissipated as a variety of signals produced by electron-sample interactions when the incident electrons are decelerated in the sample [17, 18].

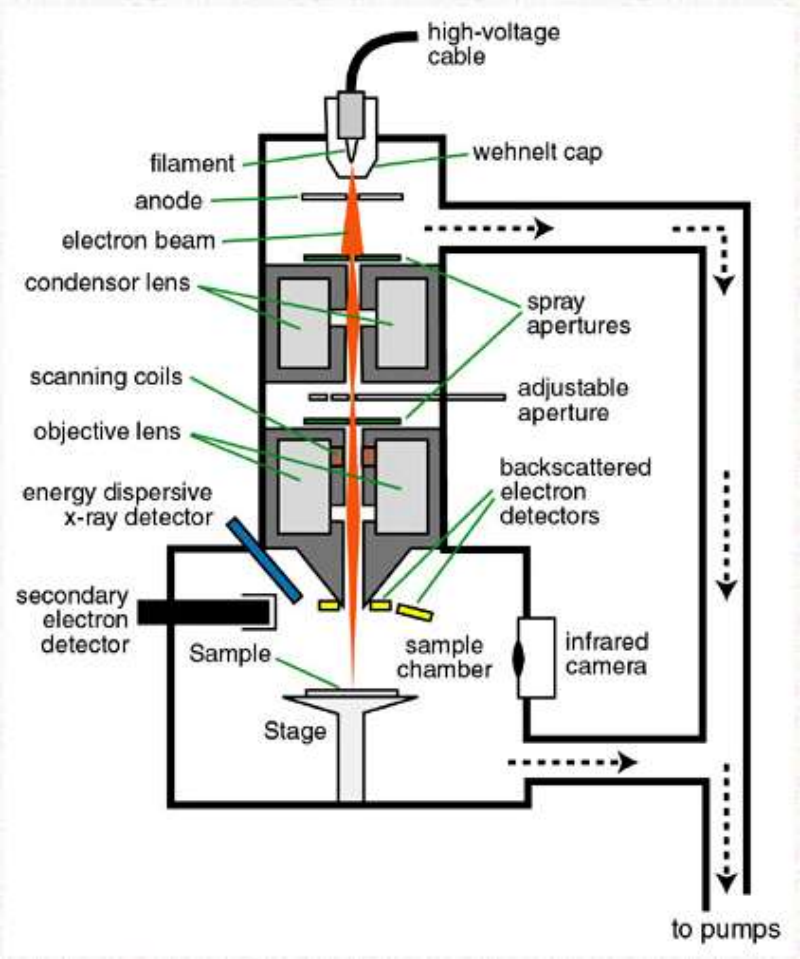

Figure 3.9 Schematic presentation of SEM [19].

When the electron beam hits the specimen on the stage, the specimen produce various kinds of information as shown in Figure 3. Figure 4(a) shows the kinds of signal obtained, whereas figure 3.10(b) shows the volume within the specimen where the signal are generated. These beams are detected, converted into electric signal, and then displayed on a monitor and convert them into images (morphological of compositional image).

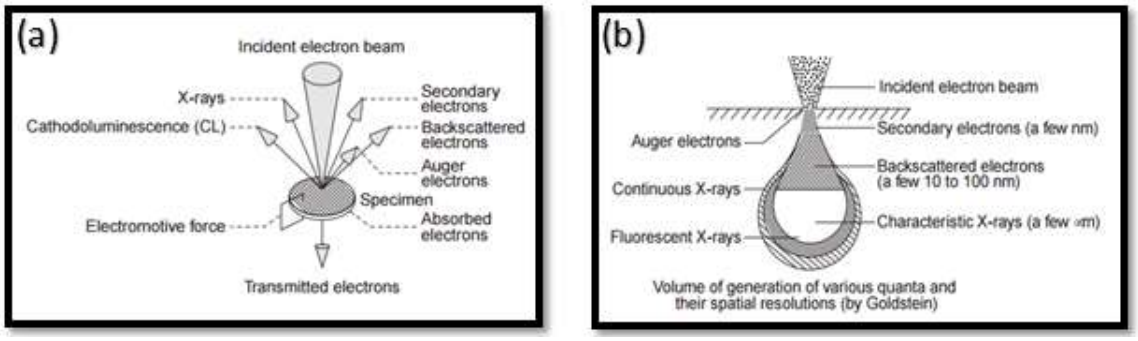

Figure 3.10 The energies produced from electron beam interaction with solid matter [20].

The energy dispersive x-ray spectrometer (EDS) is based on analyzing the chemical composition of the specimen or sample area observed in the SEM by the use of characteristic x-rays. These X-rays are detected by an Energy Dispersive detector which displays the signal as a spectrum of X-rays count rate versus X-ray energy. The characteristics of a specific element made up the sample are therefore displayed by the energies of the characteristics x-rays. The intensities of the characteristics x-ray peaks allows the concentration of the elements to be quantified, the higher the intensity in the spectrum, the more the concentrated the element in the sample will be [21]. Figure 3.11 shows JEOL JSM-7800F Field Emission Scanning Electron Microscope coupled with Oxford Aztec 350X-Max80 EDS in this study.

Figure 3.11 JSM-7800F Field Emission Scanning Electron Microscope

3.3.4 UV-Vis spectroscopy

UV-Vis spectroscopy is the instrument that measures the amount of intensity of light absorbed, transmitted or reflected (electromagnetic radiation) after it passes through the sample solution. Depending on the range of wavelength of light source, this technique can be classified into two different types. The first type is UV-Vis spectrophotometer which uses light over ultraviolet range (185 – 400 nm) and visible range (400 – 700 nm) of electromagnetic radiation spectrum. The second type is IR spectrophotometer which uses light over the infrared range (700 – 15000 nm) of electromagnetic radiation spectrum [22]. The basic setup of a spectrophotometer include a light source, diffraction grating in a monochromator to separate the different wavelength of light, sample holder and a detector. The spectrophotometer usually consist of two radiation sources, Deuterium arc lamp for ultraviolet region and Tungsten lamp for visible region respectively. The detector is a photomultiplier (PMT) or photodiode and it is used to convert the light signal into an electrical signal. The basic schematic diagram of UV-visible spectrophotometer is shown in figure 3.12.

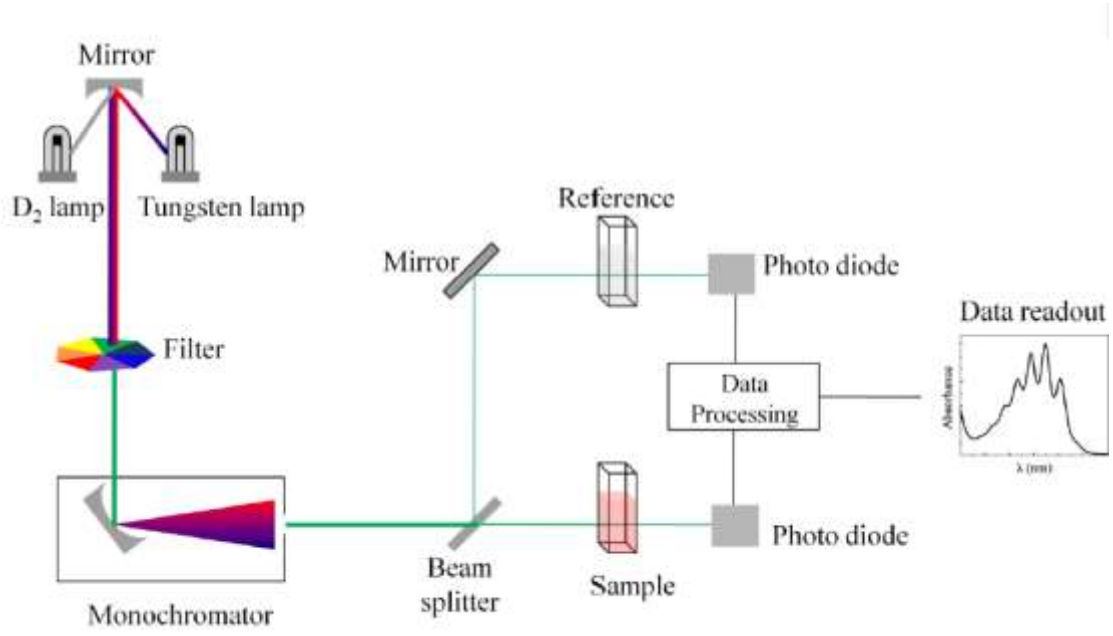

Figure 3.12 Schematic representation of UV- visible spectrophotometer [23].

When the light passes through the sample, its intensity (I) is measured and compared to intensity of the light before it passes through the sample (I_o). The ratio I/I_o is then called transmittance and

is expressed as a percentage (%T). Equation 3 shows how the absorbance (*A*) is related to transmittance.

$$A = -log\left(\frac{\%T}{100\%}\right) \tag{3}$$

The spectrophotometer can also measure the reflectance and the measured intensity of light reflected from a sample (*I*) is compared to the intensity of the light reflected from the reference material (I_o). In this case, the ratio I/I_o is called reflectance and expressed as a percentage (%R) [23]. The UV-Vis absorption or reflectance spectra is being used to determine the optical band gap of the material. The band gap energy of a material is determined by extrapolating the linear portion through the plot of the following equation for semiconductors.

$$\alpha h\nu = A\,(h\nu - E_g)^{\,n} \tag{4}$$

where α is absorption coefficient, h is Planck's constant, ν is frequency of the incident photons, A is a proportional constant, E_g is band gap energy, and n denotes optical electronic transition. The value of n for allowed direct, allowed indirect, direct forbidden and indirect forbidden electronic transition are 1/2, 2, 3/2, and 3 respectively. Band gap is the difference in energy between the top of the valence band filled with electrons and the bottom of the conduction band devoid of electrons. The diffuse reflectance data in this study were converted to absorption coefficient (α) using Kubelka-Munk analysis.

$$F(R) = \frac{(1-R)^2}{2R} \tag{5}$$

where *F(R)* is usually termed Kubelka-Munk function and *R* is the fractional reflectance. The reflectance data was divided by 100% to get rid of percentages and the absorption coefficient (α) in equation 4 is proportional to the vertical axis (*F(R)*) of Kubelka-Munk function. Therefore, the absorption coefficient in Tauc's plot is then substituted with *F(R)* [25 - 26]. The diffuse reflectance spectra presented in this study were recorded by Perkin Elmer Lambda 950 UV-Vis spectrophotometer with an integrating sphere as shown in figure 3.13.

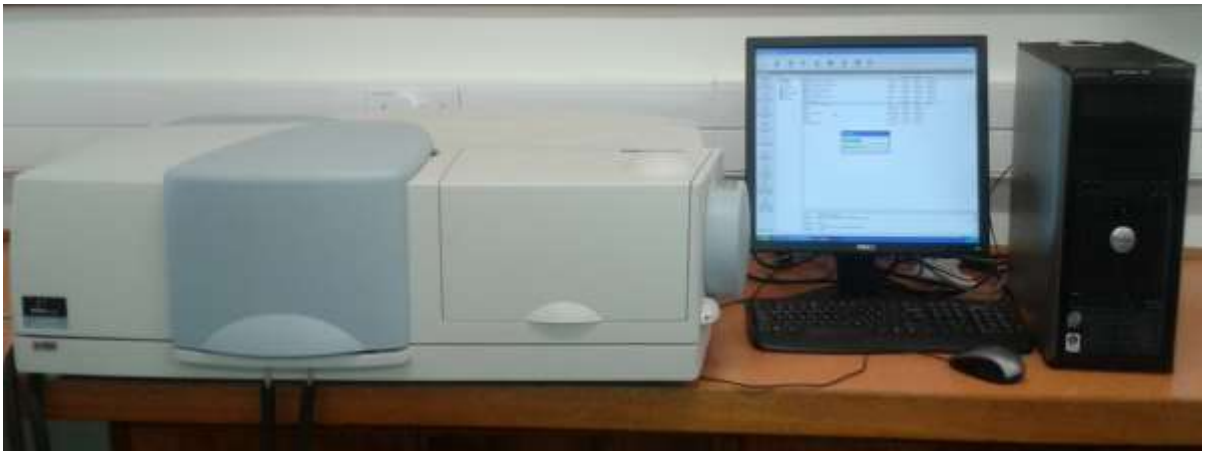

Figure 3.13 Lambda 950 UV-Vis spectrophotometer

3.3.5 Photoluminescence spectroscopy (Helium-Cadmium laser)

The Helium-Cadmium (He-Cd) laser is one of a well-known class of lasers that uses helium in conjunction with a metal with a low vaporization temperature. The basic elements of He-Cd laser consist of a tube, terminated by two Brewster angle windows with two laser mirrors mounted separately from the tube. In a typical setup of He-Cd laser, the tube is filled with helium gas, cadmium reservoir and a heater located near the main anode as shown in figure 3.14. The heater is used to evaporate the metal. The desired vapour pressure of Cd atoms in the tube is produced when the temperature of the cadmium reservoir is raised to higher value (~ 250℃). He-Cd laser can give output lines of laser beam either in violet blue (442 nm) or ultraviolet (325 nm) with a powerful output power of 50-100 mW [27, 28].

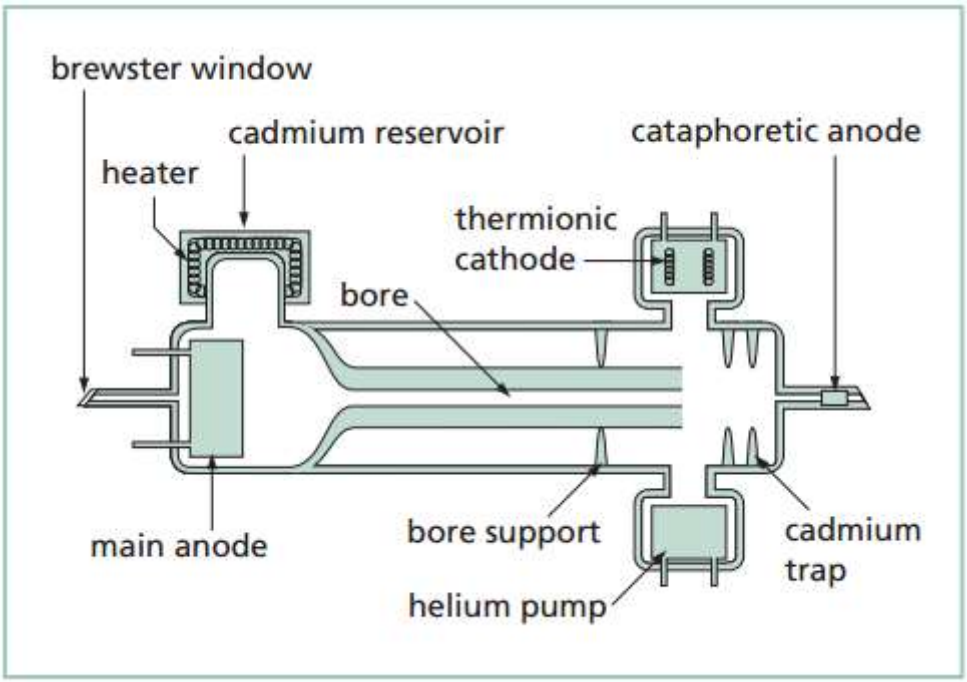

Figure 3.14 The typical cavity structure of He-Cd Laser [29].

A schematic diagram of photoluminescence measurement setup used in this study is presented in figure 3.15. All PL measurements in this work were made at room temperature. He-Cd laser beam (wavelength 325 nm) was used as excitation source and the detector used was Gallium Arsenide. During measurements, the laser beam was directed to the sample by using optical lenses and mirrors, followed by the chopper that was used to ensure that the light beam is sent in packets. The luminescence from the sample was collected by the optical lenses and focused onto the spectrometer slit through a long-pass filter. The spectrometer consist of an entrance slit, two diffraction gratings (1800 and 950 lines per mm) and exit slit. The luminescence is dispersed by diffraction grating in spectrometer whereby a certain wavelength passes through the exit slits and is incident on a gallium Arsenide detector. He-Cd laser system, shown in figure 3.15 used in this study was from Nelson Mandela Metropolitan University (NMMU) in Port Elizabeth. A schematic drawing of the He-Cd laser equipment for photoluminescence is shown in figure 3.15.

Figure 3.15 PL system used to investigate the luminescent properties of the samples.

3.3.6 Fluorescence Spectrophotometry

Fluorescence Spectrophotometry is an important tool for studying the electronic transitions following excitation by a beam of light. Typically, the sample is excited by beam of light where it is absorbed and when they spontaneously de-excited, they emit luminescence (a radiative process) or may not (a non-radiative process). The luminescence occurs in a variety of matter under many different circumstances and is called photoluminescence as the optical excitation of the sample is performed by light. During the measurements, excitation is provided by the light with an energy much larger than the optical bandgap of the material [30]. The energy of photoluminescence relates the difference in energy levels between the two electrons states involved in the transition between the excited and the equilibrium state [31]. The emission spectrum is obtained by measuring and

plotting the intensity of light of sample as a function of wavelength. Figure 3.16 shows an outline of the schematic diagram of general basic equipment for PL.

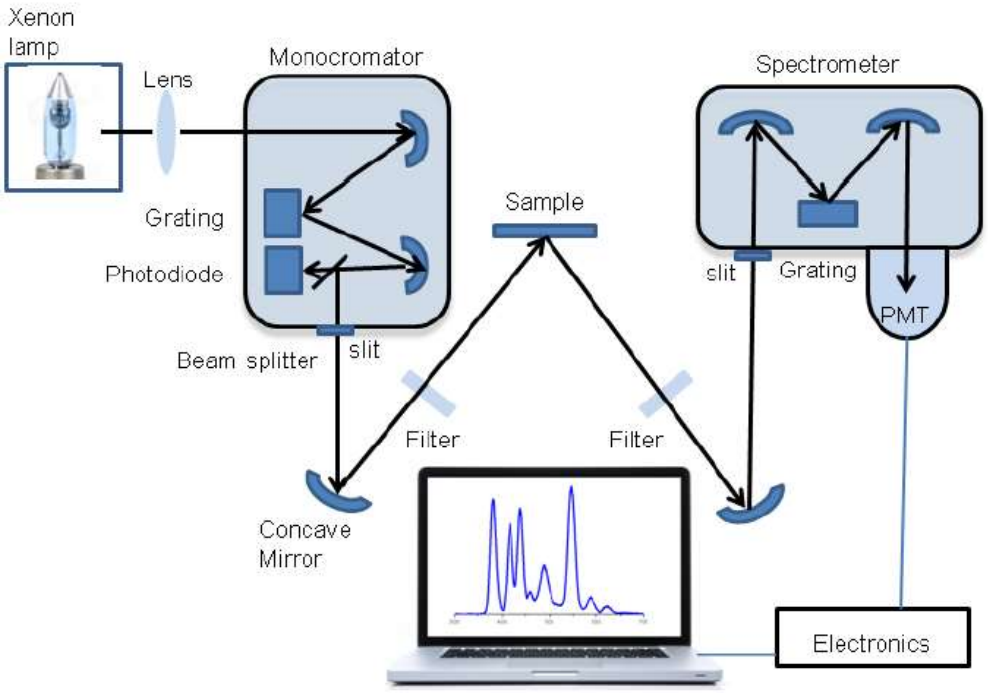

Figure 3.16 Schematic diagram of photoluminescence spectrometer [32].

The basic elements of PL system consist of xenon lamp which is collected by an elliptical mirror and directed to the entrance slit of a monochromator. One of the advantages of Xenon lamp is the high intensity at all wavelength above 250 nm. The luminescence from the sample is collected by a lens and is focused onto the spectrometer slit through a long-pass filter and the detector used is photomultiplier tube (PMT) [32]. The output of the PMT signal is amplified and recorded. The emission and excitation spectra for the samples were measured using a Cary Eclipse fluorescence spectrophotometer as presented in figure 3.17. All photoluminescence measurements were made using phosphorescence mode at room temperature.

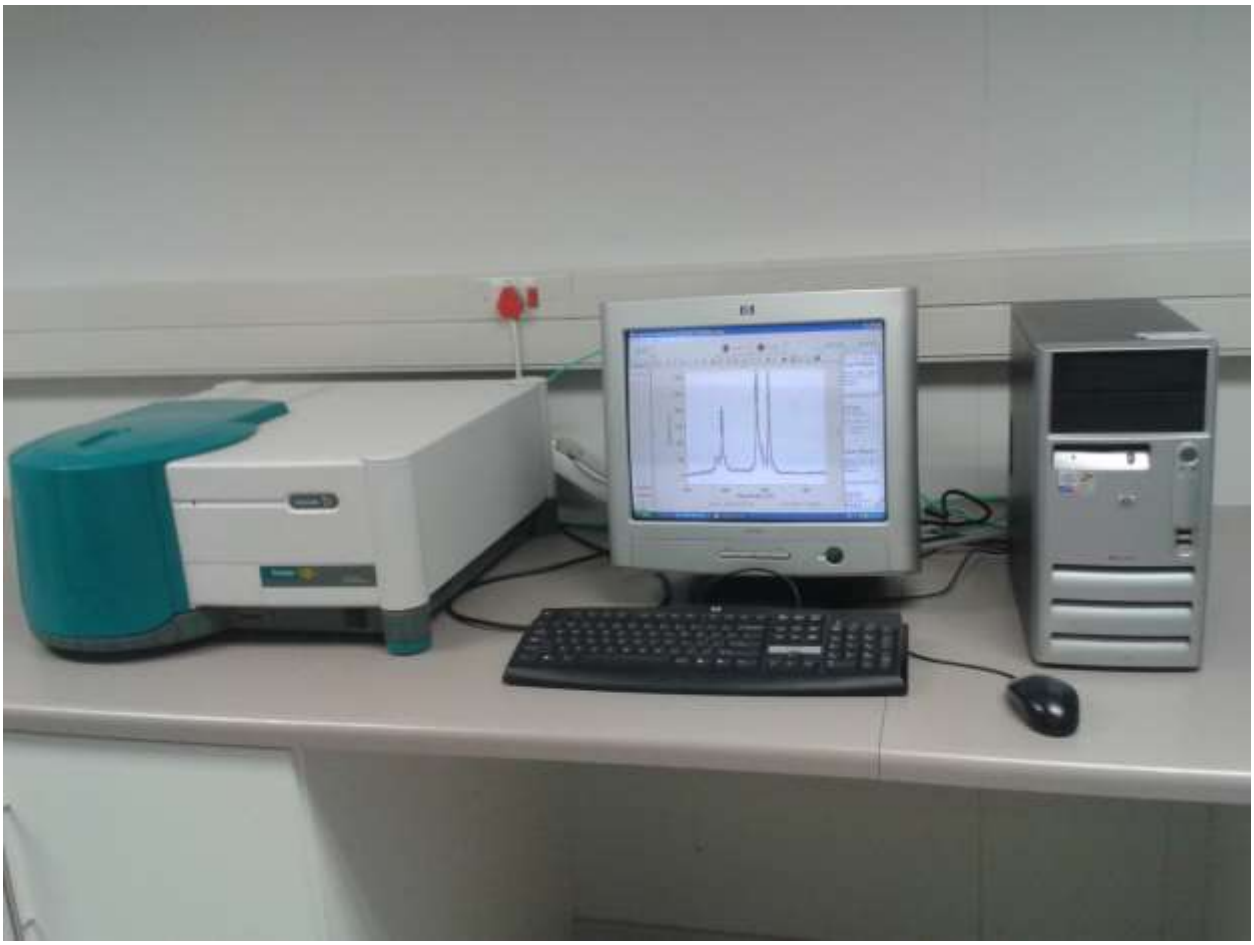

Figure 3.17 Cary-Eclipse fluorescence spectrophotometer

3.3.7 Fourier transform infrared (FTIR) spectrometer

Fourier-transform infrared (FTIR) spectroscopy is based on identifying chemicals that are either organic or inorganic and it has a broad application in many fields of science, forensic and engineering. It is an easy way to identify types of chemical bonds or presence of certain functional group in a molecule by producing an infrared absorption spectrum that is a molecular "fingerprint" and the wavelength of absorbed light is characteristic of the chemical bonds. Also, one can use the technique to quantitate some components of unknown mixture and for analysis of materials in gases, solids and liquids phases. There are several specific frequencies at which each molecular bonds vibrate depending on the type of the bonds and the elements [33].

The FTIR spectroscopy consist of a source (electromagnetic radiation), sample compartment, interferometer, detector, amplifier, and an A/D converter. In FTIR spectroscopy, the source in the IR region is directed at the sample. There is an aperture that the beam passes through and it controls the amount of energy presented to the sample. This beam enters the interferometer and the resulting interferogram signals exit the interferometer. Then, the radiation is absorbed or transmitted when the frequency of the radiation energy matches the vibrational frequency of the sample. The relationship between frequency and the wavelength is

$$\nu = \frac{c}{\lambda} \tag{5}$$

where ν is the frequency, c is the speed of light and λ is the wavelength. For wavenumber scale,

$$\bar{\upsilon} = \frac{\nu}{c} \tag{6}$$

And

$$\bar{\upsilon} = \frac{1}{\lambda[cm]} \tag{7}$$

Therefore, energy content and vibrational frequency of a sample is directly proportional to the wavenumber scale

$$E = hcW\ [cm^{-1}] \tag{8}$$

where E is vibrational energy level, h is Planck's constants and W is wavenumber scale respectively. The beam finally detected by the detector for final measurements. The measured signal is then amplified and converted to digital signal by amplifier and analog-to-digital converter. Eventually, the measured signal is transferred to computer where Fourier transformation takes place [34-36]. The preparation method for pellets used was the KBr pellet method. Spectrophotometric-grade KBr was first taken from the desiccator and dried overnight in the oven for 70℃. 0.20g of dried spectrophotometric-grade KBr and 0.01g of solid sample were wrapped with aluminium foil in a sample holder and placed in the oven for half an hour. The mixture was then mixed with a dried grinding machine for 20 seconds. The mixture was transferred into a clean dried mortar and mixed gently with clean pestle to ensure a homogenous mixture of KBr and the

solid sample and put into a stainless steel pellet-forming die. The stainless steel die were placed in the hydraulic press and 9 tons of pressure were applied gradually (3 to 5 minutes) using a big handle. After 10 minutes, the die was removed from the hydraulic press and the pressed KBr disks were transferred into appropriate disk holder using tweezers for IR analysis. The basic block diagram of an FTIR spectroscopy is presented in figure 3.18.

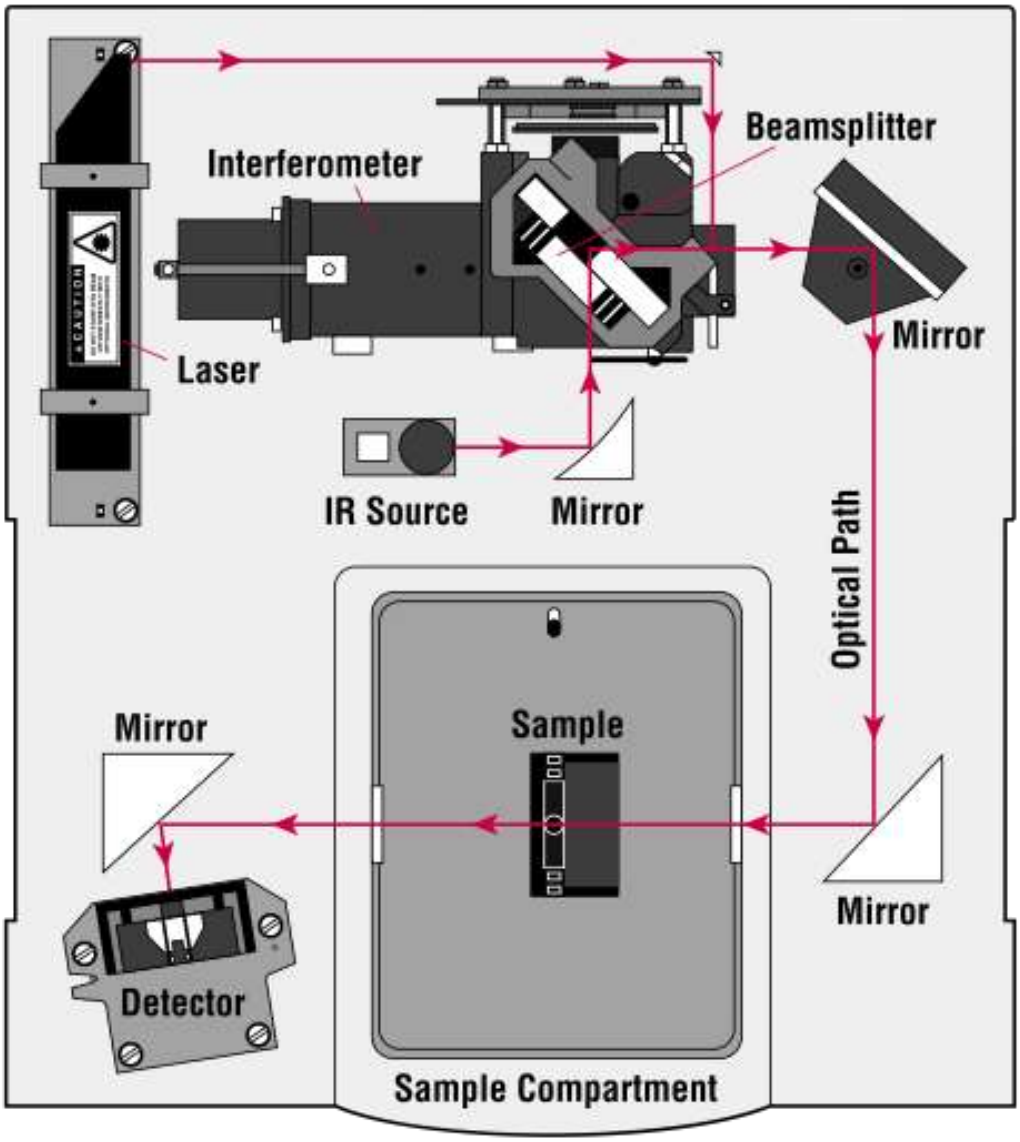

Figure 3.18 A schematic diagram of FTIR spectroscopy [34].

In this study, Nicolet 6700 Fourier-transform infrared (FTIR) spectrometer with Raman module was used to measure the vibrational frequency modes of the samples. The spectrometer is shown in figure 3.19.

Figure 3.19 Nicolet Continuum FT-IR microscope.

3.4 References

[1] Nanotechnology, [online], Available from http://www.gitam.edu/eresource/nano/nanotechnology/nanotechnology%20web%201.htm [accessed on 15 July 2015].

[2] Synthesis of Nanoparticles, [online], Available from http://www.news-medical.net/health/Synthesis-of-Nanoparticles.aspx [accessed on 15 July 2015]

[3] A. Pacthak and P. Pramanik, *Nano-Particles of oxides through Chemical Method,* PINSA (2001) 67, 47-70.

[4] Coprecipitation method, [online], Available from http://www.wikiwand.com/en/Coprecipitation [accessed on 15 July 2015]

[5] S.S. Kulkarni and M.D. Shirsat. International Journal of advanced Research in Physics Science, 2(1) **(2015)** 14-18.

[6] X. Meng, C. Han, F. Wu and J. Li. Journal of Alloy and Compound, 253 **(2012)** 210-213.

[7] Sol-gel method, [online], Available from http://www.gitam.edu/eresource/nano/NANOTECHNOLOGY/bottamup%20app.htm [accessed on 26 September 2015]

[8] N. Naseri, M. Yousefi, O. Moradlou and A.Z. Moshfegh. Phys. Chem. Chem. Phys., 13 **(2011)** 4239–4242.

[9] X-ray diffraction spectroscopy, [online]. Available from http://serc.carleton.edu/research_education/geochemsheets/techniques/XRD.html [Accessed 09 June 2015].

[10] X-ray diffraction spectroscopy, [online]. Available from http://www.matter.org.uk/diffraction/x-ray/default.htm [accessed 09 June 2015].

[11] X-ray diffraction spectroscopy, [online]. Available from http://www.slideshare.net/hephz/ppppppptttttt-x-ray [accessed 09 June 2015].

[12] X-ray diffraction spectroscopy, [online]. Available from http://en.openei.org/wiki/X-Ray_Diffraction_%28XRD%29 [accessed 09 June 2015].

[13] V.K. Pecharsky and P.Y. Zavalij, *Fundamentals of Powder Diffraction and Structural Characterization of Materials, 2nd Ed.,* Springer (New York, **2009**).

[14] X-ray diffraction spectroscopy, [online]. Available from http://hyperphysics.phy-astr.gsu.edu/hbase/quantum/bragg.html [accessed 11 June 2015].

[15] R.E. Kroon. Nanoscience and the Scherrer equation versus the 'Scherrer–Gottingen equation'. S Afr J Sci. 2013;109(5/6), Art. #a0019, 2 pages. http://dx.doi. org/10.1590/sajs.2013/a0019.
[16] M.N. Rahaman, *Ceramic Processing and Sintering, 2nd Ed.,* Marcel Dekker (New York, 2005).
[17] Scanning electron microscopy, [online]. Available from http://mee-inc.com/sem.html [accessed 22 June 2015].
[18] R. Bhardwaj and V. Gupta*, Characterization Techniques for Nano-Materials in Nano-electronics: A Review*, 2nd International Conference on Role of Technology in Nation Building (India, **2013**).
[19] Planetary Materials Microanalysis Facility, [online] http://www4.nau.edu/microanalysis/Microprobe-SEM/Instrumentation.html, [accessed 22 June 2015].
[20] JEOL Serving Advanced Technology, [online], Available from http://www.jeolusa.com/DesktopModules/Bring2mind/DMX/Download.aspx?EntryId=599&Command=Core_Download&PortalId=2&TabId=320, [accessed 22 June 2015].
[21] MyScope training for advanced research, [online], Available from http://www.ammrf.org.au/myscope/analysis/eds/, [accessed 24 June 2015].
[22] F.M. Sanda, M.E. Victor, T.A. Monica and C. Alina, *Spectrophotometric measurements techniques for fermentation process*, 1st Part, Base theory for UV-Vis spectrophotometric measurement (Hungary-Romania and Europian Union, 2012).
[23] Ultraviolet–visible spectroscopy, [online], Available from https://en.wikipedia.org/wiki/Ultraviolet%E2%80%93visible_spectroscopy, [accessed 03 July 2015].
[24] SHIMADZU, [online], Available from https://www.google.co.za/url?sa=t&rct=j&q=&esrc=s&source=web&cd=2&cad=rja&uact=8&ved=0ahUKEwiy7JuN3LXKAhXrnIMKHU37B5AQFgggMAE&url=https%3A%2F%2Fwww.researchgate.net%2Ffile.PostFileLoader.html%3Fid%3D5450e19acf57d7d61e8b45f4%26assetKey%3DAS%253A272468059590658%2540144197285561 3&usg=AFQjCNGLUgCvVAuiw933B0rfy2SfWHAxOw, [accessed 19 January 2016].
[25] Z.M. Gibbs, A. LaLonde and G.F. Snyder. New Journal of Physics, 15 **(2013)**

075020(18pp).
[26] R. Lopez and R. Gomez, J Sol-Gel Sci Technol, 61(**2012**), 1–7.
[27] M.A. Lephoto, O.M Ntwaeaborwa, B.M. Mothudi and H.C Swart. Master's thesis, University of the Free State, Republic of South Africa, **2011**, pp 47-48.
[28] M.A. Tshabalala, B.F. Dejene and H.C Swart. Master's thesis, University of the Free State, Republic of South Africa, **2011**, pp 30.
[29] Basic Laser Principle, [online]. Available form http://www.bgu.ac.il/~glevi/website/Guides/Lasers.pdf [accessed 13 August 2015].
[30] Optique coherente et non lineaire, [online], Available from http://www.lpa.ens.fr/spip.php?article266&lang=fr [accessed 06 July 2015].
[31] D. Heiman, *Photoluminescence Spectroscopy*, Physics of Waves and Optics (Northeastern University, **2004**).
[32] W.A.I Tabaza, R. E. Kroon and H.C. Swart. Unpublished PhD thesis. University of the Free State, Republic of South Africa, **2014**.
[33] Research and development, [online], Available from http://iitk.ac.in/dordold/index.php?option=com_content&view=article&id=131:fourier-transform-infrared-spectrometer-ftir&catid=221&Itemid=240 [accessed 06 July 2015].
[34] Fourier Transform Infrared Spectroscopy (FTIR), [online], Available from http://chemwiki.ucdavis.edu/Physical_Chemistry/Spectroscopy/Vibrational_Spectroscopy/Infrared_Spectroscopy/How_an_FTIR_Spectrometer_Operates [accessed 07 July 2015].
[35] Fourier Transform Infrared Spectroscopy (FTIR), [online], Available from http://mmrc.caltech.edu/FTIR/FTIRintro.pdf [accessed 07 July 2015].
[36] Fourier Transform Infrared Spectroscopy (FTIR), [online], Available from http://www.kstreetstudio.com/science/experiments/files/FTIR.pdf.

Chapter 4 Co-precipitation preparation and luminescent properties of TiO_2: Eu^{3+} nanoparticles

4.1 Introduction

Titanium dioxide (TiO_2) can crystalize into four crystalline polymorphs such as stable rutile, metastable anatase brookite, and monoclinic TiO_2. Among them, rutile and anatase are most widely studied phases and titanium oxide consist of a mixture of both amorphous and crystalline phases. The amorphous TiO_2 gel that form during aging process crystallizes into anatase while phase transformation from anatase to rutile occurs during annealing at around 400 - 1200 ℃ during which it undergoes substantial aggregation and grain growth. The transition temperature of phase transformation from anatase to rutile depend on the different method used, raw materials and the processing methods for TiO_2 preparation [1, 2]. Anatase and rutile have common primary tetragonal crystal structures, the TiO_6 octahedron which is slightly distorted from the perfect octahedron as shown in Figure 4.1 drawn using the diamond software [3]. The two equivalent bond lengths in apical direction (Ti – O_1 and Ti – O_2) are not equal with four equivalent bond lengths in equatorial direction (Ti – O_3, Ti – O_4, Ti – O_5 and Ti – O_6) in both TiO_6 octahedrons. These phases differ in terms of the length of the bonds. The stacking arrangements of the TiO_2 crystal are also different for the two phases. In the rutile phase, each TiO_6 octahedron has 10 neighbours in which two of them share edges and the other eight share corners along the [110] direction which the stacked along axis alternating by 90°. In the anatase phase, each TiO_6 octahedron has 8 neighbours in which four of them share edges and the other four share corners and all corner-sharing lies along the [001] direction. In the TiO_2 polymorphs, anatase phase can be considered as a layered structure with more empty room just outside its octahedron whereby the layers are linked with each other by soft apical Ti-O bonds. The different stacking arrangement of the TiO_2 results in different space groups for, $P4_2/mnm$ (D_{4h}^{14}) for rutile phase and $I4_1/amd$ (D_{4h}^{19}) for anatase phase. Other polymorphs of TiO_2 have different Ti-O bond strengths, stacking arrangements of the TiO_2

octahedron and the space groups [4, 5]. Luminescent nanomaterials (nanophosphors) have received a great deal of attention in applications such as display monitors, lasers and many more. A variety of semiconducting nanomaterials have been investigated as the host lattice for rare-earth (RE) ions because of their tunable optical properties [6-8]. Among these semiconductors, TiO_2 is a good candidate for rare earth dopant ions due to high transparency in the visible-light region [9]. Europium (Eu^{3+}) is a well-known rare-earth ion for red luminescence that has unique characteristics applicable in light emitting devices because of its sharp and intense luminescence at room temperature [10]. This chapter presents a preparation method, structural and optical properties of TiO_2 doped with Eu^{3+} ions.

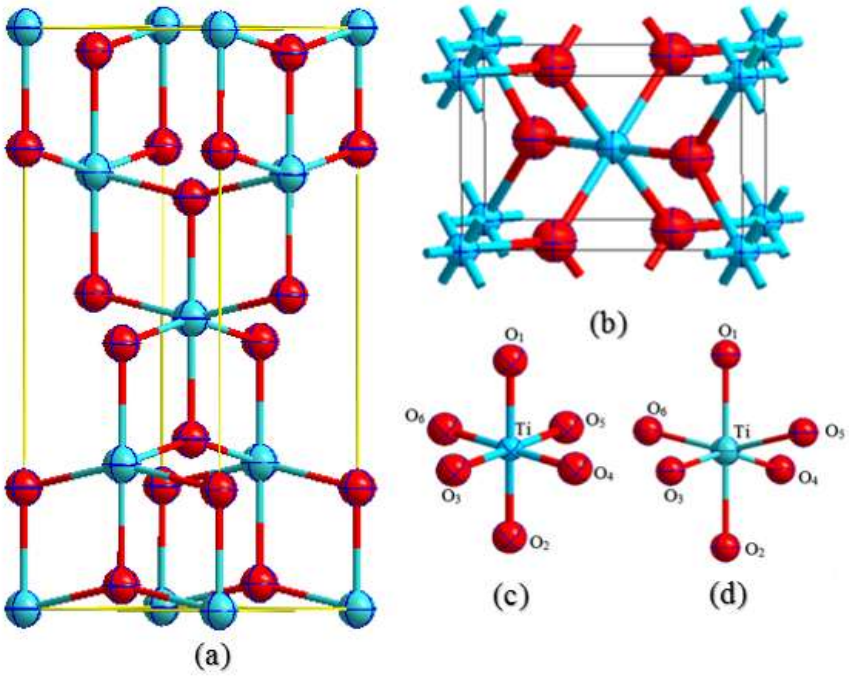

Figure 4.1 Schematic diagram of tetragonal crystal cells of (a) anatase and (b) rutile. Schematic diagram of atomic structure of TiO_6 octahedron in (c) rutile and (d) anatase.

4.2 Materials and experimental procedure

TiO_2:Eu^{3+} nanoparticulate phosphors were synthesized from analytical grade titanium (IV) butoxide ($Ti(OCH_2CH_2CH_2CH_3)_4$), acetic acid (CH_3COOH) and europium acetate dehydrate ($Eu(CH_3COO)_3{\cdot}2H_2O$). In a typical preparation, a mixture of acetic acid and ethanol were stirred

for 5 min followed by addition of titanium (IV) butoxide and europium acetate hydrate into the solution under vigorous stirring for 1 hour. After stirring for 1 hour, the reaction was stopped and the resulting grey solution was aged for 2 hours. The sedimented solution was dried at 70 ℃ in an oven for 24 hours to evaporate the solvent and the precipitates was cooled down at room temperature. The TiO_2:Eu^{3+} powders were ground gently using a pestle and mortar. The resulting powders were annealed at 600 ℃ for 2 hours to improve their crystallinity. The concentration of Eu^{3+} was varied from 1 to 5 mol%.

4.3 Results and discussion

4.3.1 Structural and morphological analysis

The X-ray diffraction (XRD) patterns of TiO_2:Eu^{3+} with difference molar concentrations of Eu^{3+} are shown in Figure 4.2. The undoped TiO_2 consist of mixed crystalline phases of anatase (JCPDS card # 21-1272) and rutile (JCPDS card # 75-1753). The XRD patterns of TiO_2 doped with Eu^{3+} ions were not so different from those pure TiO_2 except phase transformation and the dominant phase is anatase. This suggest that by incorporation of Eu^{3+} ions into TiO_2 have shown the effects on phases transformation in crystalline structure of TiO_2 nanoparticles, and no new diffraction peak of crystalline Eu_2O_3 are produced by doping. This is due to the fact that the addition of Eu^{3+} ions into TiO_2 stabilized anatase phase with an increase of concentration of Eu^{3+} ions [11]. Figure 4.3 (a) depicts the XRD maximum intensity perceived from the relative intensities of the anatase (101) and rutile (110) phases as a function of Eu^{3+} concentration. Without Eu^{3+} doping, TiO_2 nanoparticle contains more rutile phase and less anatase phase. Similarly, Eu^{3+} doped TiO_2 nanoparticle contains more anatase and less rutile which decreased steadily with an increase in Eu^{3+} concentration. TiO_2: Eu^{3+} nanoparticle at high concentration showed the presence of broad diffraction peaks corresponding to anatase phase. Figure 4.3 (b) shows the full with at half maximum as a function of Eu^{3+} concentration for (110) diffraction peak of anatase phase. The broadening of the diffraction peaks are probably due to the reduction in the grain sizes containing many structural defects with an increase in Eu^{3+} contents [12].

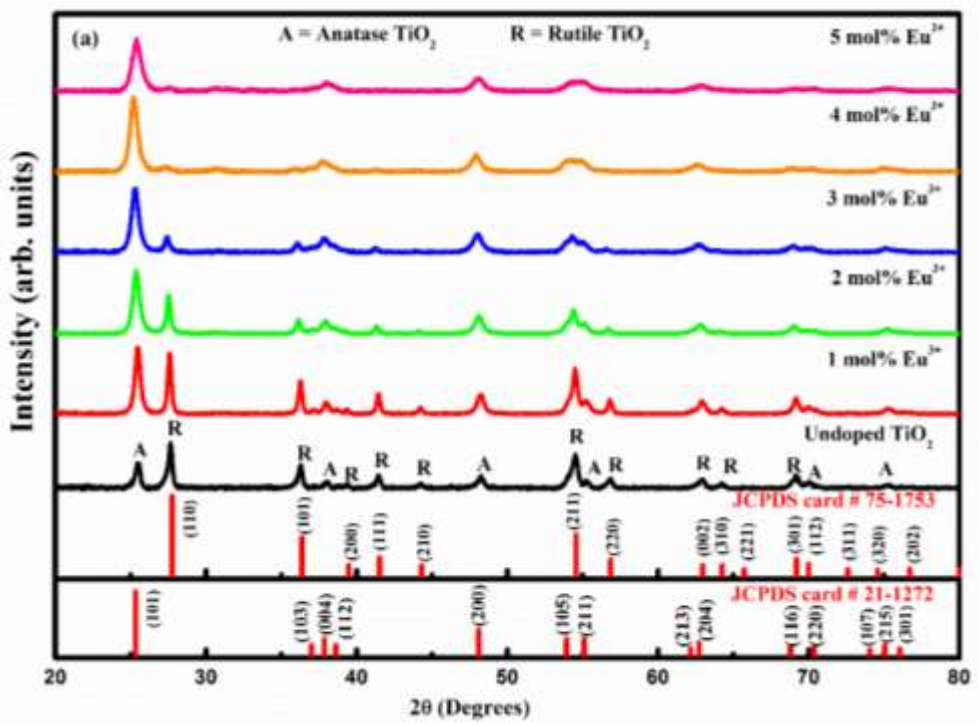

Figure 4.2 XRD pattern of undoped and Eu^{3+}-doped TiO_2 nanoparticle annealed at 600℃.

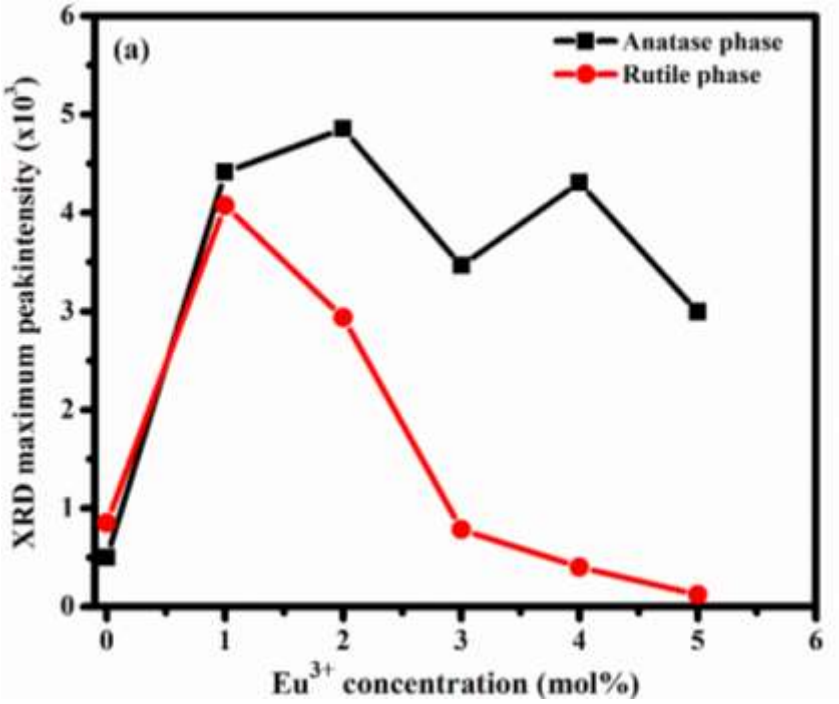

Figure 4.3 (a) Phase composition of TiO_2:Eu^{3+} nanoparticles annealed at 600℃ as a function of Eu^{3+} concentration.

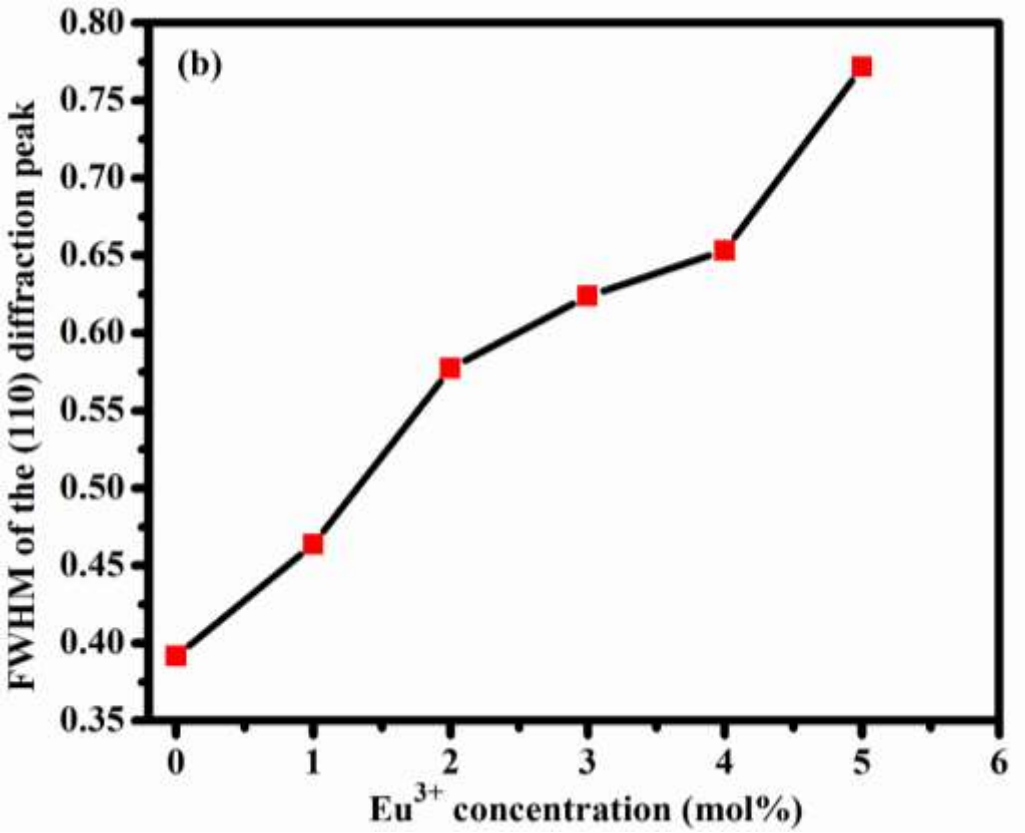

Figure 4.3 (b) Full width at half maximum (FWHM) of (110) diffraction peak as a function of Eu^{3+} concentration.

The average crystallite size (D) of prepared TiO_2: Eu^{3+}nanoparticles were estimated using Scherrer's equation [13] given by

$$D = 0.89\lambda / \beta cos\theta \quad (1)$$

where D is the average crystallite size, λ the x-ray wavelength (0.15406 nm), θ the Bragg diffraction angle and β is a full width at half maximum (FWHM) of the diffraction peak. The average crystal sizes of undoped and Eu^{3+} (5 mol %) doped TiO_2 nanoparticle using all diffraction peaks are 21 and 8 nm, respectively. The decrease in crystallites size can be explained in terms of strain induced in the system, resulting in slight change of the lattice periodicity when Eu^{3+} ions was incorporated into crystal lattice of TiO_2 [6]. From the XRD studies, X-ray diffraction peaks of crystal planes [004] at 2θ=38° and [200] at 2θ=48.22° for anatase and also [110] at 2θ=27.61° and [101] at 2θ=36.25° for rutile were used to calculate the lattice parameter of TiO_2 presented in table 1 using equation (2) [14].

$$\mathrm{Sin}^2\theta = \frac{\lambda^2}{4a^2}\left[h^2 + k^2 + \left(\frac{a}{c}\right)^2 l^2\right] \quad (2)$$

where θ is the Bragg diffraction angle, *hkl* are the Miller indices and *a* and *c* are lattice parameters. The calculated and theoretical lattice parameters of anatase and rutile TiO_2 are shown in table 4.1. However, lattice parameters of both anatase and rutile TiO_2 are bigger when compared to the theoretical lattice constants showing that prepared anatase and rutile TiO_2 have grown along *a*, *b* and *c*-axis compared to theoretical lattice constant.

Table 4.1 The lattice parameters of anatase and rutile TiO_2 phases.

Lattice parameters	Calculated		Theoretical [15]	
	Anatase (Å)	Rutile (Å)	Anatase (Å)	Rutile (Å)
a	3.549	4.563	3.784	4.594
b	3.549	4.563	3.784	4.594
c	9.460	2.946	9.515	2.958

The FT-IR spectra of TiO_2 taken at room tempearture in the range of 400 and 4000 cm^{-1} to determine the functional groups of TiO_2 nanoparticle is presented in Figure 4.4. From the spectrum, it can be observed that absorption bands around 485 and 744 cm^{-1} are typically corresponding to the stretching mode of Ti-O in the crystalline. The sharp absorption bands around 1387 cm^{-1} is associated with deformation of organic functional group (-C-H bending) respectively [16]. Another absorption peak appeared around 2356 cm^{-1} is associated with the characteristics vibration of C-H bond of the alkane group. These alkane group might probably due to one of the precursors used such as titanium (IV) butoxide [17].

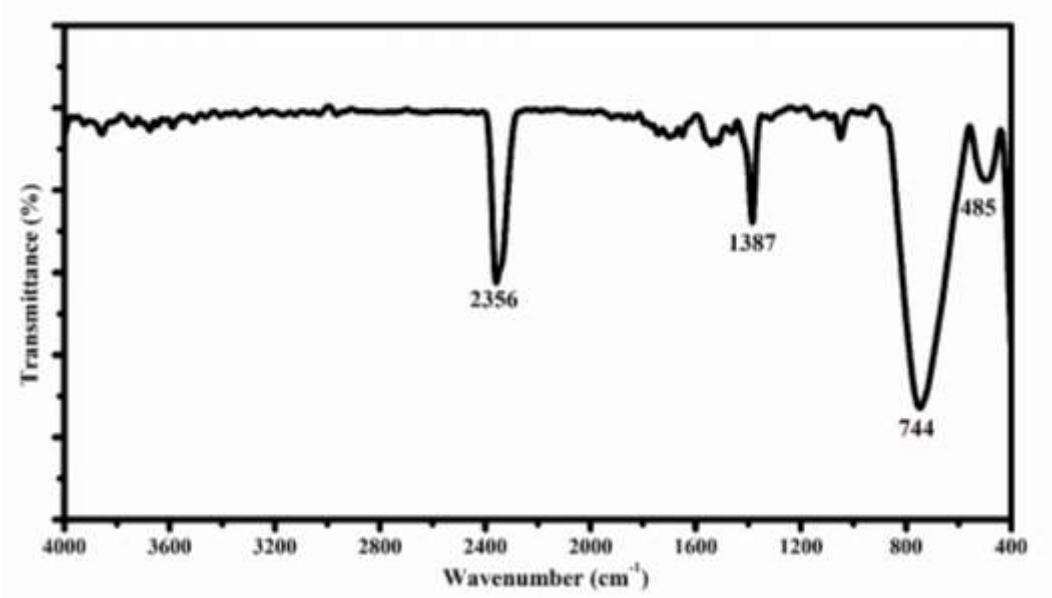

Figure 4.4 FTIR spectrum of TiO_2 nanoparticles.

Field Emission Scanning Electron Microscope (FE-SEM) micrographs of TiO_2 nanoparticle calcined at 600℃ were studied to examine particle morphology. As it follows from Figure 4.5 (a) TiO_2 grew into granular nanorods. The average length and diameter of the TiO_2 nanorods calculated from high magnification micrograph shown in Figure 4.5 (b) are approximately 410 and 73 nm, respectively. The morphology of TiO_2 did not change when Eu^{3+} ions were incorporated. Figure 4.5(b) shows high magnification micrograph and the morphology of the nanorods are thickened and irregular nanoparticlce are observed. In order to verify the presence of all elements in TiO_2:Eu^{3+} nanoparticles, they were investigated using energy dispersive x-ray spectroscopy (EDS) as shown in figure 4.5(e). The carbon peak could be from the carbon tape used to mount the sample. The elemental contents of titanium is ~58%, oxygen ~32% and europium ~10% in weight percentage respectively. Table 4.2 depicts the calculated concentration of elements present in TiO_2:Eu^{3+}. The measured Eu concentration (10w%) correspond to the doping concentration (5 mol%) used for preparing the sample. In addition, the concentration of O (83 mol%) is less than expected suggesting that the sample is oxygen deficient compared to TiO_2.

Table 4.2 Calculated concentration (mol %) of elements relative to Ti in TiO_2:Eu^{3+}.

Elements	Measured (Weight %)	Concentration (mol %) relative to Ti
Ti	58	100
O	32	83
Eu	10	5

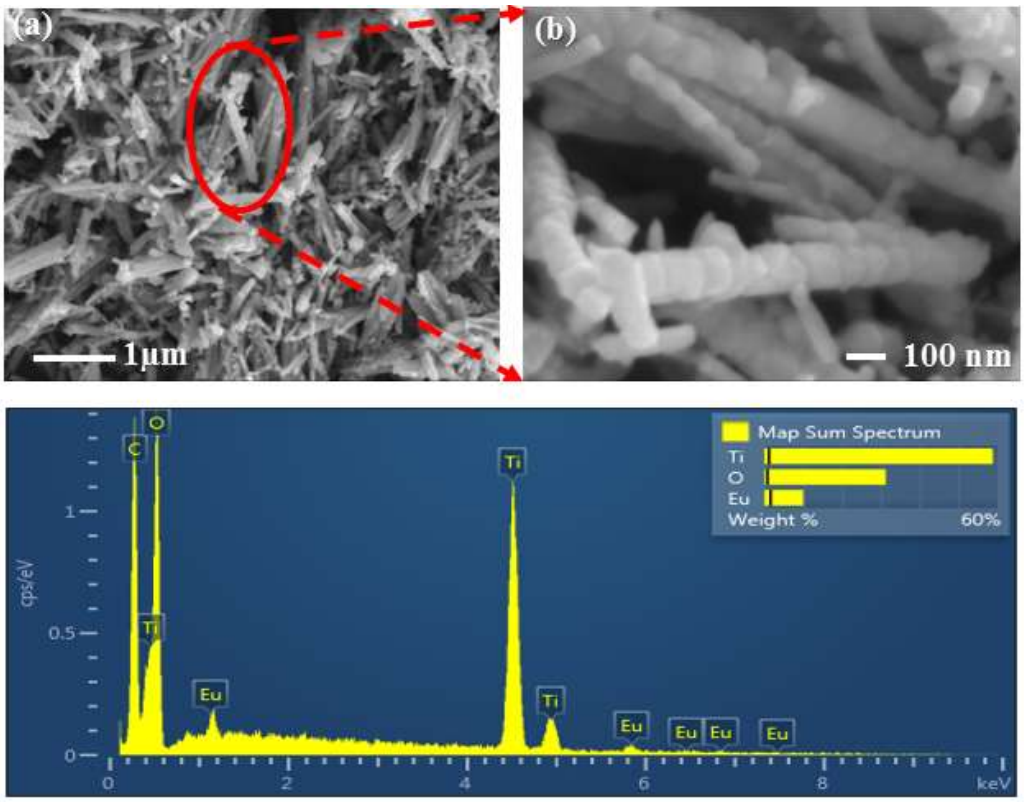

Figure 4.5 (a) - (b) FE-SEM micrographs of TiO_2 and (c) EDS analysis of 5.0 mol% Eu^{3+} doped TiO_2 nanoparticle.

4.3.2 Optical analysis

The UV-Vis reflectance spectra for undoped and Eu^{3+}-doped titania nanoparticle were recorded as shown in Fig. 4.6(a) after annealed at 600℃. A sharp decrease in reflectance at ~ 425 nm is due to strong absorption edge of TiO_2 nanoparticle [6]. Eu^{3+} doped TiO_2 shows characteristics of $f \rightarrow f$

absorption of Eu^{3+}. On increasing the concentration of Eu^{3+} ions, the absorption bands of Eu^{3+} are increased and the absorption edge suffered a gradual blue shift. The blue shift is due to a shifting of the conduction and valence band of TiO_2 because of the existence of charge-transfer transition between Eu^{3+} 4*f* electrons and conduction or valence bands of TiO_2 [18]. Observed characteristic $4f \rightarrow 4f$ absorption peaks of Eu^{3+} are assigned to $^7F_0 \rightarrow {}^5D_2$ and $^5D_1$ in the wavelength regime of 465 and 535 nm respectively [19, 20]. The band-gap energies (E_g) for undoped and Eu^{3+}-doped TiO_2 nanoparticle were determined from the extrapolation of the linear portion of the $(\alpha h\nu)^{1/2}$ vs $h\nu$ plots from Tauc's plot method [21].

$$\alpha h\nu = A\,(h\nu - Eg)^2 \qquad (2)$$

where, *A* is constant, E_g is the optical band gap, *h* is Plank's constant and α is the absorption coefficient. The optical indirect band-gap (n = 2) has increased from 2.96 to 3.15 eV with an increase in Eu^{3+} concentration. An increase in Eu^{3+} concentration shift the conduction band of TiO_2 above the highest excited state of Eu^{3+} and the energy transfer between Eu^{3+} and TiO_2 is enhanced by the interaction of Eu^{3+} electrons and conduction band [6].

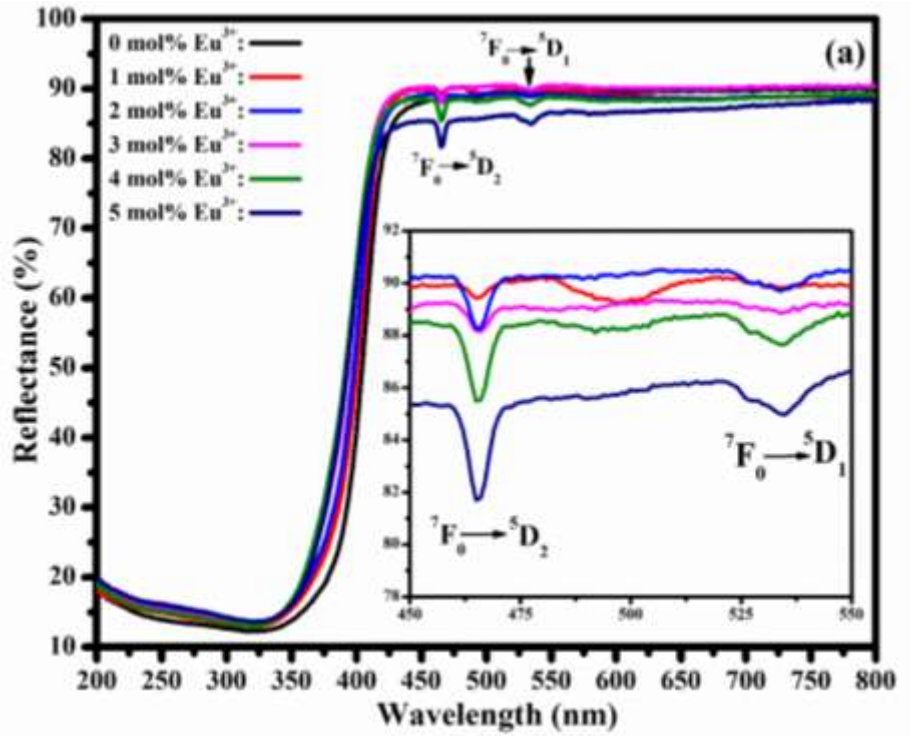

Figure 4.6 (a) The reflectance spectra for TiO_2: Eu^{3+} nanoparticle.

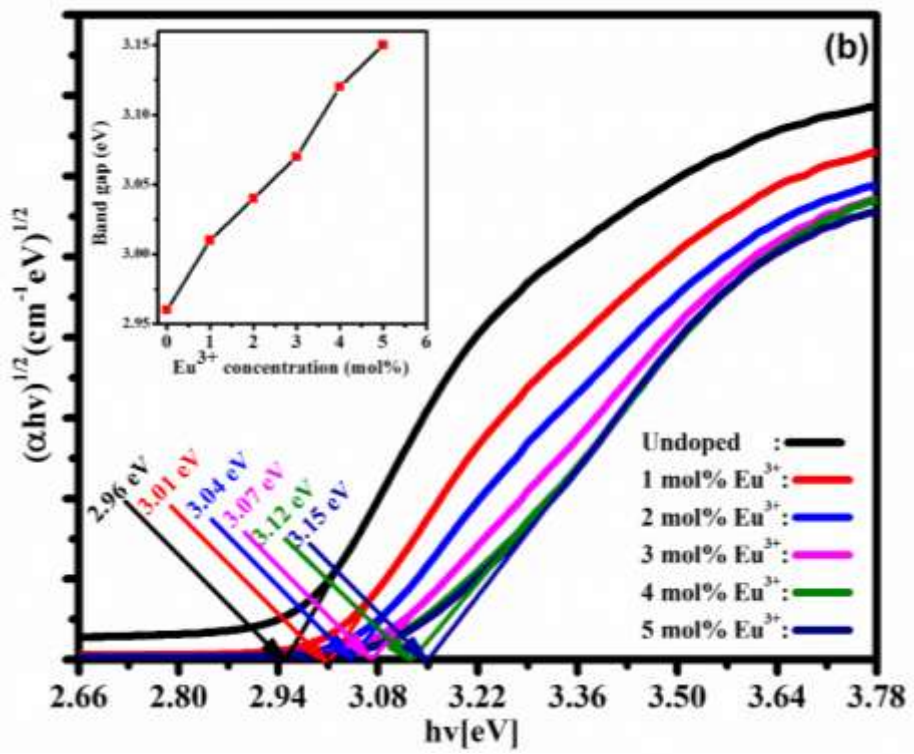

Figure 4.6 (b) Band-gap calculated with Tauc's plot for TiO_2: Eu^{3+} nanoparticle

4.3.3 Photoluminescence analysis

Figure 4.7(a) shows the emission spectra of the TiO_2 nanoparticle, which were taken under 325 nm He-Cd laser excitation. It is seen that TiO_2 nanoparticle showed a broad PL emission peaking from 350 to 800 nm after annealing at 600 ℃. Generally, the photoluminescence emission spectrum of TiO_2 is attributed to three different kinds of physical origin such as surface states, radiative recombination of self-trapped excitons and oxygen vacancies [6, 22, 23, 24]. This broad peak centred at ~460 nm might have originated from the anatase and rutile crystallite due to the lattice distortion caused by annealing and surface oxygen vacancies that are present in the sample. Gaussian fitting was used to de- convolute the TiO_2 broad emission peak in order to understand their peak positions and nature as shown in Fig. 4.7(a). Chang et al [25] prepared TiO_2 nanoparticles by sol–gel method and reported two photoluminescence sub-bands peaks at 465 nm and 525 nm attributed to F and F^+ centres respectively. The F centre represents the neutral oxygen vacancy and F^+ centre represents oxygen vacancy losing one electron. The energy level diagram of TiO_2 emissions is shown in Fig. 4.7(b).

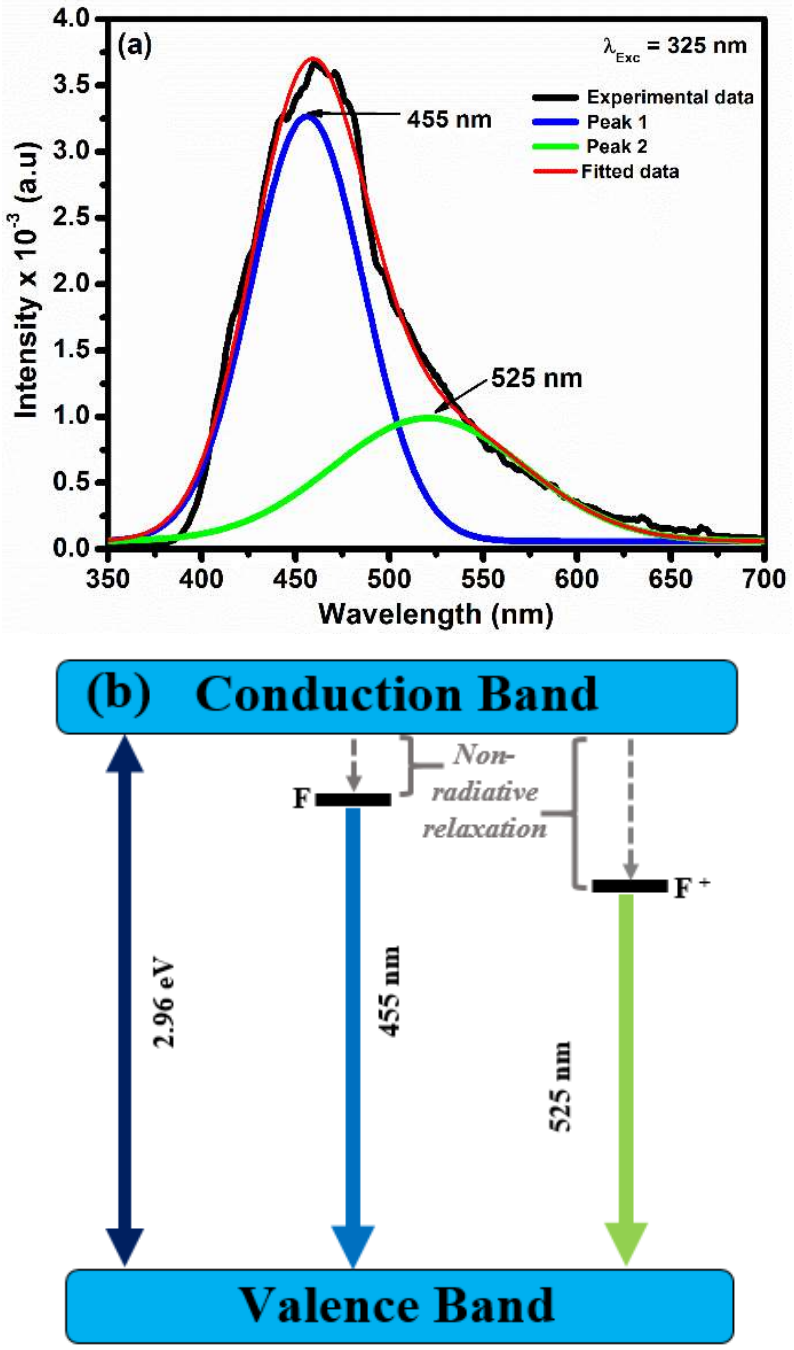

Figure 4.7 (a) PL emission of TiO_2 annealed at 600 ℃ and (b) schematic energy level diagram.

Figure 4.8 depicts the excitation and emission spectrum of TiO_2: x mol% of Eu^{3+} annealed at 600 ℃. All photoluminescence spectra of were measured using a Cary eclipse fluorescence spectrophotometer. The excitation spectrum were measured by monitoring 613 nm emission

wavelength from the highest concentration of Eu^{3+} ions. It consist of four sharp peaks lines centred at 396, 415, 466 and 535 nm that correspond to the intrinsic $4f \rightarrow 4f$ transitions: $^5F_0 \rightarrow {}^5L_6$ and $^5F_0 \rightarrow {}^5D_J$ (J = 0, 2 and 3) of Eu^{3+} ions in the host [26, 27]. From the emission spectrum, it can be seen that the emission intensity is enhanced and it is influenced by the ligands ions in the crystals [28]. The weak and intense emissions at 580 nm, 592 nm, 613 nm, 653 m and 703 nm are attributed to Eu^{3+} transitions: $^5D_0 \rightarrow {}^7F_J$ (J = 1, 2, 3 and 4) respectively [29]. According to Li et al [30], the colour emission intensity of different transitions: $^5D_0 \rightarrow {}^7F_J$ depends on the local symmetry of the crystal field of Eu^{3+} ions in the host. If the Eu^{3+} ions occupy an inversion symmetry site in the crystal field, the emission which originate from magnetic dipole transition $^5D_0 \rightarrow {}^7F_1$ around 590 nm becomes the dominant transition while electric-dipole- allowed transition $^5D_0 \rightarrow {}^7F_2$ around 613 nm becomes dominant if the Eu^{3+} ions does not occupy the inversion symmetry site. In this study, the predominant emission from TiO_2:Eu^{3+} nanoparticle is from $^5D_0 \rightarrow {}^7F_2$ (613 nm) the transition of Eu^{3+} which originate from electric-dipole- allowed transition and is hypersensitive to the environment. The energy level diagram for TiO_2: Eu^{3+} nanoparticle emissions is shown in Fig 4.9.

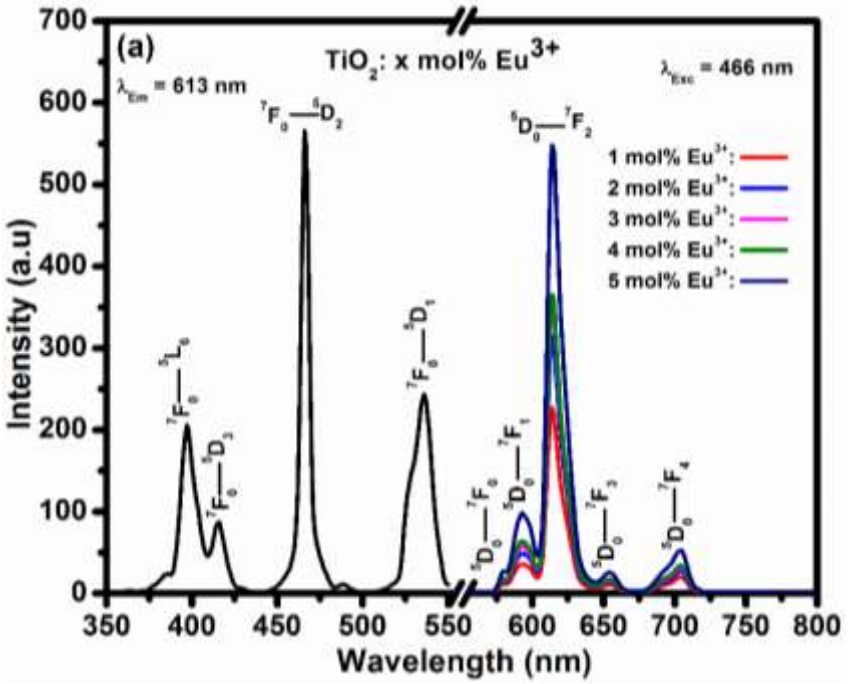

Figure 4.8 Excitation and emission spectra of TiO_2:Eu^{3+} with different concentration of Eu^{3+} ions.

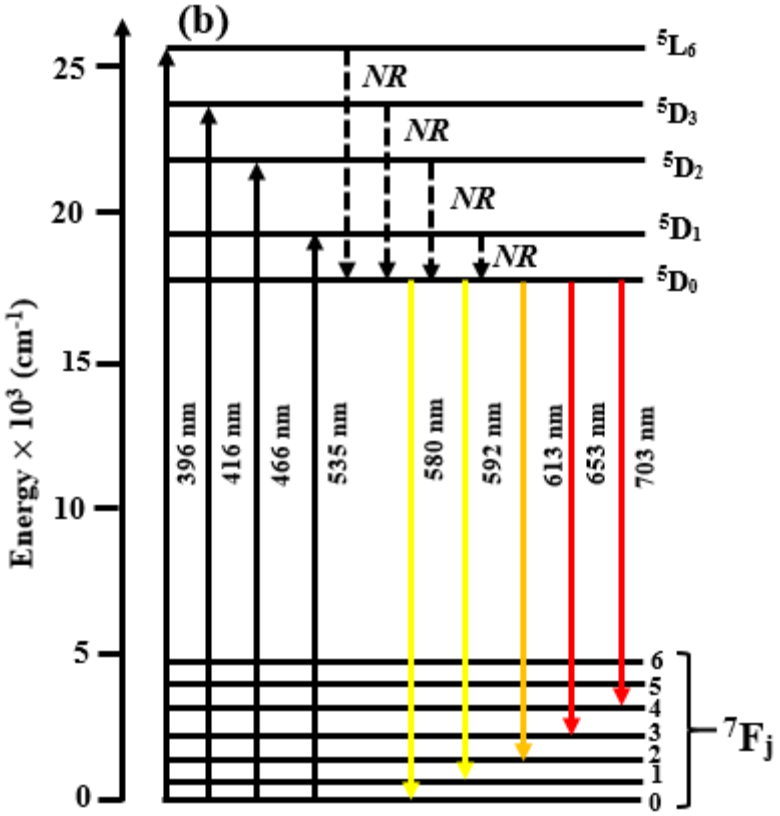

Figure 4.9 Energy level diagram for Eu^{3+} ions in TiO_2 (*NR* = non-radiative relaxation).

4.4 Conclusion

In conclusion, undoped and Eu^{3+} doped TiO_2 nanoparticle were successfully synthesized via co-precipitation method. The effect of Eu^{3+} concentration on the structure of ZnO nanoparticle was confirmed by XRD analysis and both the tetragonal anatase and rutile phases of TiO_2 was observed. FE-SEM results shows that as prepared TiO_2 grew into granular nanorods made of irregular nanoparticles. The luminescent properties of both TiO_2 and TiO_2: Eu^{3+}nanoparticle were investigated. Blue and green emissions from TiO_2 nanoparticle are attributed to the defects centres while emissions from TiO_2:Eu^{3+} are attributed to Eu^{3+} transitions.

4.5 References

[1] D.A. H. Hanaor and C.C. Sorrell. Journal of Materials Sciences, 46 **(2011)** 855–874.

[2] H.I. Hsiang and S.C. Lin. Materials Science and Engineering, 380 **(2004)** 67–72.

[3] K. Brandenburg .Crystal Impact GbR, Bonn, Germany **(2005)**.

[4] L. Liu and X. Chen. American Chemical Society, 114 **(2014)** 9890−9918.

[5] W.J. Yin, S. Chen, J.H. Yang, X.G Gong, Y. Yan and S.H Wei. Applied physics letter, 96 **(2010)** 221901.

[6] M. Pal, U. Pal, J.M.G.Y Jiménez and F.P. Rodríguez. Nanoscale Research Letters, 7 **(2012)** 1-12.

[7] J.G. Li, X. Wang, K. Watanabe, and T. Ishigaki, J. Phys. Chem. B, 110 **(2006)** 1121-1127.

[8] R.S. Ningthoujam, V. Sudarsan, R.K. Vatsa, R.M. Kadam, Jagannath, and A. Gupta. Journal of alloy and compounds, 486 (209) 864-870.

[9] E.Z. Alejandre, M.Z. Torres, M.G. Hipolito, M.A. Frutis, G.A. Flores, J.G. Mendoza and C. Falcony. Journal of Physics D, 42 **(2009)** 1-8.

[10]. J. Zhao, H. Duan, Z. Ma, L. Liu and E. Xie, Journal of optoelectronics and advanced materials, 10 **(2008)** 3029 – 3032.

[11] R.S. Ningthoujama, V. Sudarsana, R.K. Vatsaa, R.M. Kadamb, Jagannathc and A. Gupta. Journal of Alloys and Compounds, 486 **(2009)** 864–870.

[12] B. Choudhury, M. Dey and A. Choudhury. International Nano Letters, 3 **(2013)** 1-8.

[13] R.E. Kroon. Nanoscience and the Scherrer equation versus the 'Scherrer–Gottingen equation'. S Afr J Sci. 2013:109(5/6), Art. #a0019, 2 pages. http://dx.doi. org/10.1590/sajs.2013/a0019.

[14] W. Massa, Crystal Structure Determination, Springer-Verlag, Berlin, Heidel- berg, New York **(2000)** 25.

[15] M. Landmann, E. Rauls and W.G. Schmid. Journal of physics: Condensed Matter, 24 **(2012)** 195503 (6pp).

[16] M.M. Karkare. Int Nano Lett, 4 **(2014)**111.

[17] B. Keerthana, J. Madhavan and M.V.A. Raj. Scholars Research Library, 6 **(2014)** 50-55.

[18] V. Stengl, S. Bakardjieva and N. Murafa. Materials Chemistry and Physics 114 **(2009)** 217–226.

[19] L.F. Koao, F.B. Dejene, R.E. Kroon and H.C. Journal of Luminescence, 147 **(2014)** 85–89.

[20] C. Shinho. Journal of the Korean Physical Society, Vol. 66, No. 10, **(2015)** 1559 – 1563.

[21] Vinod Kumar, S. Som, Vijay Kumar, Vinay Kumar, O.M. Ntwaeaborwa, E. Coetsee and H.C. Swart. Chemical Engineering Journal, 255 **(2014)** 541–552.

[22]. S.Perumal, C.G. Sambandam, K.M. Prabu and S. Ananthakumar. International Journal of Research in Engineering and Technology, 03 **(2014)** 2321-7308.

[23]. T.S. Senthil, N. Muthukumarasamy, R. Balasundaraprabhu and C.K.S. Kumaran. Journal of NanoScience and nanotechnology, 1 **(2012)** 06-09.

[24]. S.G. Yenchalwar, V.K. Azhagana and M.V. Shelke. Royal society of Chemistry, 16 **(2014)** 17786.

[25]. Y.H. Chang, C.M. Liu, C. Chen and H.E. Cheng. Journal of the Electrochemical Society. 159 **(2012)** 401-405. [25] X. Zeng, J. Yuan, and L. Zhang, J. Phys. Chem. C, 112 **(2008)** 3503-3508

[27] B. Han, P. Li, J. Zhang, J. Zhang, Y. Xue, X. Suo, Q. Huang, Y. Feng, H. Shi. Materials Letters, 158 **(2015)** 208–210.

[28] Z. Zhang, L. Liu, S. Song, J. Zhang, D. Wang. Current Applied Physics, 15 **(2015)** 248-252.

[29] Y. Fang, H. Li, Y. Wanga and X. Liua. The Royal Society of Chemistry, 39 **(2010)** 11594–11598.

[30] Ho. Li, K. Zheng, Y. Sheng, Y. Song, H. Zhang, J. Huang, Q. Huo, H. Zou. Optics and Laser Technology, 49 (2013) 33–37.

Chapter 5 Co-precipitation preparation and luminescent properties of ZnO: Eu^{3+} nanoparticles

5.1 Introduction

ZnO is a well-known important group II-IV semiconductor with a broad energy band (3.37 eV) and a large exciton binding energy (60 meV) [1]. The wurtzite crystal of ZnO belongs to hexagonal system with lattice constants *a* and *b* that lie in the x-y plane and have equal length, and *c* parallel to z-axis as shown in Figure 5.1(a) drawn using the diamond software [2]. The values of lattice constants are $a = b = 3.429$ Å and $c = 5.207$ Å (JCPDS card # 36-1451) [3] at room temperature. The ratio *c/a* for ZnO hexagonal structure is about 1.60 and it deviate slightly from ideal value of hexagonal cell which is $c/a = \sqrt{8/3} = 1.633$. However, Zn^{2+} (cation) and O^{2-} (anion) ions in ZnO structure are bonded in the form of tetrahedral to form ZnO_4 groups, meaning that Zn^{2+} ions are surrounded by four O^{2-} ions of a regular tetrahedron with the Zn^{2+} ions at the centre as shown in Figure 5.1(b). Similarly, each O^{2-} ion is surrounded by four Zn^{2+} ions with the O^{2-} ions at the centre. Additionally, the types of wurtzite structure are covalently bonded with sp^3 hybridization. This tetrahedron in ZnO structure is imperfect because the bond length parallel to the c-axis of Zn^{2+}-O^{2-} is 1.992 Å and the length of the other three basal bonds is 1.973 Å. Therefore, the bond length along c-axis is 0.985% longer than other three basal bonds length [3-4].

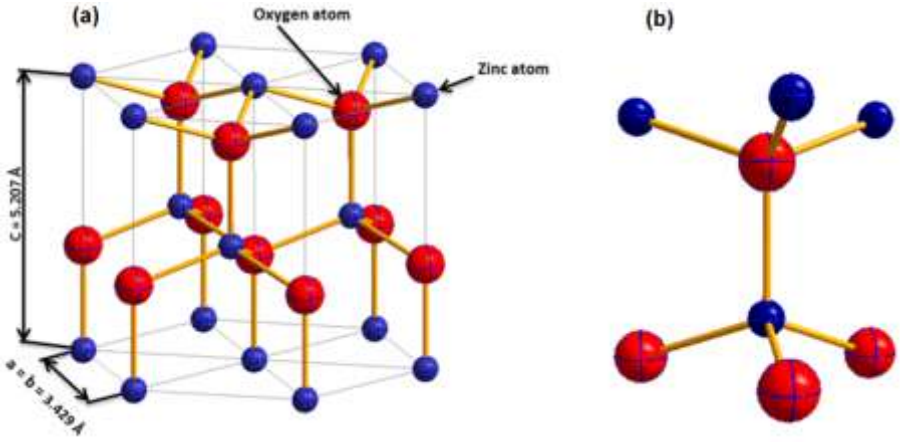

Figure 5.1 (a) Wurtzite crystal structure of ZnO and (b) Tetrahedron in ZnO structure.

ZnO semiconductor has received much attention in research because it has potential applications in different types of light-emitting devices, solar energy conversion and photocatalysis due to various properties that includes good transparency, high electron mobility, and strong room temperature luminescence [1, 5, 6]. An intrinsic physical and chemical properties of ZnO such as electronic, luminescence and magnetic properties can be easily improved by incorporating relevant impurities into ZnO interstitial through doping and co-doping [7]. Incorporation of rare earth elements are well known in tuning the properties of semiconductors and can in turn be used in applications such as emitters in the visible region due to their *f*→*f* or *f*-*d* internal orbital transition [8].

Various properties of materials at nano-scale are playing a major role in both scientific and industrial applications. Simply because ZnO has good optical properties it is being considered as one of the most semiconductor utilized in nanodimensions with possible future applications [6] in different types of electronic devices. This chapter presents undoped and Eu^{3+} doped ZnO nanoparticles that were synthesized by co-precipitation method. Their structure, morphology and optical properties were investigated. The optical (reflectance and photoluminescence transitions) properties of ZnO and ZnO:Eu^{3+} were studied in detail.

5.2 Materials and experimental procedure

ZnO:Eu^{3+} nanoparticulate phosphors were prepared from analytical grade zinc acetate dehydrate ($Zn(CH_3COO)_2{\cdot}H_2O$), sodium hydroxide pellets (NaOH) and europium nitrate pentahydrate ($Eu(NO_3)_3{\cdot}5H_2O$). In a typical preparation, zinc acetate dehydrate was dissolved in de-ionized water followed by continuous stirring for 30 minutes. Sodium hydroxide pellets were dissolved in de-ionized water by stirring 15 minutes. This solution was added drop-wise to the zinc acetate solution. The resulting solution was further stirred for one hour and a precipitate was obtained. The precipitates was centrifugally separated and washed several times with de-ionized water to remove excess Zn^{2+} and Na^{+} ions. The precipitate was dried in an oven at 60 ℃ overnight and finally ZnO nano-powder was obtained. The powder was cooled down to room temperature and ground gently using a pestle and mortar.

5.3 Results and discussion

5.3.1 Structural and morphological analysis

The XRD patterns of ZnO and ZnO:Eu^{3+} nanoparticle are shown in figure 5.2(a). All diffraction peaks of pure ZnO and Eu^{3+}-doped ZnO shows peak positions that match well the standard data JCPDS card number 36-1451 (a = b = 0.3253 nm, c = 0.509 nm) of hexagonal wurtzite structure of ZnO. As can be seen in Figure 5.2(a) and (b), there are impurity related diffraction peaks (marked with asterisk ***** and +) indicating the presence of a secondary phases of Eu_2O_3 (JCPDS, card number 34-0072) and $Zn(OH)_2$ (JCPDS, card number 74-0094). The impurities are probably due to the fact that most of Eu^{3+} ions segregated on the surface and small number of Eu^{3+} ions that were introduced into Zn interstitial sites due to difference in ionic radii of Eu^{3+} (0.95 Å) and Zn^{2+} (0.74 Å) [9].

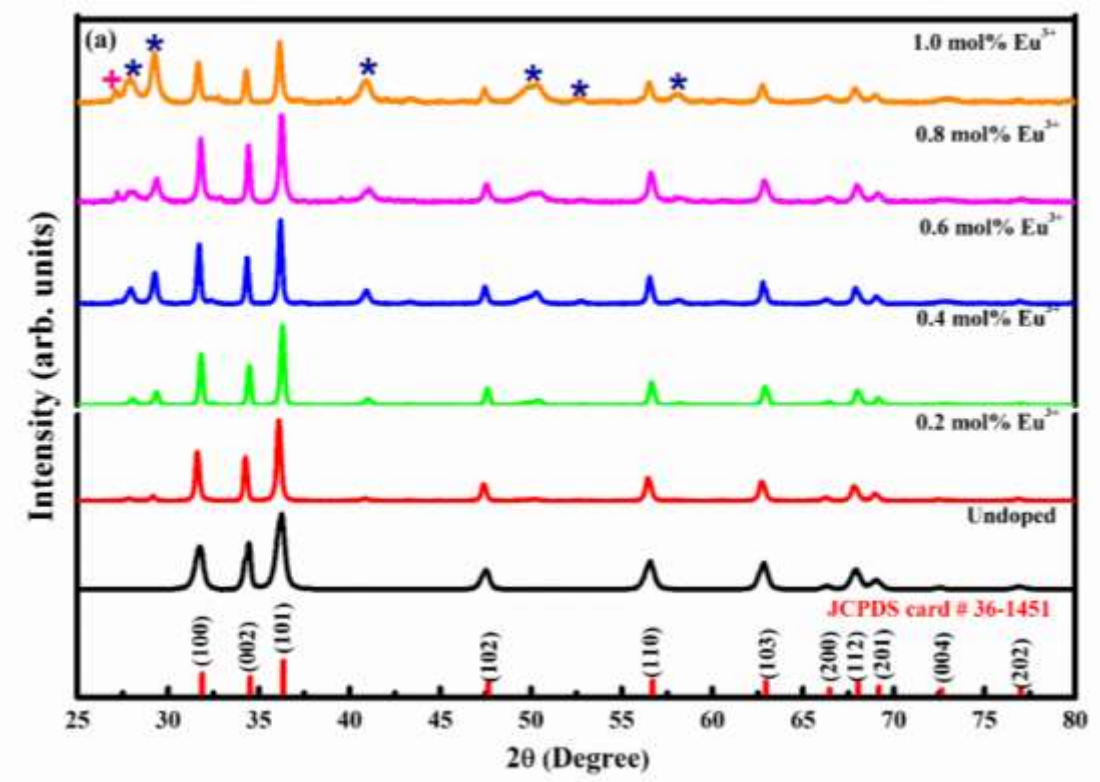

Figure 5.2 (a) XRD pattern for pure ZnO and Eu^{3+}-doped ZnO nanoparticle.

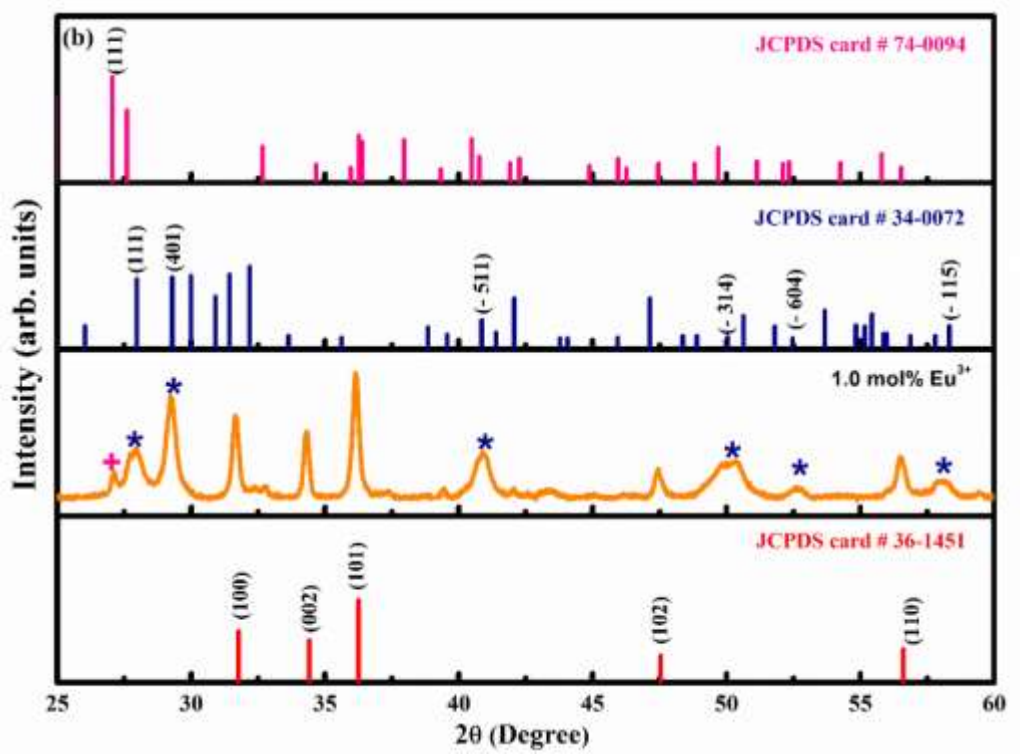

Figure 5.2(b) XRD patterns for 1.0 mol% Eu^{3+}-doped ZnO nanoparticle and standard files of $Zn(OH)_2$ and Eu_2O_3.

The average crystallite size (*D*) of ZnO nanoparticles were estimated using Scherrer's equation [10] given by

$$D = 0.89\lambda / \beta cos\theta \quad (1)$$

where *D* is the average crystallite size, λ the x-ray wavelength (0.15406 nm), θ the Bragg diffraction angle and β is a full width at half maximum (FWHM) of the diffraction peak. The diffraction peaks of ZnO get narrower with an increase of Eu^{3+} concentration suggesting that crystallinity was improving. The crystallite size values of both undoped and Eu^{3+}-doped ZnO are listed in Table 5.1. The lattice constants of ZnO nanoparticles were calculated (a = b = 0.3254 nm and c = 0.5209 nm) using (100) and (002) diffraction peaks by equation (2) and they are consistent with theoretical lattice constant values [11]

$$\mathrm{Sin}^2\theta = \frac{\lambda^2}{4a^2}\left[\frac{4}{3}(h^2 + hk + k^2) + \left(\frac{a}{c}\right)^2 l^2\right] \quad (2)$$

where θ is the Bragg diffraction angle, *hkl* are the Miller indices and *a*, *b* and *c* are lattice parameters. Equation (3) was derived from equation (2) by substituting $\sin^2\theta$ with Bragg's

equation in order to calculate d-spacing of ZnO nanoparticles. The values of *a*, *b* and *c* used in the calculations based on the lattice parameters from the synthesized ZnO nanoparticle in this study and are shown in Table 5.2. However, according to JCPDS no. 36-1451 d-spacing for ZnO are also shown in Table 5.2 and the measured d-spacing are quite reasonable compared to d-spacing from JCPDS no. 36-1451.

$$\frac{1}{d^2} = \frac{4}{3}\left(\frac{h^2 + hk + k^2}{a^2}\right) + \frac{l^2}{c^2} \qquad (3)$$

Table 5.1 The average crystallites size of undoped and Eu^{3+} doped ZnO.

Nanophosphor	Crystallites size (nm)
ZnO	15.2
ZnO: Eu^{3+} (1.0 mol %)	23.1

Table 5.2 The crystallographic planes corresponding to various Bragg angles and the calculated and theoretical d-spacing for ZnO.

2θ (deg.)	Planes	Measured d-spacing (nm)	Standard d-spacing (nm)
31.72	(100)	0.2818	0.2814
34.39	(002)	0.2604	0.2603
36.20	(101)	0.2478	0.2475
47.48	(102)	0.1912	0.1913
56.54	(110)	0.1627	0.1624
62.81	(103)	0.1478	0.1477
67.90	(200)	0.1409	0.1407
69.01	(112)	0.1379	0.1378

The FT-IR spectra of ZnO taken at room tempearture in the range of 400 and 4000 cm^{-1} is shown in Figure 5.3. The spectrum shows two absorption band around 441 and 565 cm^{-1} which correspond to the stretching mode frequencies of Zn-O. The band around 867 cm^{-1} is due to the formation of tetrahedral coordinates of Zn. The bands around 1577 and 1412 cm^{-1} may be related to the symmetric and asymmetric stratching vibrations of carboxylic group originating from the reaction intermediates or small residues of zinc acetate used for preparation of ZnO nanoparticle. The broad peak and the small around at 3428 and 2364 cm^{-1} are due to O-H group and CO_2 stretching [12,13].

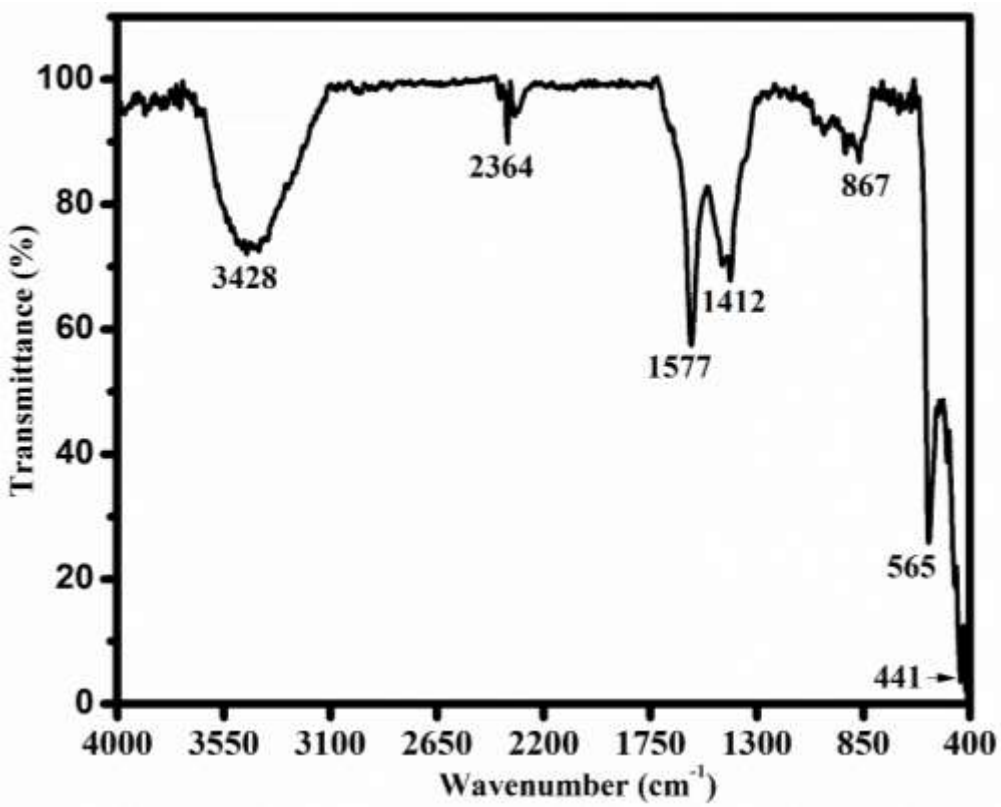

Figure 5.3 FTIR spectroscopy of ZnO nanoparticle

Figure 5.4(a) shows the FE-SEM micrographs of undoped and Eu^{3+} doped ZnO nanostructures. The morphology of undoped ZnO consists of agglomeration of flake-like nanostructures, which was shown to change to oval shape when the Eu^{3+} ions were incorporated as shown in Figure 5.4(a-c). The morphological changes of ZnO due to incorporation of Eu^{3+} ions have been reported and attributed to the complete change of the surface aspect to oval-like shapes and tensile stress occurring inherently in Eu^{3+} doped ZnO [14, 15]. Figure 5.4(c) shows high magnification micrograph confirming the oval-like nanostructures. The elemental analysis on the ZnO: Eu^{3+}

nanoparticle was investigated using energy dispersive x-ray spectroscopy (EDS) as shown in figure 5.4(d). The inset in the spectrum shows the chosen position on FE-SEM where EDS analysis was performed. The EDS results confirms the presence of zinc (Zn), europium (Eu), oxygen (O) and carbon (C) in ZnO:Eu $^{3+}$ nanoparticles. The carbon might due to carbon tape used to mount the samples on the stub.

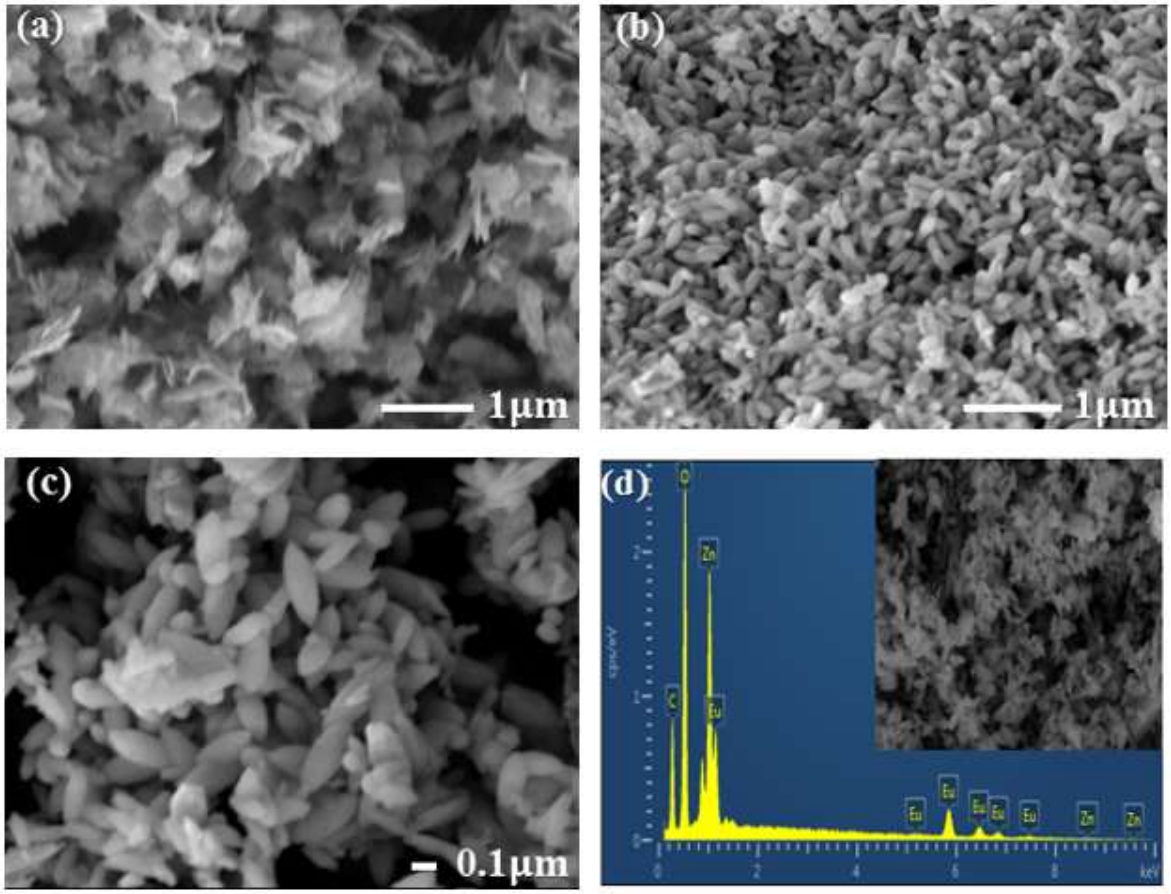

Figure 5.4 FE-SEM micrographs (a) un-doped ZnO, (b-c) 1.0 mol% Eu^{3+} doped ZnO and (d) EDX analysis of 1.0 mol% Eu^{3+} doped ZnO nanoparticle.

5.3.2 Optical analysis

The UV-Vis reflectance spectra for ZnO and ZnO:Eu^{3+} nanoparticles are presented in Figure 5.5(a). The spectra of ZnO nanoparticle shows high reflectance in the visible and high absorption

in the ultraviolet (UV) region while ZnO:Eu^{3+} nanoparticles shows $f \rightarrow f$ absorption in the visible region in addition to ultraviolet (UV) absorption of ZnO in the UV. Similarly, the samples exhibit a sharp decrease in reflectance at approximately 375 nm. The decrease in reflectance is called absorption edge and it is attributed to absorption of the electrons of level $1S_h$ (fundamental state) to $1S_e$ (excitation state) excitonic transition in ZnO nanoparticles. The characteristic $4f \rightarrow 4f$ absorption peaks of Eu^{3+} are assigned to $^7F_0 \rightarrow {}^5D_2$, $^5D_1$, $^5D_1$, and $^5D_0$ in the wavelength regime of 465, 525,535 and 592 nm respectively [14, 15]. The inset in the spectra is the enlarged spectra confirming $4f \rightarrow 4f$ transition of Eu^{3+} ions. A close inspection of this spectrum reveals further extra absorption peak (marked with black square) around 496 nm for ZnO:Eu^{3+} (0.2 and 1.0 mol%) samples that could be due to incidental impurities in the samples. The band-gap energies (E_g) for undoped and Eu^{3+}-doped ZnO nanoparticle were estimated from the extrapolation of the linear portion of the $(\alpha h\nu)^2$ vs $h\nu$ plots (Figure 5.5(b)) from Tauc's plot method [14]

$$\alpha h\nu = A\,(h\nu - Eg)^{1/2} \qquad (2)$$

where, A is constant, E_g is the optical band gap, h is Plank's constant and α is the absorption coefficient. The optical band-gap of the ZnO (host) is estimated to be 3.27 eV. When Eu^{3+} ions is incorporated in ZnO, the bandgap energy decreases because of the presence of defects states due to Eu^{3+} doping and the behaviour of the band gap as a function of Eu^{3+} concentration is shown as inset in figure 5.5(b). Narrowing of the bandgap of ZnO with doping is a well-known phenomenon due to the impurities that introduce new energy levels in the band gap near conduction edge such as shallow level donor impurities. Additionally, the impurities such as shallow acceptor impurities introduce energy levels near the valence band [8]. So, the new impurities formed between the conduction and valence bands with an increase in Eu^{3+} concentration in ZnO tailors its band gap.

5.3.3 Photoluminescence analysis

The photoluminescent spectra of undoped ZnO and effect of the Eu^{3+} concentration on the emission behavior of ZnO:Eu^{3+} nanoparticles are shown in Figure 5.6 and 5.7. The emission spectrum of undoped ZnO was excited at 325 nm using He-Cd laser and is shown in Fig. 5.6. The PL excitation and emission spectra (for excitation 466 nm using xenon lamp) of ZnO:Eu^{3+} nanoparticles were measured with the Cary-Eclipse fluorescence spectrophotometer and are shown in Fig 5.7. The PL spectra of ZnO exhibit two luminescence bands: ultraviolet emission as shown in the inset insert which is located near the absorption edge due to exciton emission and visible

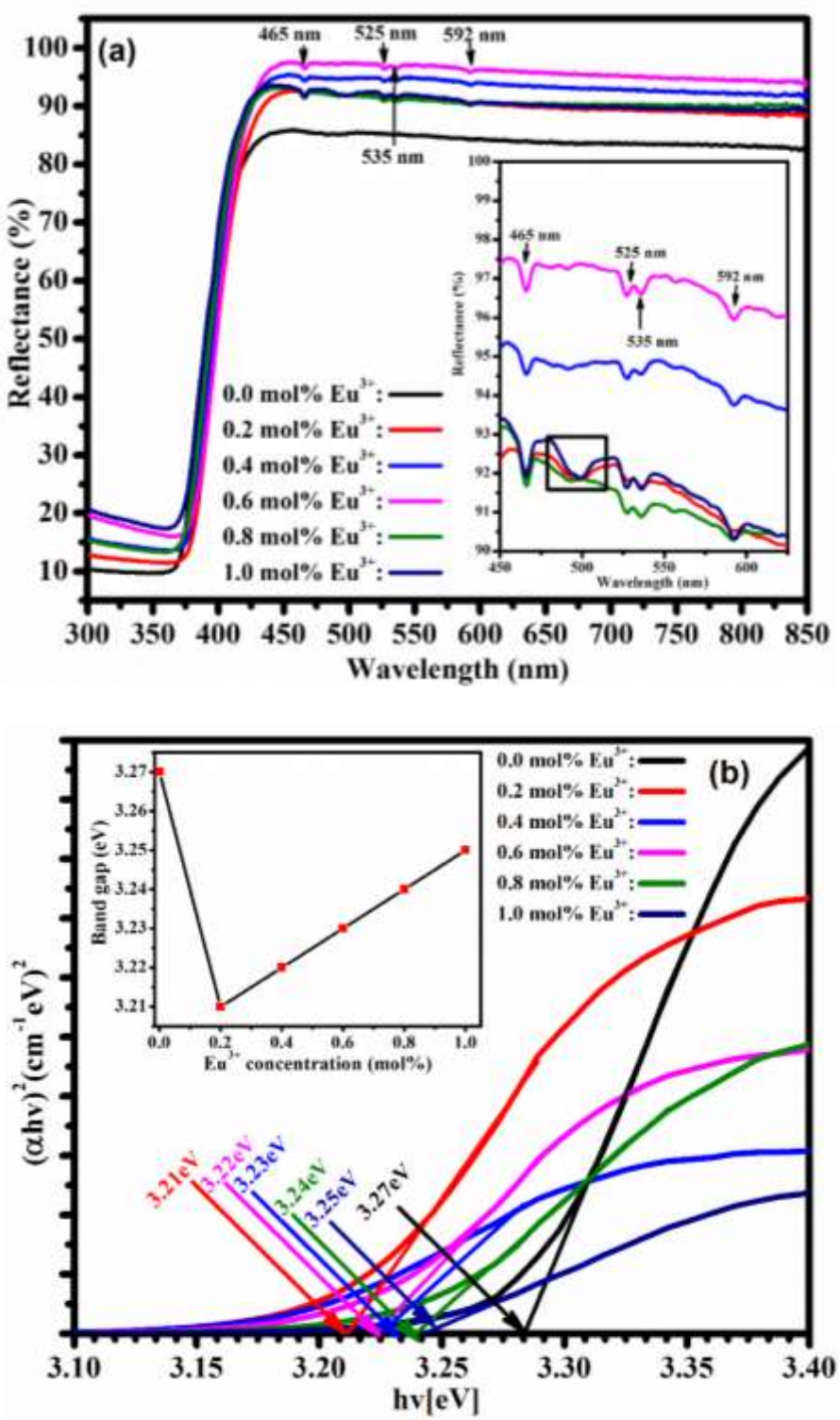

Figure 5.5 (a) Reflectance spectra and (b) Tauc's plot of un-doped and Eu^{3+} doped ZnO nanoparticles.

emission which is related to deep level emission (DLE) [8, 16]. The weak ultraviolet emission in these case may be due to the used excitation energy that may be lower than the band gap energy of the prepared ZnO or due to increased defects density in visible emission [17]. Gong et al [18], has reported that deep level emission of ZnO is normally related to green, yellow and blue luminescence. The de-convolution of the ZnO emission is shown in Figure 5.6 and the three defect-related visible emission (537, 591 and 670 nm) were observed. The three visible emission are related to oxygen vacancies (V_0) and oxygen interstitials (O_i) defects levels respectively [19].

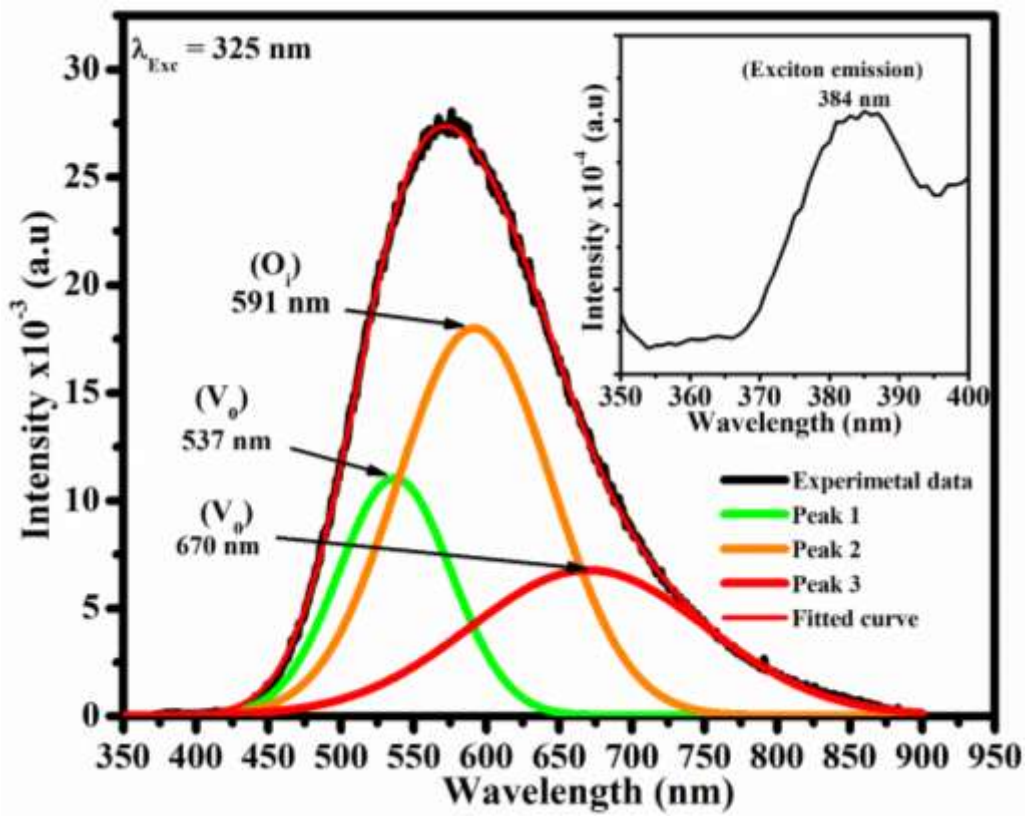

Figure 5.6 A deconvolution of the light emission of ZnO nanoparticles prepared with co-precipitation method. The inset of the figure shows the ultraviolet emission spectra of ZnO nanoparticles.

The excitation and emission spectra of Eu^{3+} doped ZnO at room temperature are shown in Fig. 5.7 (a). The excitation spectra were measured by monitoring the emission wavelength at 618 nm and the spectra contains sharp lines at 398, 416, 466 and 538 nm that correspond to the intrinsic $4f \rightarrow 4f$

transitions of Eu^{3+} in the host. Intrinsic $4f \rightarrow 4f$ transitions of Eu^{3+} observed are assigned to $^7F_0 \rightarrow {}^5L_6$, $^5D_3$, $^5D_2$ and $^5D_1$. Figure 5.7(a) shows the emission spectra for ZnO:Eu^{3+} with different concentration of Eu^{3+} ions. The weak and intense emissions at 593 nm, 618 nm, 646 m and 682-696 nm are attributed to Eu^{3+} transitions: $^5D_0 \rightarrow {}^7F_J$ (J = 1, 2, 3 and 4) respectively [20, 21]. It has been reported that the $^5D_0 \rightarrow {}^7F_1$ emission transition which is assigned to magnetic dipole becomes intense if Eu^{3+} ions are located at site with inversion symmetry, whereas $^5D_0 \rightarrow {}^7F_2$ emission transition that is assigned to electric dipole become intense without inversion symmetry in the ZnO host lattice. As can be seen in figure 5.7 that the emission intensity of transition $^5D_0 \rightarrow {}^7F_2$ is intense than that of $^5D_0 \rightarrow {}^7F_1$, which indicate that the Eu^{3+} ions occupies site without inversion symmetry in the host lattice [22]. An increase in Eu^{3+} concentration enhanced the luminescence intensity and the maximum PL intensity was observed at 0.4 mol% Eu^{3+} beyond which the luminescence intensity decreases due to concentration quenching effects. The concentration quenching is probably due to non-radiative interaction between ions as resonance energy transfer is enhanced when the doping concentration is increased [14].

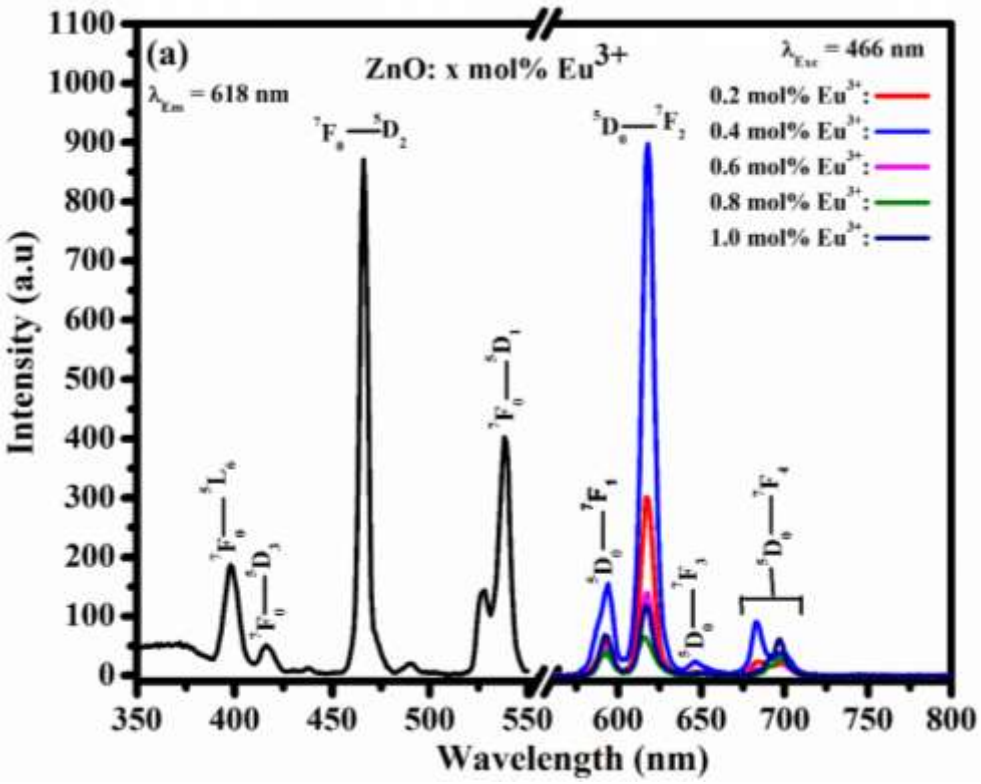

Figure 5.7 (a) PL excitaion and emission spectra of ZnO:Eu^{3+} with differeny concentration of Eu^{3+}.

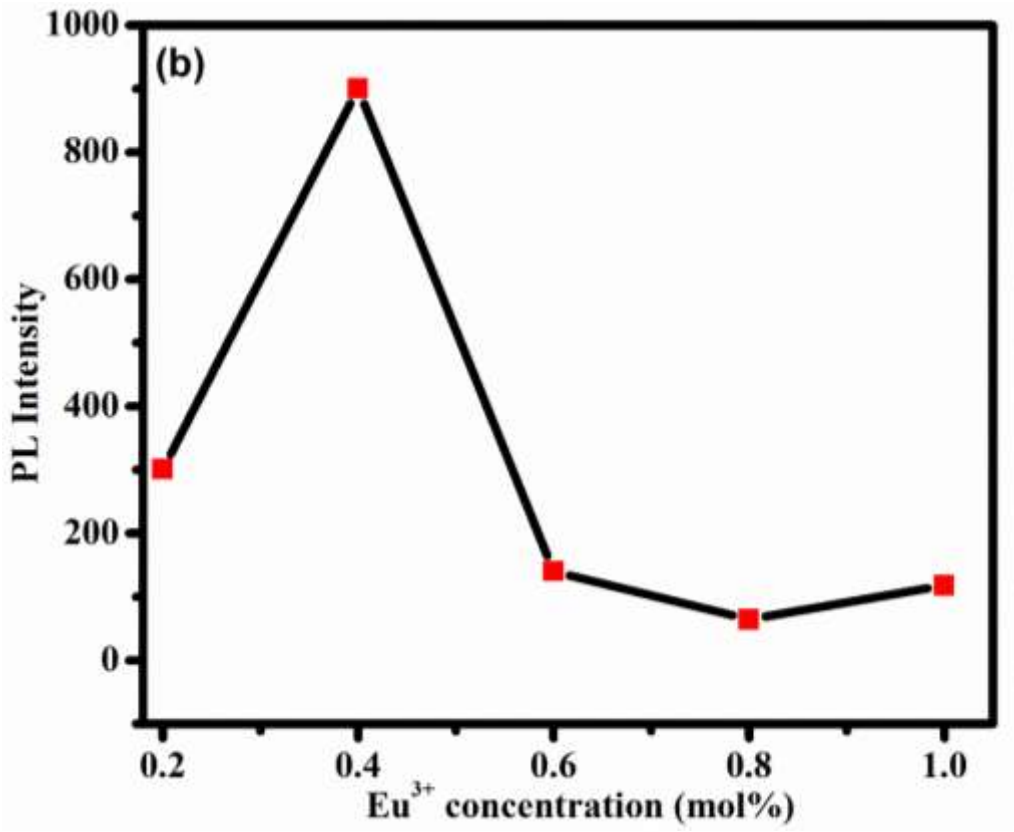

Figure 5.7 (b) PL intensity as a function of Eu^{3+} concentartion.

Figure 5.8 shows the schematic band diagram of deep-level emissions and the presence of different types of defects in ZnO nanoparticles. The ultraviolet emission is attributed to the transition from conduction band to the valence band of ZnO [8]. The visible emission is caused by the recombination of a shallowly trapped electron with a deeply trapped hole in a V_0^{++} centre. The green and red emissions at 537 and 670 nm can be ascribed to the transitions due to intrinsic defects (V_0) in ZnO nanopartcicles. The green emission originated from near conduction band to deep acceptor level while red emission originated from conduction band to deep acceptor level like V_0. Intrinsic defects is also responsible for red-orange emission and it is attributed to the transition from the conduction band to the deep levels like O_i [17] as shown in figure 5.7. ZnO:Eu^{3+} nanoparticle excited at 466 nm shows the transitions of Eu^{3+} ions.

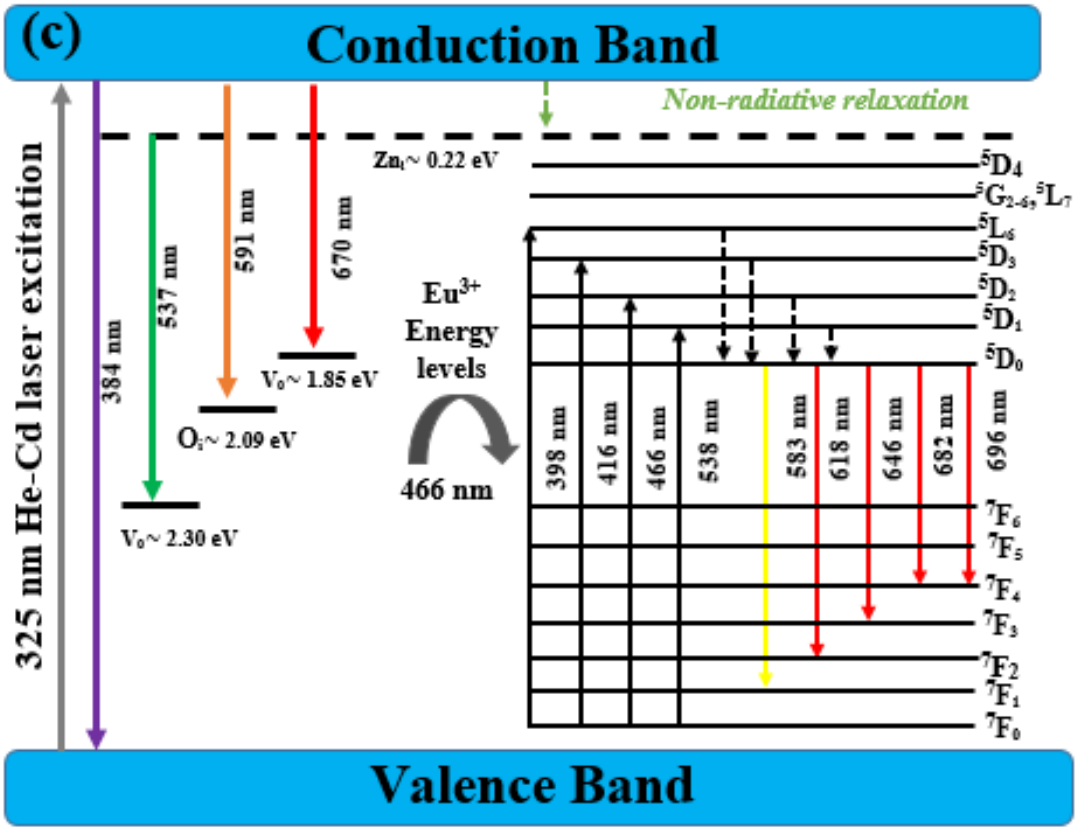

Figure 5.8 Schematic view of the energy band diagram proposed for undoped and Eu^{3+} doped ZnO nanoparticles.

5.4 Conclusion

In conclusion, undoped and Eu^{3+} doped ZnO nanoparticulate phosphors were successfully synthesized via co-precipitation method. The wurtzite hexagonal crystal structure of ZnO was observed and incorporation of Eu^{3+} in ZnO have a great influence on both structure and luminescent intensity of ZnO:Eu^{3+} nanoparticles phosphors. The broad emission spectra observed in the visible region for undoped ZnO is attributed to different kind of defects. ZnO:Eu^{3+} nanoparticle shows yellow and red emission and are attributed to Eu^{3+} transitions. The red emission intensity was measured as a function of Eu^{3+} doping concentration and the emission of Eu^{3+} are completely quenched beyond the concentration of 0.4 mol%.

5.5 References

[1] F. Lu, W. Cai, and Y. Zhang. Advanced Functional Materials, 18 (2008) 1047–1056.

[2] K. Brandenburg .Crystal Impact GbR, Bonn, Germany **(2005)**.

[3] Y. Zhang, M.K. Ram, E.K. Stefanakos, and D.Y Goswami. Journal of Nanomaterilas, 2012 **(2012)** 1-22.

[4] A. Onodera and M Takesada. In: Advances Ferroelectrics (A.P. Barranco, editor), Hokkaido University, Sapporo, Japan, **(2012)** 231-253.

[5] Fang L, Cai W and Zhang Y. Advance functional materials, 18 **(2008)** 1047-1056.

[6] S. Sabir, M. Arshad, and S.K. Chaudhari. The Scientific World Journal, **(2014)** 1-8.

[7] N. Naseri, M. Yousefi, O. Moradlou and A.Z. Moshfegh. Phys. Chem. Chem. Phys., 13 **(2011)** 4239–4242.

[8] Vinod Kumar, S. Som, Vijay Kumar, Vinay Kumar, O.M. Ntwaeaborwa, E. Coetsee and H.C. Swart. Chemical Engineering Journal, 255 **(2014)** 541–552.

[9] T.B. Iveti´c, M.R. Dimitrievska, I.O. G´uth, L.R. Da - ˇcanin, S.R. Luki´c-Petrovi´c. Journal of Research in Physics, 36(1) **(2012)** 43 - 51.

[10] R.E. Kroon. Nanoscience and the Scherrer equation versus the 'Scherrer–Gottingen equation'. S Afr J Sci. 2013:109(5/6), Art. #a0019, 2 pages. http://dx.doi. org/10.1590/sajs.2013/a0019.

[11] W. Massa, Crystal Structure Determination, Springer-Verlag, Berlin, Heidel- berg, New York **(2000)** 25.

[12] O. Yayapao,T. Thongtem, A. Phuruangrat and S. Thongtem. Journal of alloys and compounds, 276 **(2013)** 72-79.

[13] K. Ravichandrika, P. Kiranmayi and R.V.S.S.N. Ravikumar International Journal of Pharmacy and Pharmaceutical Sciences, 4(4) **(2012)** 1- 3.

[14] L.F. Koao, F.B. Dejene, R.E. Kroon and H.C. Journal of Luminescence, 147 **(2014)** 85–89.

[15] C. Shinho. Journal of the Korean Physical Society, 66(10) **(2015)** 1559 – 1563.

[16] M. Zhong, G. Shan, Y. Li, G. Wang and Y. Liu. Materials Chemistry and Physics, 106 **(2007)** 305–309.

[17] T.K. Kundu, N. Karak, P. Barik and S. Saha. International Journal of Soft Computing and Engineering, 1 **(2011)** 19-24.

[18] Y. Gong, T Andelman and G.F. Neumark. Nanoscale Res Lett, 2**(2007)** 297-302.

[19] C. Ahn, Y.Y. Kim, D.C. Kim, S.K. Mohanta, H.K. Cho. J. Appl. Phys. 105 **(2009)** 2-6.

[20] X. Zeng, J. Yuan, and L. Zhang, J. Phys. Chem. C, 112 **(2008)** 3503-3508.

[21] B. Han, P. Li, J. Zhang, J. Zhang, Y. Xue, X. Suo, Q. Huang, Y. Feng, H. Shi. Materials Letters, 158 **(2015)** 208–210.

[22] M. Chndrasekhar, H.Nagabhushana, Y.SVidya, K.S Anantharaju, S.CSharma, H.B. Premkumar, S.C. Prashantha, B.D. Prashantha, B.D. Prasad, C.Shivakumara, R. Saraf and H.P. Nagaswapura. Journal of Molecular Catalyst A, 409 **(2015)** 26-41.

Chapter 6 Sol-gel preparation and luminescent properties of ZnO-TiO_2: Eu^{3+} nanocomposites

6.1 Introduction

Metal oxide based nanocomposites have attracted a great deal attention because of their potential application to solve environmental problems. Among various metal oxide, composites of ZnO and TiO_2 are among those that have received considerable interest. These metal oxide tend to combine to form composite easily because the bulk band gap energy of ZnO (approximately 3.37 eV) is similar to that of TiO_2 (approximately 3.2 eV) [1]. However, they have different properties that are advantageous for different applications. For example ZnO have higher conductivity compared to TiO_2 while TiO_2 have higher chemical stability and reactivity, much higher dielectric constant and fewer defects states while ZnO can be easily nanostructured. Doping of ZnO and TiO_2 with rare earth materials gives the opportunity to tune luminescent properties of each oxide in a controlled manner and can be used to enhance the performance of the solar cells. The light which they emit at shorter wavelength (in the UV region) can be absorbed by the rare earths ions and re-emitted at longer wavelengths (in the visible region) [2, 3].

Rare-earths doped metal oxide phosphors are extensively used in fluorescent lamps and emissive displays. Among the rare-earth ions, trivalent europium (Eu^{3+}) ion is a widely recognized red light emitting (around 610-620 nm) dopant which is used in various red light emitting devices. The red emission is due to $4f \rightarrow 4f$ transition ($^5D_0 \rightarrow {}^7F_2$) of Eu^{3+} [4]. In this chapter, sol-gel method was used to prepare undoped as well as Eu^{3+} doped ZnO-TiO_2 nanocomposites with different concentrations of Eu^{3+}, and the structure, particle morphology and optical properties are reported.

6.2 Materials and experimental procedure

Undoped and Eu^{3+} doped ZnO-TiO_2 nanocomposites were prepared from analytical grade zinc acetate dehydrate ($Zn(CH_3COO)_2 \cdot H_2O$), monoethanolamine (C_2H_7NO), titanium (IV) butoxide ($C_{16}H_{40}O_4Ti$), nitric acid (HNO_3), lithium hydroxide (LiOH) and europium acetate dehydrate ($Eu(CH_3COO)_3 \cdot 2H_2O$)). In a typical preparation of nanocomposites, titanium (IV)-butoxide was dissolved in ethanol and the solution was stirred for 30 minutes to form what we refer to as solution 1. Nitric acid (70%) was added drop-wise in the solution as a catalyst followed by vigorous stirring for 2 hours. For the preparation of what we refer to as solution 2, zinc acetate dehydrate was dissolved in a mixture of ethanol and monoethanolamine at 60℃. The solution was stirred for 20 minutes. After one day of aging, the two solutions were combined followed by addition europium acetate dehydrate with vigorous stirring for 2 hours. The molar ratio of Ti: Zn was 1:1. Lithium hydroxide was added into a transparent solution followed by vigorous stirring at 80℃ for 1 hour and a gel was formed. The gel was dried in an oven at 90°C for 24 hours. The resulting Eu^{3+} - doped nanocomposite powders were annealed at 600°C for 2 hours.

6.3 Results and Discussion

6.3.1 Structural and morphological analysis

The crystalline phase of the undoped and Eu^{3+} doped ZnO-TiO_2 nanocomposites phosphor annealed at 600℃, identified by X-ray diffraction analysis, are represented in Figure 6.1. Distinct diffraction peaks of wurtzite ZnO and tetragonal TiO_2 (anatase and rutile phase) in the spectrum are indexed using the JCPDS file numbers 36-1451 for wurtzite ZnO, 86-1157 and 75-1753 for tetragonal TiO_2 (anatase and rutile phase). The XRD revealed that the reaction occurred between zinc oxide and titanium dioxide resulting in the formation of zinc titanium oxides, namely $ZnTiO_3$ and Zn_2TiO_4 that are consistent with the JCPDS file numbers 26-1500 and 86-0158 respectively. The broad and intense diffraction peaks from the hexagonal wurtzite ZnO indicate the high crystalline in the nanocomposites. This might be the fact that TiO_2 is amorphous to be detected by X-rays in consideration of the TiO_2 content in the ZnO-TiO_2 nanocomposites because of the

quantity could affect this factor. From the XRD pattern, it can be confirmed that the TiO_2 in nanocomposites before doping was identified as rutile phase with single peak and the diffraction peak related to anatase phase was observed due to Eu^{3+} doping. This is the indication that some of Eu^{3+} ions incorporated into the nanocomposites might be dispersed in TiO_2 matrix and stabilized anatase phase [5]. As can be seen from Fig 6.1(b), the diffraction peaks of the nanocomposites shifted slightly towards higher angle then towards lower angle with an increase in Eu^{3+} concentration. When the Eu^{3+} ions incorporated in the ZnO-TiO_2 nanocomposites crystals, the distinct difference ion radii between substitution and lattice atoms results in lattice distortion and induced strain thereby shifting the diffraction peaks. In addition, the shifting of the diffraction peaks could be due to the decrease and increase in lattice constants of present phases in the nanocomposites compared to standard JCPDS no. 36-1451 (ZnO), 86-1157 and 75-1753 for tetragonal TiO_2 (anatase and rutile phase), 26-1500 and 86-0158 for $ZnTiO_3$ and Zn_2TiO_4 respectively [4]. The average crystallite size (D) of the ZnO-TiO_2:Eu^{3+}nanocomposites were estimated using Scherrer's equation [6] given by

$$D = \frac{0.89\lambda}{\beta\cos\theta} \quad (1)$$

where D is the average crystallite size, λ the x-ray wavelength (0.15406 nm), θ the Bragg diffraction angle and β is a full width at half maximum (FWHM) of the diffraction peak. The average crystallite sizes from all diffraction peak was found to be 13 nm and increased to 20 nm with incorporation of different concentrations of Eu^{3+} ions.

The morphology of the undoped and Eu^{3+} (0.5 mol %) doped ZnO-TiO_2 nanocomposites was studied using the FE-SEM as shown in figure 6.2. From the FE-SEM micrographs, it was found that the morphology of undoped and Eu^{3+} doped ZnO–TiO_2 nanocomposites looks the same which shows that Eu^{3+} doping did not influence the morphology of ZnO–TiO_2 nanocomposites. The micrographs from Fig. 6.2 (a)-(b) have a uniform structure of irregular shaped with some spherical and highly agglomerated grains of ZnO–TiO_2 nanocomposites. The elemental analysis on the Eu^{3+} doped ZnO–TiO_2 nanocomposites was investigated using energy dispersive x-ray spectroscopy (EDS) as shown in figure 6.2(c). The EDS results confirms the presence of zinc (Zn), titanium (Ti), europium (Eu) and oxygen (O) in Eu^{3+} doped ZnO–TiO_2 nanocomposites.

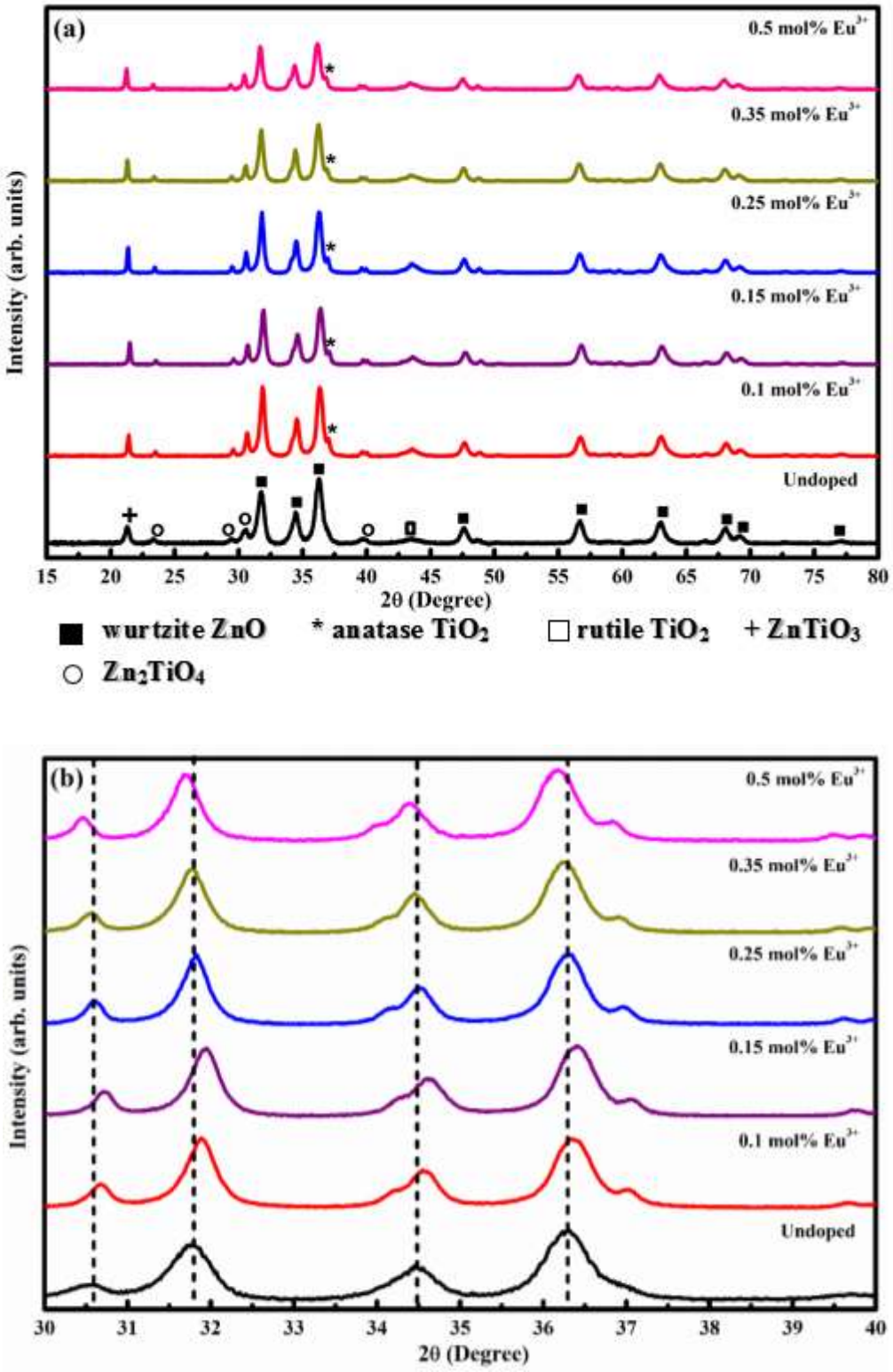

Figure 6.1(a) and (b) X-ray diffraction pattern of different concentration of Eu^{3+} ions doped ZnO–TiO_2 nanocomposites.

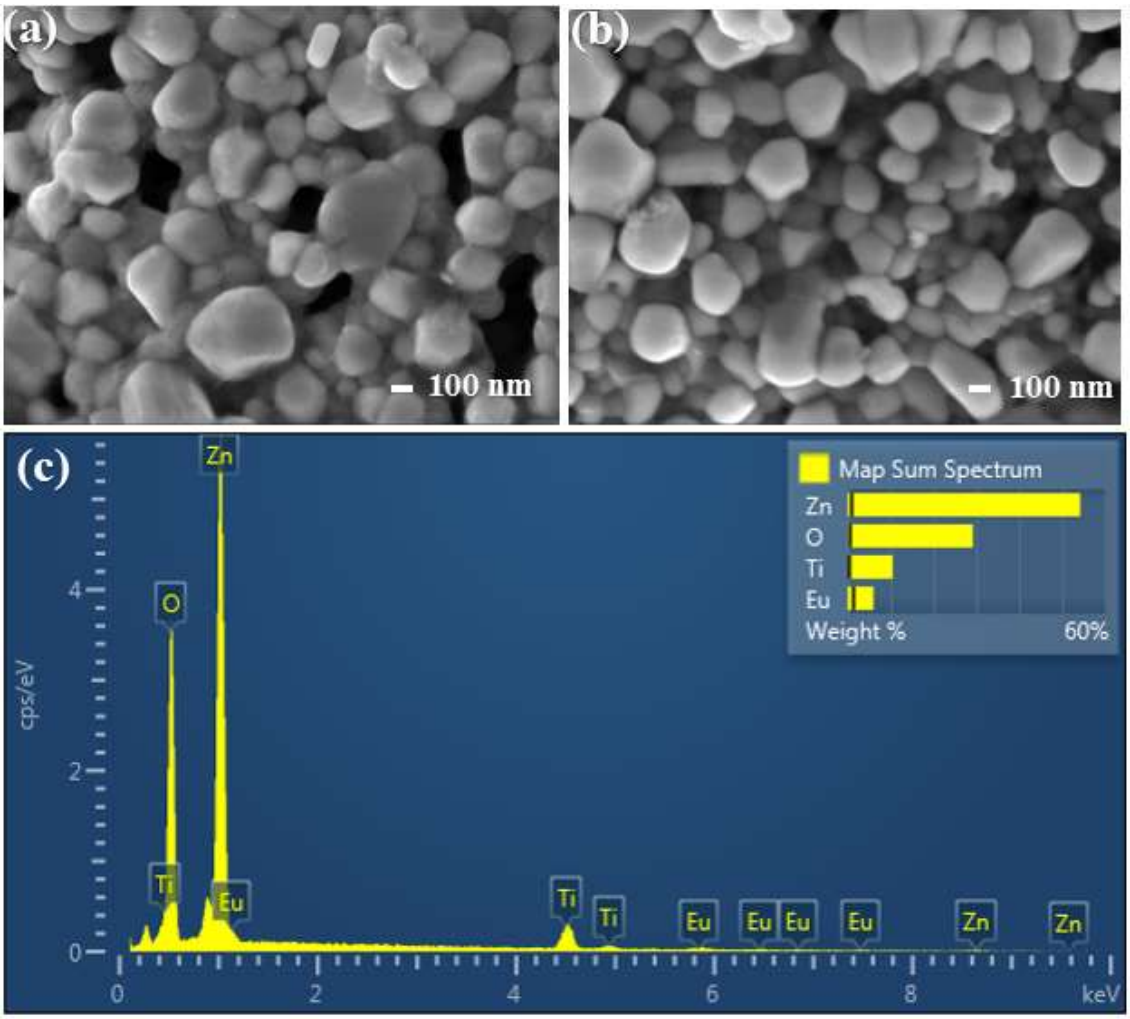

Figure 6. 2 FE-SEM micrographs (a) undoped ZnO–TiO_2 nanocomposites, (b) 0.5 mol% Eu^{3+} doped ZnO–TiO_2 nanocomposites and (c) EDS analysis of 0.5 mol% Eu^{3+} doped ZnO–TiO_2 nanocomposites.

6.3.2 Fourier transform infrared (FTIR) analysis

FT-IR measurements were performed in the range of 400– 4000 cm^{-1} to examine the stretching frequency modes as shown in Fig. 6.3. The absorption bands appearing around 527 cm^{-1} and 864 cm^{-1} are due to the stretching modes of Zn-O and Zn-O-Ti, respectively. The absorption band around 1081 cm^{-1} is ascribed to carboxylic acid (i.e. C=O stretching mode). The broad absorption bands around 1436 cm^{-1} which is typically corresponding to the vibration mode of Ti-O and Ti-O-C in the nanocomposites [7-9]. The absorption peak obsrved around 2356 cm^{-1} is associated with the characteristics vibration of C-H bond of the alkane group. This alkane group might probably

be due to one of the precursors used in the synthesis such as titanium (IV) butoxide [10]. The weak absorption band observed around 2970 cm^{-1} is associated with the C-H stretching vibration in atmospheric organic compounds [9]. The wide weak peak around 3333 cm^{-1} observed is attributed to the O-H stretching vibration of hydroxyl group on the surface and the O-H group [8] may results from the large amount of ethanol used in the preparation of the nanocomposites.

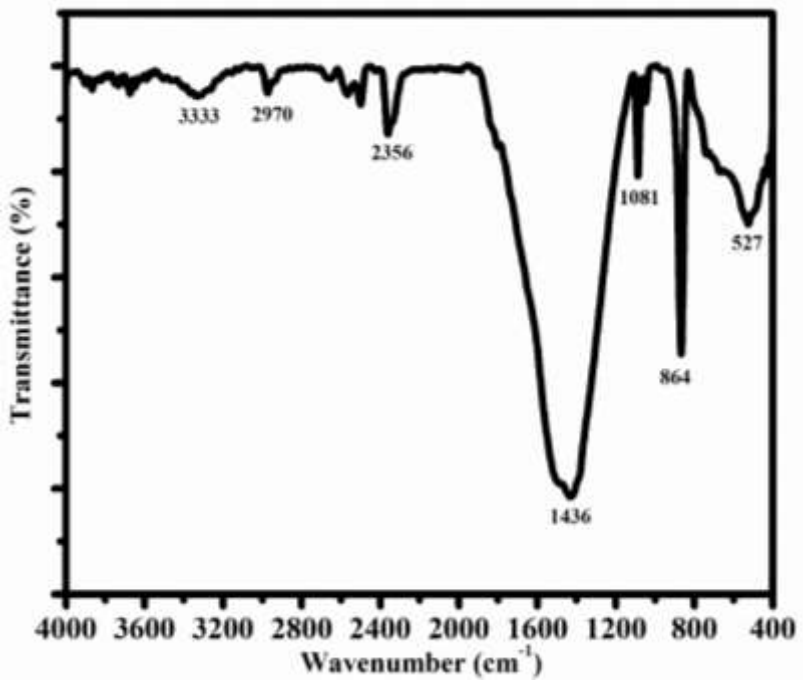

Figure 6.3 FTIR spectra of ZnO-TiO_2 nanocomposites.

6.3.3 UV-Vis Reflectance analysis

The reflectance spectra of undoped and Eu^{3+} doped ZnO-TiO_2 nanocomposites with different concentration of Eu^{3+} were recorded in the range 300 nm to 900 nm at room temperature as shown in Fig. 6.4 (a). Both undoped and Eu^{3+} doped ZnO-TiO_2 nanocomposites samples exhibit a sharp decrease in reflectance at ~ 375 nm due to strong absorption edge of ZnO. The absorption edge in these case can be explained in terms of the movement of electrons from the valence band to the conduction band in ZnO in the nanocomposites [11]. After doping the nanocomposites, characteristics $f \rightarrow f$ absorption peaks of Eu^{3+} were observed in the visible region in the wavelength regime of 465 nm and 534 nm. These $f \rightarrow f$ absorption peaks can be assigned to $^7F_0 \rightarrow {}^5D_2$ and $^5D_1$

respectively [12,13]. The insert shows the magnification of the *f→f* absorption peaks of Eu^{3+} ions. The band gap energies was estimated with Tauc's plot method shown in equation (1) using reflectance spectra.

$$\alpha h\nu = A\,(h\nu - Eg)^{1/2} \quad (1)$$

where, *A* is constant, E_g is the optical band gap, *h* is Plank's constant and α is the absorption coefficient. The plot of this parameters were used to determine the band gap energies by extrapolating the linear portion to zero at the corresponding photon energy. It is problematic that we have nanocomposites of a direct and indirect allowed transition and therefore it is unclear which one we should use for measuring band gap. However, since XRD pattern shows more dominant ZnO peaks we have decided to the value of "n" to be indirect allowed transition (n = 1/2). From the plot of band gap as a function of Eu^{3+} concentration, see the inset in Figure 6.4(b), it can be seen that doping the nanocomposites with 0.1 mol% of Eu^{3+} does not affect the band gap. An increase in Eu^{3+} concentration in ZnO-TiO_2:Eu^{3+} nanocomposites lead to the fluctuation in band gap energy. This might be caused by numerous surface state in ZnO-TiO_2:Eu^{3+} nanocomposites due to the defect state, anion or cations vacancies and interstitials (V_o/O_i) with energy levels located within the band gap where they do not have any fixed position in the energy level diagram, yet, are located within the band gap region [14].

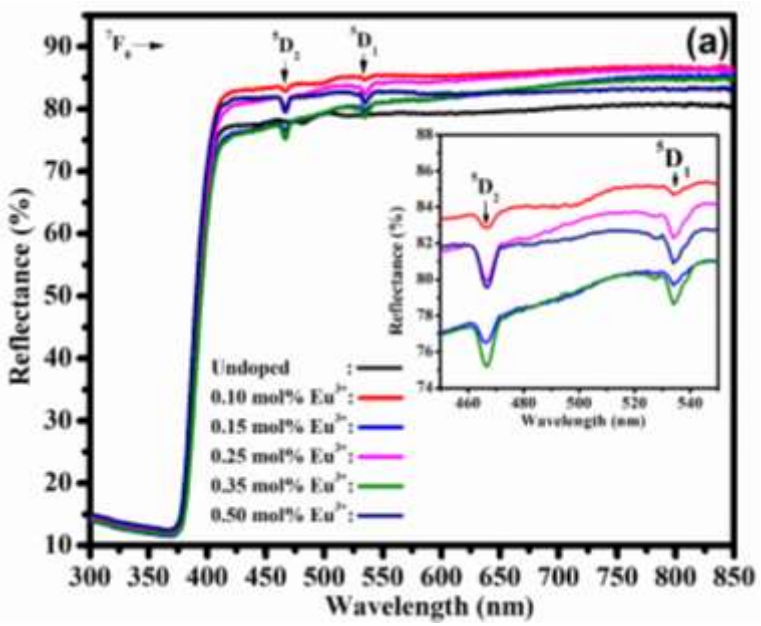

Figure 6.4 (a) Reflectance spectra of undoped and Eu^{3+} doped ZnO-TiO_2 nanocomposites for different concentration of Eu^{3+}.

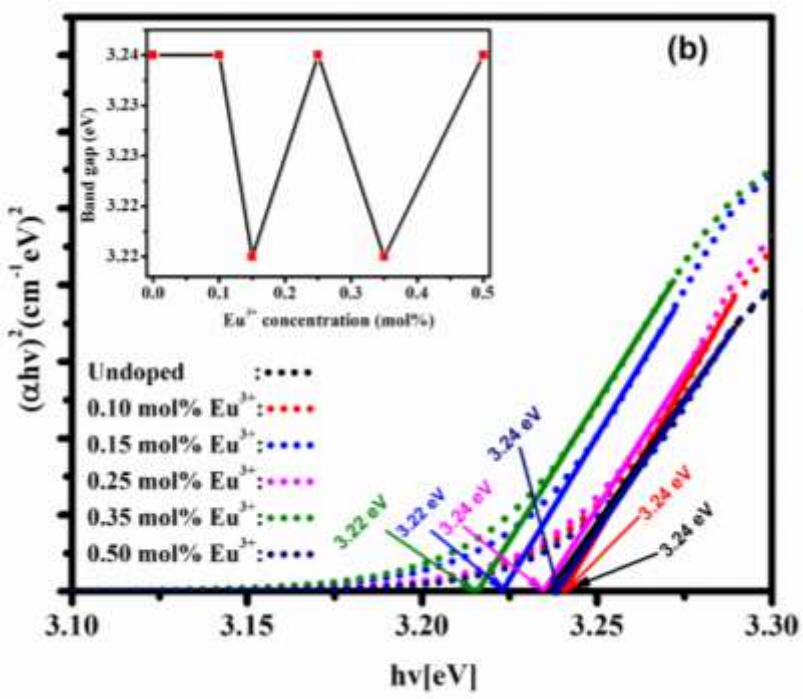

Figure 6.4 (b) Tauc's plot and band-gaps of undoped and Eu^{3+} doped ZnO-TiO_2 nanocomposites for different concentration of Eu^{3+}.

6.3.4 Photoluminescence analysis

The photoluminescence emission spectra of the ZnO–TiO_2 nanocomposites which were recorded under 325 nm He-Cd laser excitation is shown Figure 6.5. ZnO–TiO_2 nanocomposites exhibited a broad band ranging from 400 nm to 900 nm and represent the combined emission band of both hexagonal wurtzite ZnO and tetragonal TiO_2 phases as shown in Fig. 6.5(a). The broad visible emission can be related to the defects emission in ZnO and TiO_2 phases [15, 16]. Gaussian fitting was used to de-convolute this broad emission peak in order to understand their peak positions and nature as shown in Fig. 6.5(b). The blue and green emissions centred at 476 nm and 546 nm are attributed to both phases of ZnO–TiO_2 nanocomposites. The blue emission can be related to electronic transition from donor energy level of zinc interstitial to acceptor energy level of zinc vacancies [17] or self-trapped excitons localized on TiO_6 octahedra [5]. Intrinsic defects centres from ZnO such as zinc vacancy (V_{zn}), oxygen vacancies (V_o) or antisite oxygen (O_{zn}) as well as F^+ centres (oxygen vacancy losing one electron) from TiO_2 phases are responsible for green emission in the prepared ZnO–TiO_2 nanocomposites [18,19]. The orange and red emission peaking at 600 and 638 nm can be ascribed to oxygen interstitials (O_i) [20].

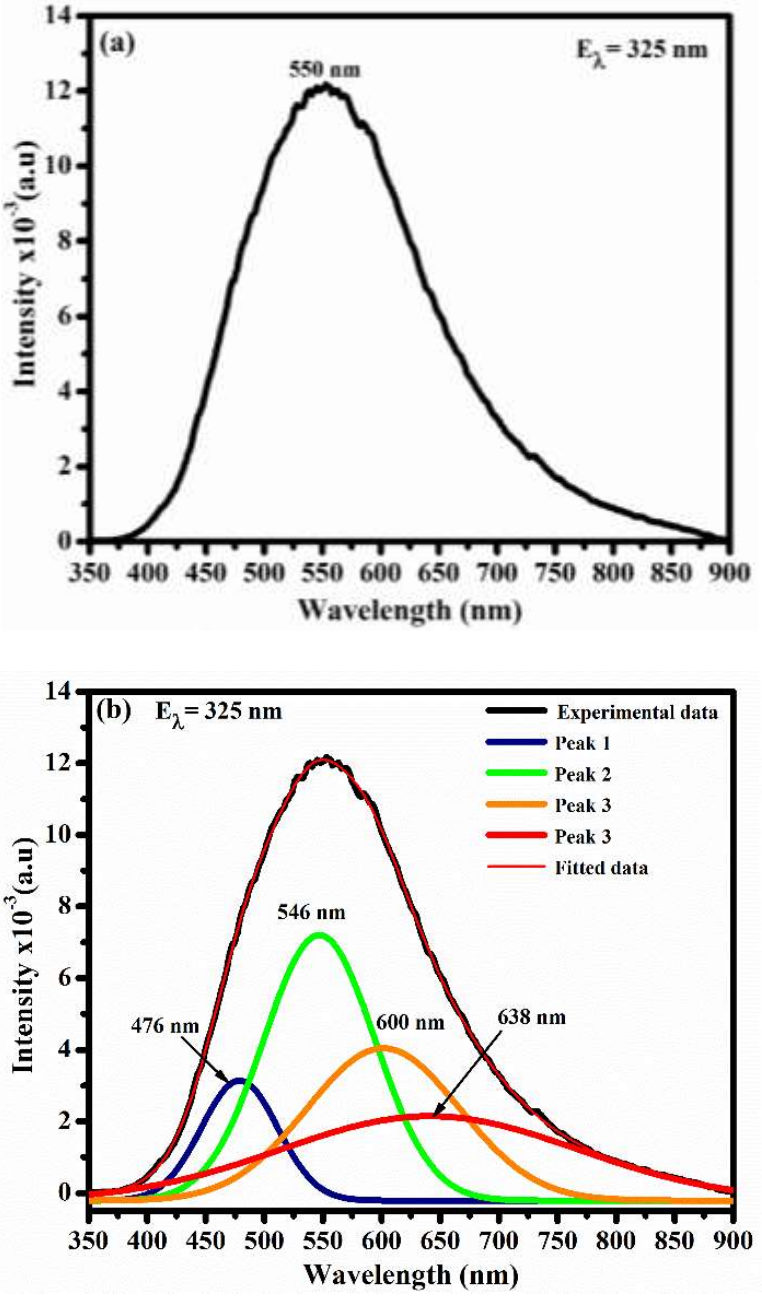

Figure 6.5 (a) PL emission of ZnO–TiO_2 nanocomposites annealed at 600 ℃ and (b) Gaussian fit of the PL emission of the nanocomposites.

The photoluminescence emission spectra of Eu^{3+} doped ZnO–TiO_2 nanocomposites prepared by sol-gel method are shown in figure 6.6 for various Eu^{3+} concentrations. The excitation spectrum were measured by monitoring 613 nm emission wavelength from the concentration of Eu^{3+} ions (0.25 mol%) that give highest luminescence intensity from emission spectrum. The excitation spectrum exhibit a series of sharp characteristics lines of Eu^{3+} centred at 396, 412, 466 and 536

nm that correspond to the intrinsic 4*f*→4*f* transitions of Eu^{3+} ions in the host and can be assigned to transitions between $^5F_0 \rightarrow {}^5L_6$ and $^5F_0 \rightarrow {}^5D_J$ (J = 1, 2 and 3) [21,22]. The emission spectrum exhibited commonly occurring five emissions peaks centred at 579, 592, 613, 652 and 707 nm. These emission are attributed to the Eu^{3+} transitions: $^5D_0 \rightarrow {}^7F_J$ where J = 0, 1, 2, 3 and 4 respectively. The dominant emission of Eu^{3+} at 613 nm is from the $^5D_0 \rightarrow {}^7F_J$ (J = 2) transitions. This emission can be explained in terms of the direct excitation (466 nm) of one Eu^{3+} ion and subsequently transfer of primary excitation energy to another Eu^{3+} ions (613 nm) [23]. As shown in Fig. 6.7, the luminescence intensity of the emission spectrum was enhanced when the Eu^{3+} concentration increased and the concentration quenching effect was observed. Migration of excitation between emissions of Eu^{3+} ions and the closely related crystal structure of zinc oxide and titanium dioxide are responsible for the concentration quenching. Additionally, concentration quenching is explained in terms of the two interactions (multipole-multipole and super-exchange interactions) that occur between Eu^{3+} ions. The critical concentration in this case was observed at 0.25 mol% of Eu^{3+} and it is due to cross-relaxation whereby energy is being transferred form one ion to another neighbor ion by transition that match in energy [24, 25].

The energy level diagram of Eu^{3+} ions and ZnO–TiO_2 nanocomposites is shown in figure 6.8. The deep-level emissions of different types of defects associated with ZnO and TiO_2 are also presented. The visible emission of the nanocomposites can be explained in terms of the recombination of a shallowly trapped electrons with a deeply trapped hole in a V_o^{++} centre in ZnO or surface oxygen vacancies in TiO_2, respectively. As can be seen from figure 6.6, green and red emission at 546 and 638 nm can be attributed to intrinsic defects such as ionized oxygen vacancy (V_o) from ZnO or the green on the other hand can be attributed to defect such as F^+ centre (oxygen vacancy losing one electron) from TiO_2 [26,27]. Recombination between the zinc interstitials (Zn_i) and the valence band from zinc [28] or F centres (neutral oxygen vacancy) from TiO_2 are responsible for blue emission at 476 nm, respectively[27]. The orange-red emission at 600 nm coming from intrnsic defects can be assigned to the transition from the conduction band to the deep levels such as oxygen interstitials (O_i) from ZnO in the nanocomposites [26]. The energy level diagram for Eu^{3+} ions doped ZnO-TiO_2 nanocomposites shows that excitaion wavelength of 466 nm raises Eu^{3+} ion from $^7F_0$ state to different higher states ($^5L_6$ and ^5D_J (J = 1, 2 and 3)) which can relaxes to $^5D_0$ state by emitting non-radiative energy and therefore finally decay radiatively to ^7F_J states where J = 0, 1, 2, 3 and 4.

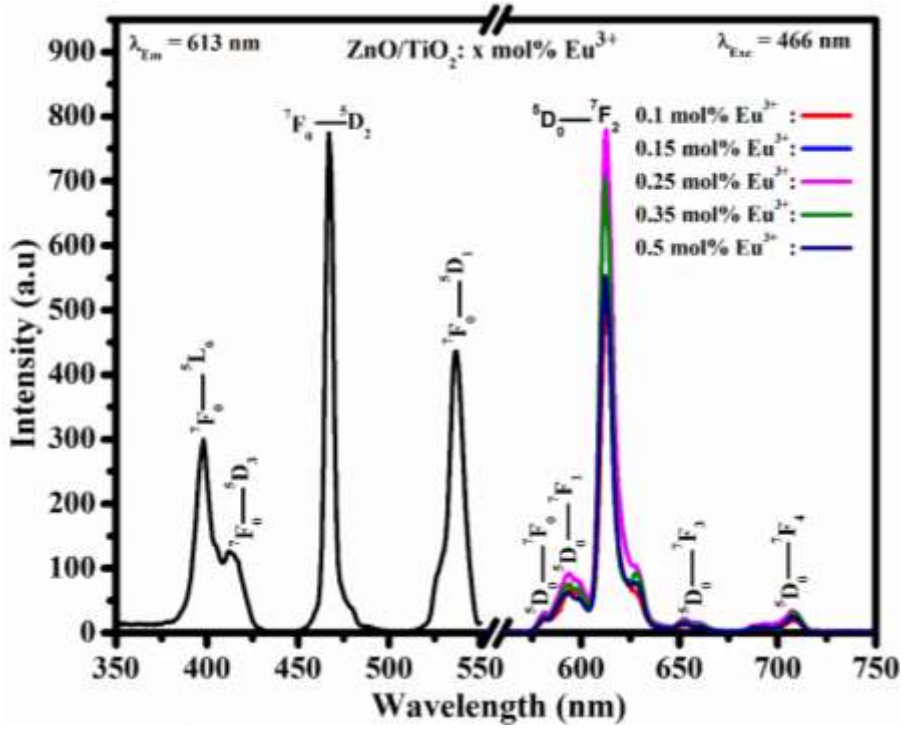

Figure 6.6 PL emission spectra of ZnO–TiO_2: Eu^{3+} nanocomposites for different concentration of Eu^{3+} ions doping for 466 nm excitation.

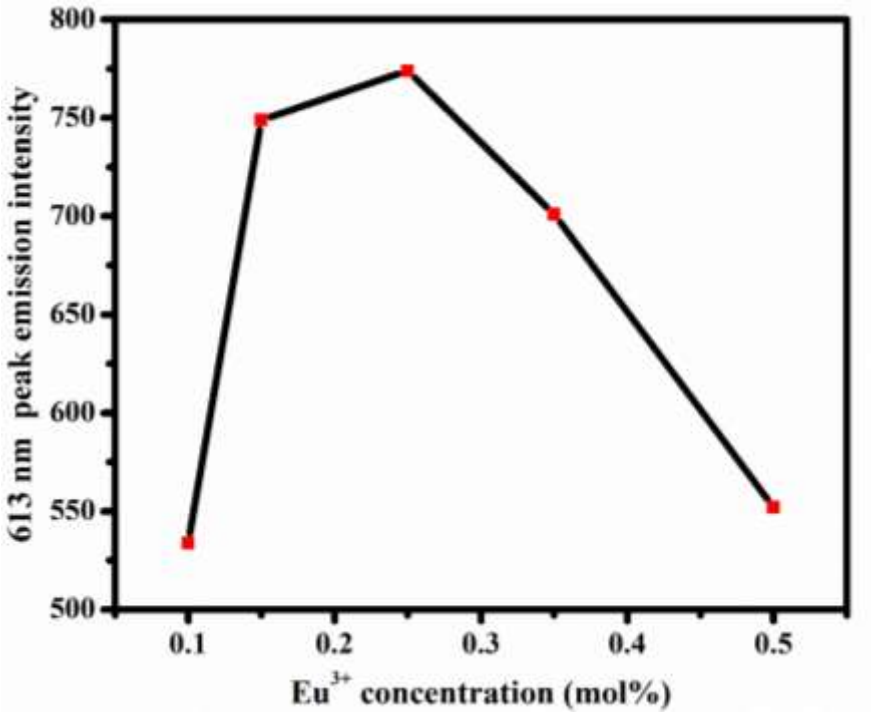

Figure 6.7 613 nm peak intensity as a function of Eu^{3+} concentration.

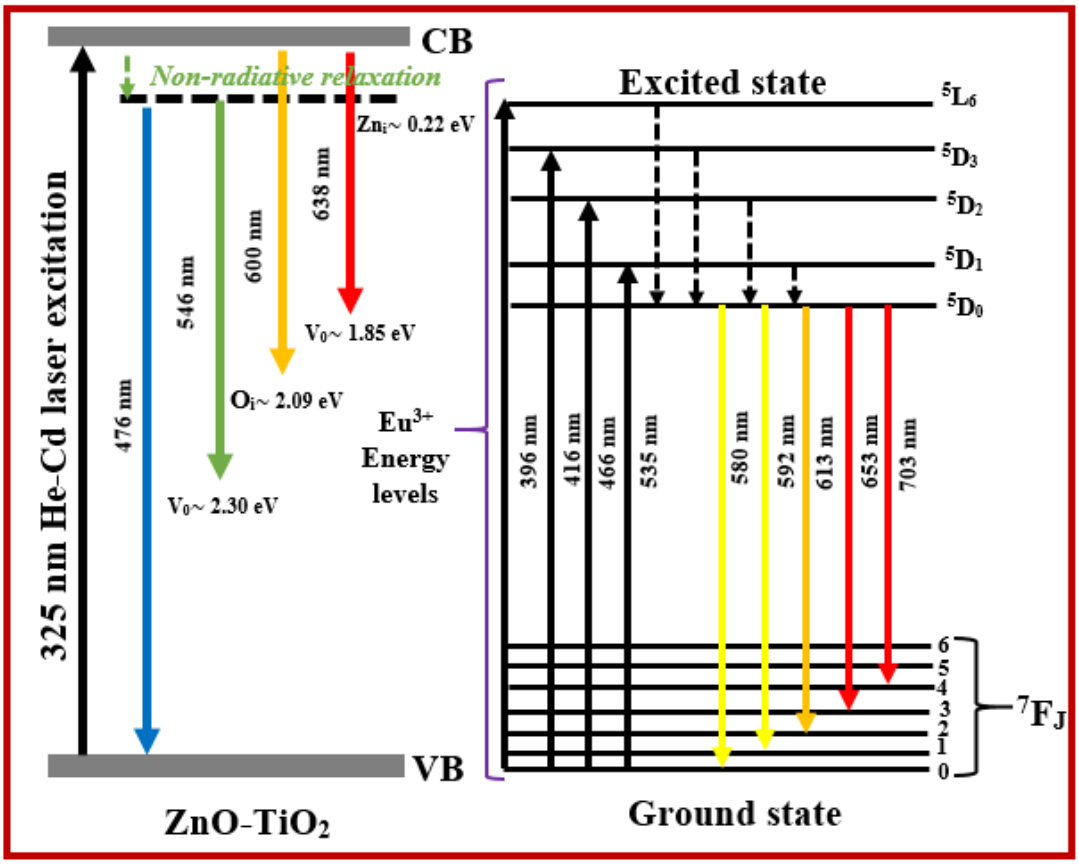

Figure 6.8 Schematic diagram of the energy level diagram for ZnO–TiO$_2$:Eu^{3+} nanocomposites.

6.4 Conclusion

ZnO-TiO$_2$ nanocomposites doped with Eu^{3+} ions has been successfully synthesized by sol-gel method. The nanocomposite showed presence of both wurtzite hexagonal ZnO phase and tetragonal TiO$_2$ phases as well as zinc titanium oxide ($ZnTiO_3$ and Zn_2TiO_4) phases. The morphology of these nanocomposites showed uniform structure of irregular shaped with some spherical shapes. The broad emission from undoped ZnO-TiO$_2$ nanocomposites in the range from 350 nm to 900 nm excited by He-Cd laser is due to the presence of different defects centres. The sharp intense red emission from Eu^{3+} doped ZnO-TiO$_2$ nanocomposites observed was excited by xenon lamp (excitation wavelength of 466 nm) which is attributed to the transition $^5D_0 \rightarrow {}^7F_2$ at 613 nm. An increase in concentration of Eu^{3+} enhanced the luminescence intensity and the concentration quenching effect was observed after 0.25 mol% Eu^{3+}.

6.5 References

[1] C.S. Lim. Journal of Ceramic Processing Research, 11(5) **(2010)** 631- 635. [2]. B.S. Richards. Solar Energy Materials & Solar cells, 90 **(2006)** 1189-1207.

[3] N. Yao, J. Huang, K. Fu, S. Liu, Y Wang, X. Xu, M Zhu and B. Cao. Journal of power sources, 267 **(2014)** 405- 410.

[4] P.Kr. Baitha and J. Manam. Optik - International Journal for Light and Electron Optics, **(2015)** 1-30.

[5] I. Cacciotti, F.R. Lamastra, A. Bianco, A. Speghini, F. Piccinelli, M.E. Fragala, G. Malandrino and G. Gusmano. Ceramic Materials, 62(4) **(2010)**, 516-520.

[6] R.E. Kroon. Nanoscience and the Scherrer equation versus the 'Scherrer–Gottingen equation'. S Afr J Sci. 2013:109(5/6), Art. #a0019, 2 pages. http://dx.doi. org/10.1590/sajs.2013/a0019.

[7] B.H. Soni, M.P. Deshpande, S.V. Bhatt, N. Garg and S.H. Chaki. Journal of Nano-and electronic physics, 5(4) **(2013)** 6.

[8] S. Moradi, P.A. Azar, S.R. Farshid, S.A. Khorrami, and M.H. Givianrad. International Journal of Chemical Engineering, 2012 **(2012)** 1-5.

[9] E. Rusu, V. Ursaki, T. Gutu, P. Vlaza and A.Sir. 3rd International Conference on Nanotechnologies and Biomedical Engineering, 55 **(2016)** 93-96.

[10] B. Keerthana, J. Madhavan and M.V.A. Raj. Scholars Research Library, 6 **(2014)** 50-55.

[11] A.K. Zak, A.M. Hashim and M. Darroudi. Nanoscale Research Letters, 9 (**2014)** 399.

[12] L.F. Koao, F.B. Dejene, R.E. Kroon and H.C. Journal of Luminescence, 147 **(2014)** 85–89.

[13] C. Shinho. Journal of the Korean Physical Society, 66(10) **(2015)** 1559 – 1563.

[14] J. Dhanaraj, R. Jagannathan, T. R. N. Kutty and C.H. Lu. J. Phys. Chem. B, 105 **(2001)** 11098-11105.

[15] O.M. Ntwaeaborwa, R.E. Kroon, V. Kumar, T. Dubroca, J.-P. Ahn, J.-K. Park and H.C. Swart. Journal of Physics and Chemistry of Solids, 70 **(2009)** 1438–1442.

[16] M. Pal, U. Pal, J.M.G.Y Jiménez and F.P. Rodríguez. Nanoscale Research Letters, 7 **(2012)** 1-12.

[17] M. Rajalakshmi, S. Sohila, S. Ramya, R. Divakar, C. Ghosh, S. Kalavathi. Optical Materials, 34 **(2012)** 1241–1245.

[18] X. Qin, L. Cui, and G. Shao. Journal of Nanomaterials, 2013 **(2013)** 1-5.

[19]. Y.H. Chang, C.M. Liu, C. Chen and H.E. Cheng. Journal of the Electrochemical Society, 159

(2012) 401-405.

[20] C. Ahn, Y.Y. Kim, D.C. Kim, S.K. Mohanta, H.K. Cho. J. Appl. Phys. 105 **(2009)** 2-6.

[21] X. Zeng, J. Yuan, and L. Zhang, J. Phys. Chem. C, 112 **(2008)** 3503-3508.

[22] B. Han, P. Li, J. Zhang, J. Zhang, Y. Xue, X. Suo, Q. Huang, Y. Feng, H. Shi. Materials Letters, 158 **(2015)** 208–210.

[23] Á.M. Ramírez, A.G. Murillo, F.J.C. Romo, M.G. Hernández, J.M. Palmerin and R.R. Guerrero. International Journal of Molecular Sciences, 12 **(2011)** 6240-6254.

[24] T. Homna, K Toda, Z.G. Yeb and M. S. J. Phys. Chem Solids. 59(8) **(1998)** 1187–1193

[25] A.N. Yerpude and S.J. Dhoble. Advanced Matterial Letter, 4(10) **(2013)** 792-796.

[26] T.K. Kundu, N. Karak, P. Barik and S. Saha. International Journal of Soft Computing and Engineering, 1 **(2011)** 19-24.

[287]. Y.H. Chang, C.M. Liu, C. Chen and H.E. Cheng. Journal of the Electrochemical Society, 159 **(2012)** 401-405.

[28] Vinod Kumar, S. Som, Vijay Kumar, Vinay Kumar, O.M. Ntwaeaborwa, E. Coetsee and H.C. Swart. Chemical Engineering Journal, 255 **(2014)** 541–552.

Chapter 7 Preparation and characterization of UV down-converting ZnO-TiO_2:Dy^{3+}/ Eu^{3+} nanocomposite

7.1 Introduction

Nowadays, research on novel nanocrystalline phosphor materials for up and down conversion in solar cells applications has been a subject of intense investigation [1]. To improve the efficiency of solar cells, special attention has been paid to down and up conversions from rare earth ions. A goal is to develop incident solar light converting phosphors pumped through ultra violet (UV) region and infrared (IR) region and capable of emitting in the visible region [2]. One of the best possible technique to enhance the solar cells is down conversion based on nanocomposites phosphors doped with rare earths ions which absorbs ultraviolet (UV) photons from the sun and down convert them into visible photons that can subsequently be absorbed by solar cells. Among available phosphor materials, nanocomposites based on semiconductors such as ZnO and TiO_2 in nanometre range are suitable host lattice for rare earth (RE) ions [3] to prepare UV down-converting phosphors.

ZnO and TiO_2 semiconductors have similar valence and conduction band positions, but they have different properties that are advantageous for different applications. ZnO have higher conductivity compared to TiO_2 while TiO_2 have higher chemical stability and reactivity, much higher dielectric constant and fewer defects states. Doping of ZnO and TiO_2 with rare earth materials gives the opportunity to tune the properties of each oxide in a controlled manner in order to enhance the performance of the solar cells. However, light at shorter wavelength can be used since the rare earths ions have the ability to absorb it and emit at longer wavelength [4, 5]. In this chapter, we investigate the energy transfer from Dy^{3+} to Eu^{3+} and study the role of down converter for possible application in solar cells. The energy transfer from Dy^{3+} to Eu^{3+} and the corresponding luminescence mechanism have been reported [6-9].

7.2 Materials and experimental procedure

$ZnO\text{-}TiO_2$:0.4 mol% Dy^{3+}, x mol% Eu^{3+} (x = 0.05, 0.15, 0.25, 0.50 and 0.75) were synthesized through sol-gel method. Analytical grade zinc acetate dehydrate ($Zn(CH_3COO)_2{\cdot}H_2O$), monoethanolamine (C_2H_7NO), titanium (IV) butoxide, nitric acid (HNO_3), lithium hydroxide (LiOH), europium acetate dehydrate ($Eu(CH_3COO)_3{\cdot}2H_2O$) and dysprosium acetate dehydrate ($Dy(CH_3COO)_3{\cdot}2H_2O$) were used. In a typical preparation, titanium (IV)-butoxide was dissolved in ethanol and the solution was stirred for 30 minutes to form what we refer to as solution 1. Nitric acid (70%) was added drop-wise in the solution as a catalyst followed by vigorous stirring for 2 hours. For the preparation of what we refer to as solution 2, zinc acetate dehydrate was dissolved in a mixture of ethanol and monoethanolamine at 60℃. The solution was stirred for 20 minutes. After one day of aging, the two solutions were combined followed by addition of Dy^{3+} and Eu^{3+} ions and the solution was stirred for 2 hours. The molar ratio of Ti: Zn was 1:1. Lithium hydroxide was added into a transparent solution followed by vigorous stirring at 80℃ for 1 hour and a gel was formed. Then, using an oven, the gel was dried at 90°C for 24 hours. The resulting rare-earth ions co-doped nanocomposites powders were annealed at 600°C for 2 hours.

7.3 Results and discussion

7.3.1 Structural analysis

The X-ray diffraction patterns of the undoped, Dy^{3+}/Eu^{3+} singly activated and Dy^{3+}-Eu^{3+} co-doped $ZnO\text{-}TiO_2$ nanocomposite phosphors are presented in Figure 7.1. The patterns showed peaks coming from wurtzite hexagonal ZnO and tetragonal TiO_2 (anatase and rutile) phases and were indexed using the JCPDS file number 36-1451 for ZnO, 86-1157 and 75-1753 for TiO_2 phases (anatase and rutile). There are peaks corresponding to zinc titanium oxides, namely $ZnTiO_3$ and Zn_2TiO_4, that are consistent with the JCPDS file numbers 26-1500 and 86-0158 respectively, suggesting that these secondary phases were formed. The hexagonal wurtzite ZnO shows dominant diffraction peaks in the nanocomposites compared to zinc titanium oxides and TiO_2 diffraction peaks. This can be due to the fact that TiO_2 had no effect on the crystal phase of ZnO during chemical reaction between ZnO and TiO_2 but results in the new formation of zinc titanium oxides phases in the nanocomposites.

It is known that incorporation of rare earth ions into TiO_2 could suppress the phase transformation from anatase to rutile in TiO_2. These phenomenon is attributed to the formation of Ti-O-rare earth ions bond by surrounding rare earth ions thereby stabilizing the anatase phase in TiO_2 [10]. Therefore, the anatase phase after doping nanocomposites in figure 7.1 was stabilized by Dy^{3+} and Eu^{3+} due to the formation of Ti-O-Dy^{3+} and Ti-O-Eu^{3+} bonds. In addition, there are impurities related peaks in the Dy^{3+}/Eu^{3+} co-doped ZnO/TiO_2 nanocomposites indicating the presence of the secondary phases of Eu_2O_3 (JCPDS, card number 34-0072) and Dy_2O_3 (JCPDS, card number 86-1327). It should be mentioned that co-doping with Eu^{3+} and Dy^{3+} resulted in the Eu_2O_3 and Dy_2O_3 secondary phases [11] due to possible oxidation reactions since the materials were prepared and annealed in air. In addition, undoped nanocomposites shows broad diffraction peaks while Eu^{3+} and Dy^{3+} co-doped nanocomposites shows sharp peaks suggesting that crystallinity has improved after doping. The ionic radii of both Eu^{3+} (0.95 Å) and Dy^{3+} (0.91 Å) are large compared to ionic radii of Ti^{4+} (0.61Å) and Zn^{2+} (0.74Å). Thus the improvement of the crystallinity may possibly due to minor fractions of the total amount of both rare earths (Eu^{3+} and Dy^{3+}) that goes into Ti^{4+} or Zn^{2+} interstitials sites whereby the most of the amount of these rare-earths reside on the surface or grain boundaries of the prepared nanocomposites [12].

The average crystallite size (*D*) of different nanocomposites shown in XRD were estimated using Scherrer's equation [13] given by

$$D = \frac{0.89\lambda}{\beta\cos\theta} \quad (1)$$

where *D* is the average crystallite size, λ the x-ray wavelength (0.15406 nm), θ the Bragg diffraction angle and β is a full width at half maximum (FWHM) of the diffraction peak. The crystallite sizes of ZnO/TiO_2 nanocomposites increased when rare earth (RE) ions where incorporated as shown in Table 7.1. The crystallite sizes was estimated from all diffraction peaks in the spectrum.

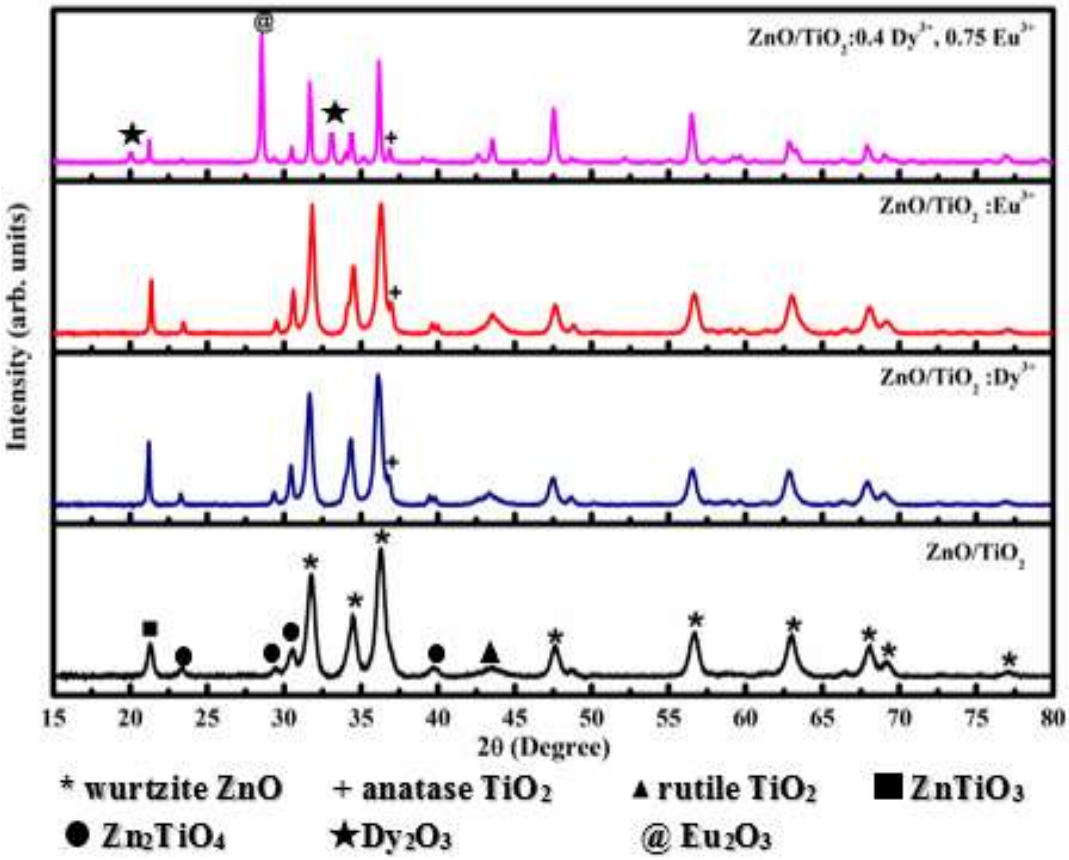

Figure 7. 1X-ray diffraction patterns of ZnO–TiO_2, ZnO–TiO_2:Dy^{3+}, ZnO–TiO_2:$Eu^{3+}$and ZnO–TiO_2:Dy^{3+}, Eu^{3+} nanocomposites annealed at 600℃.

Table 7.1 The average crystallites size of undoped, Dy^{3+} /Eu^{3+} singly doped and co-doped ZnO/TiO_2 nanocomposites.

ZnO/TiO_2 nanocomposites	Crystallites size (nm)
Undoped	13±3.18
Doped with Dy^{3+}	20±10.85
Doped with Eu^{3+}	19±5.028
Co-doped with Dy^{3+} and Eu^{3+}	35±12.32

7.3.2 Scanning Electron Microscopy Analysis

The morphology of undoped and Dy^{3+}/Eu^{3+} single doped and Dy^{3+}-Eu^{3+} co-doped ZnO-TiO_2 nanocomposites was studied with FE-SEM as shown in Fig.7.2. From the FE-SEM micrographs, it was found that ZnO–TiO_2 nanocomposites consist of faceted spheres and hexagons. Upon doping nanocomposites with Eu^{3+} ions did not affect the morphology of the nanocomposites as shown in figure 7.2 (b), suggesting that Eu^{3+} ions were well dispersed in the host lattice. However, it has been observed from Figure 7.2(c) and (d) that there are small spherical shapes residing on the surface of ZnO-TiO_2:Dy^{3+} and ZnO-TiO_2:Dy^{3+}, Eu^{3+} nanocomposites. It is reasonable to associate these nano encrustation with Dy^{3+} and conclude unlike Eu^{3+}, Dy^{3+} did not substitute and not occupy interstices but sat on the surface of the bigger grains.

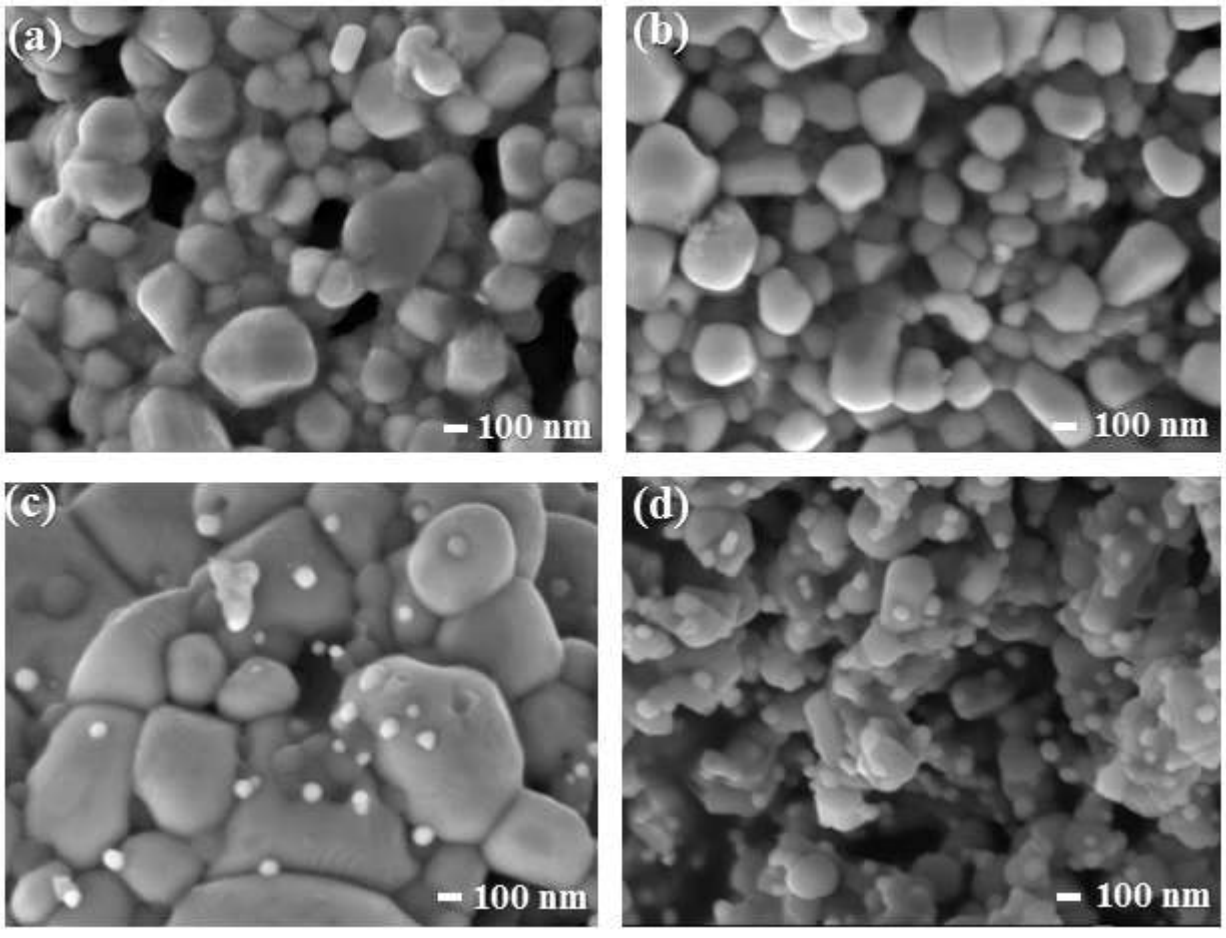

Figure 7. 2 FE-SEM micrographs (a) undoped ZnO–TiO_2, (b) ZnO–TiO_2: Eu^{3+}, (c) ZnO–TiO_2: Dy^{3+} and (d) Dy^{3+}/Eu^{3+} co-doped ZnO–TiO_2 nanocomposites.

Figure 7.3 demonstrates energy dispersive X-ray analysis to confirm the elemental composition of Dy^{3+} single doped and Eu^{3+}/Dy^{3+} co-doped ZnO-TiO_2 nanocomposites. The EDS spectra of Eu^{3+} doped ZnO-TiO_2 nanocomposites was reported in chapter 6. Based on the EDS analysis, it can be seen that the nanocomposites have all host elements (Zn and Ti) and rare earth elements (Eu and Dy) used as dopants in their appropriate weight percentage. The insets in the middle in figure 7.3(a) and (b) are the regions from FE-SEM micrographs where EDS analysis where performed and are marked S3, S4, S5, S6, S7 and S8. Figure 7.3 (a) is the comparison of EDS recorded at S3 and S4. S3 shows the presence of host elements together with Dy^{3+} ions while S4 show Dy^{3+} ions only. Thus this confirm that the small white spherical nanoparticles residing on the surface and grain boundaries of the prepared nanocomposites contain mainly Dy^{3+} ions. Figure 7.3(b) compares EDS spectrum recorded at position S7 and S8. The region of S6 and S8 is the same. The elemental contents of zinc (Zn) and oxygen (O) are approximately 65% and 30% at S7 and S8. Titanium (Ti) is approximately 5% and 15% at S7 and S8, respectively. In addition, europium (Eu) is approximately 2% at S7 while dysprosium (Dy) is approximately 10% at S8 respectively. These results confirm that Eu^{3+} and Dy^{3+} are homogeneously incorporated into the ZnO-TiO_2 nanocomposites. As can be seen in Figure 7.3(a), there are other additional elements detected by EDS. The carbon tape was used to mount the samples on the aluminum stub during measurements and the carbon which also give carbon signal in the EDS spectra. The aluminium signal might come from the aluminium stub used during the measurements. The characteristics X-rays of Na and Zn are 1.041 and 1.012 keV, whereas that one of As and Dy are 1.282 and 1.293 keV. Sodium (Na) and Arsenic (As) signals in EDS spectra may be due to overlapping with zinc (Zn) and dysprosium (Dy) because of the similar characteristic X-rays.

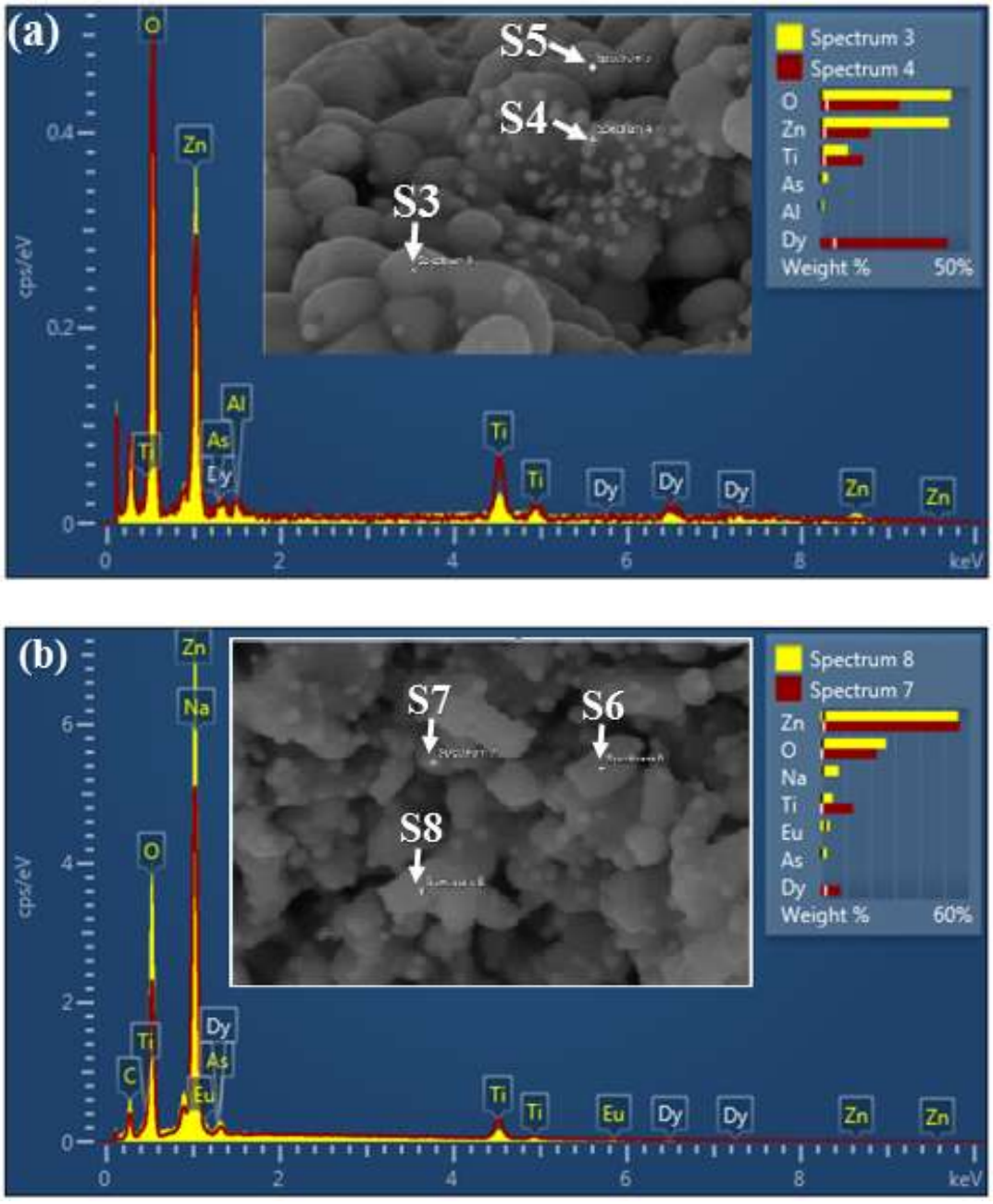

Figure 7.3 EDS spectra of (a) ZnO/TiO$_2$:Dy^{3+} and (b) ZnO/TiO$_2$:Dy^{3+}, Eu^{3+} nanocomposites. 'S' in the insets present spectrum, for example S3 means spectrum 3.

7.3.3 Optical properties

Figure 7.8 depicts the reflectance spectra of undoped and rare earth (Dy^{3+} and Eu^{3+}) ions single and co-doped ZnO-TiO_2 nanocomposites phosphor. The host and rare earth ions single doped and co-doped ZnO-TiO_2 nanocomposites show high reflectance in the visible region and a sharp decrease in reflectance in the region less than 400nm region which is attributed to electronic transition from ground states to the excited states of Zn^{2+} groups. There are sharp absorption bands in the range 400 - 900 nm, which are assigned to $f \rightarrow f$ characteristic absorptions of Eu^{3+} and Dy^{3+} ions such as $^7F_0 \rightarrow {}^5D_2$, $^5D_1$, $^5D_0$, $^5D_0$ of Eu^{3+} [14, 15] at 465, 534, 580 and 611 nm as well as $^6H_{15/2} \rightarrow {}^4G_{11/2}$, $^4I_{15/2}$, $^4I_{15/2}$, $^4F_{3/2}$, $^4F_{5/2}$, $^4F_{7/2}$ of Dy^{3+} ions [16-18]. The band gap energies was estimated with Tauc's plot method shown in equation (1) using reflectance spectra.

$$\alpha h\nu = A\,(h\nu - Eg)^{1/2} \quad (1)$$

where, A is constant, E_g is the optical band gap, h is Plank's constant and α is the absorption coefficient. The plot of this parameters were used to determine the band gap energies by extrapolating the linear portion to zero at the corresponding photon energy. The band gap energies of the nanocomposites are listed in table 7.2 and it was found that the band gap energies of undoped ZnO-TiO_2 nanocomposites decreases when Dy^{3+} and Eu^{3+} were incorporated.

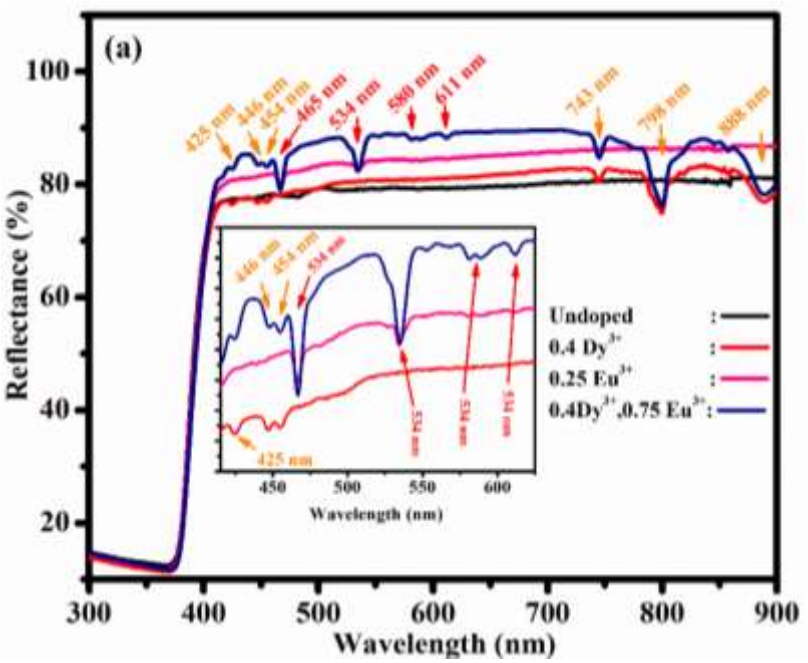

Figure 7.8 (a) Reflectance spectrum of ZnO-TiO_2 nanocomposites single doped and co-doped with Dy^{3+} and Eu^{3+}ions.

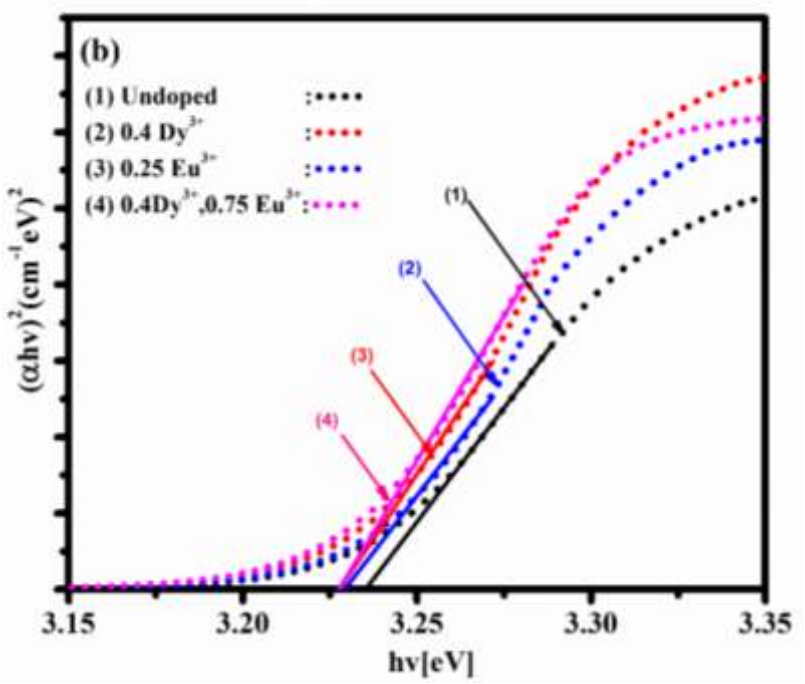

Figure 7.8 (b) Band gap energies of ZnO-TiO_2 nanocomposites single doped and co-doped with Dy^{3+} and Eu^{3+}ions.

The decrease of band gap energies with doping can be explained due to the overlapping of the wave-functions of electron that bound to the dopants as the density of states of the dopants increases. This overlap tend to force the energies to create energy levels just below the conduction band of ZnO in nanocomposite [19].

Table 7.2 The band gap energies of undoped, Dy^{3+} /Eu^{3+} single doped and co-doped ZnO/TiO_2 nanocomposites.

ZnO/TiO_2 nanocomposites	Band gap (eV)
Undoped	3.216
Doped with Dy^{3+}	3.211
Doped with Eu^{3+}	3.210
Co-doped with Dy^{3+} and Eu^{3+}	3.213

7.3.4 Photoluminescence analysis

The photoluminescent properties of undoped ZnO/TiO_2, Dy^{3+}/Eu^{3+} both single and co-doped ZnO/TiO_2 nanocomposites were recorded at room temperature. The PL spectra of undoped ZnO/TiO_2 nanocomposites were studied in details in chapter 6. Figure 7.6 depicts the PL excitation and emission spectra of Dy^{3+} and Eu^{3+} doped ZnO/TiO_2 nanocomposites. The excitation spectra from both figure 7.5 (a) and 7.5 (b) shows a strong broad band ranging from 200 nm to 300 nm which is well known as charge transfer band (CTB). These CTBs are assigned to Dy−O and Eu−O charge transfer, respectively. The absorption peaks from figure 7.5 (a) are assigned to $f \rightarrow f$ transitions of Dy^{3+}. The strong absorption peak at 456 nm is due to $^6H_{15/2} \rightarrow {}^4I_{15/2}$ transition and less intense absorption peaks at 398 nm, 426 nm, 470 nm and 480 nm are due to $^6H_{15/2} \rightarrow {}^4F_{7/2}$, $^4G_{11/2}$, $^4F_{9/2}$ and $^4F_{9/2}$ transitions of Dy^{3+}, respectively [20]. The emission spectra of ZnO/TiO_2: Dy^{3+} nanocomposites phosphor shows four simultaneous emission at 495 nm (blue), 583 nm (yellow), 673 nm (red) and 768 nm (red) corresponding to $^4F_{9/2} \rightarrow {}^6H_{15/2}$, $^6H_{13/2}$, $^6H_{11/2}$ and $^6H_{9/2}$ transitions of Dy^{3+} ions [21]. It is well known that blue emission (495 nm) and yellow emission (583) are the two prominent emissions of Dy^{3+} ions. Their emission intensity are employed for determination of the local host site surrounding the rare earth ions. The transition of blue emission peak of Dy^{3+} is associated with magnetic dipole transition, which means that it is strongly independent on the host. In addition, the transition of yellow emission peak of Dy^{3+} is associated with hypersensitive electric dipole transition and therefore it is strongly depends on the host. It should be noted that yellow emission in figure 7.5(a) is the dominant emission and this suggest that Dy^{3+} are residing in low symmetry site that lack inversion centre [20].

Figure 7.5 (b) shows the PL excitation and emission spectra of ZnO/TiO_2: Eu^{3+} nanocomposites. The excitation spectra exhibit sharp absorption peaks at 398 nm, 412 nm, 466 nm and 536 nm and they are assigned to $f \rightarrow f$ transitions of Eu^{3+} ions. This PL spectra was explained in detail in chapter 6. When the ZnO/TiO_2: Eu^{3+} nanocomposites was excited at 466 nm, five emission peaks at 580 nm (yellow), 593 nm (yellow), 613 nm (red), 652 nm (red) and 78 nm (red) assigned to $^5D_0 \rightarrow {}^7F_0$, $^7F_1$, $^7F_2$, $^7F_3$ and $^7F_4$ transition of Eu^{3+} were observed. The red emission at 613 nm is also known as a hypersensitive transition. Among weak emission peaks of Eu^{3+}, the emission peaks in the region 580 nm to 604 nm are associated with magnetic dipole transition peaks [20, 22].

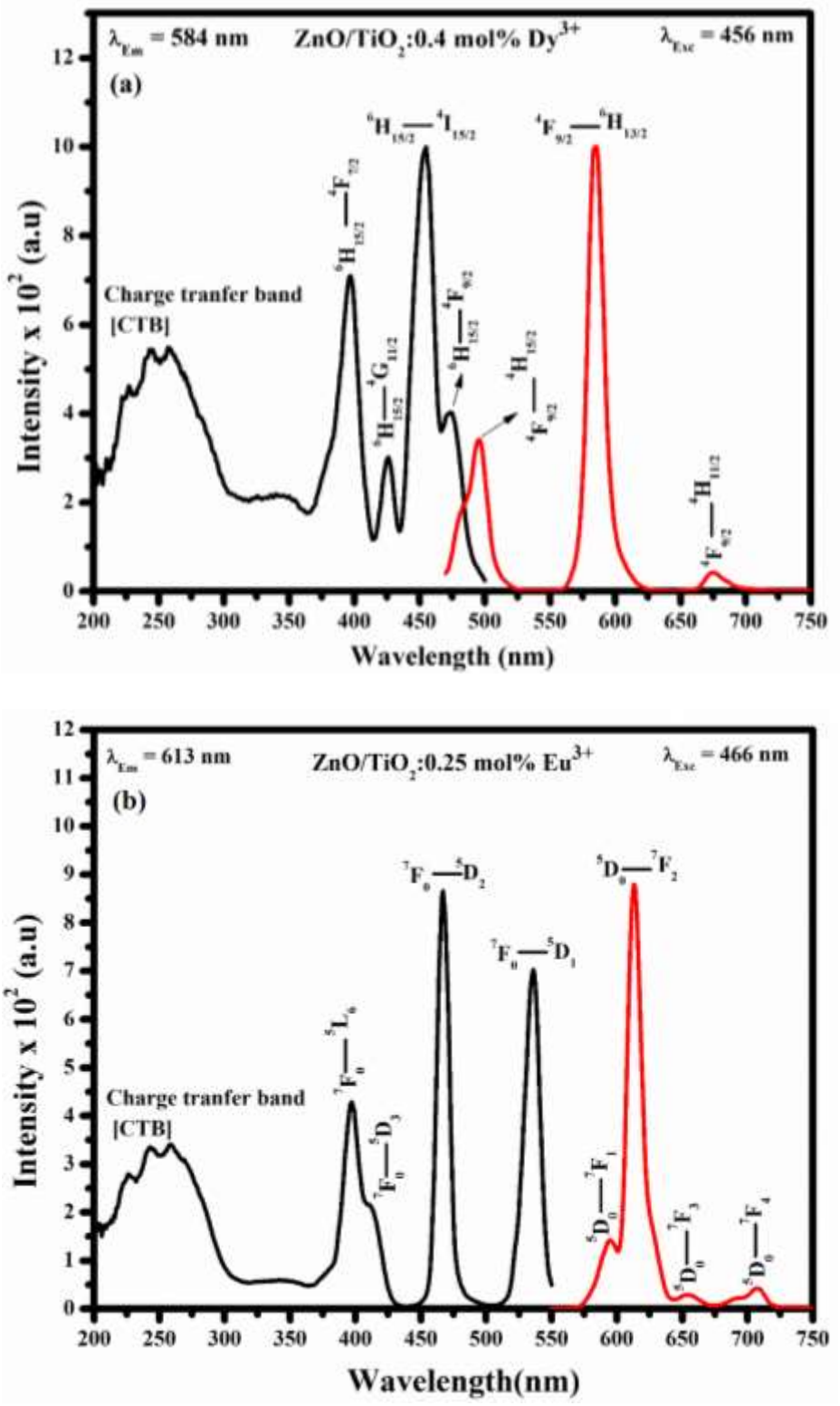

Figure 7.5 PL excitation emission of (a) $ZnO/TiO_2:Dy^{3+}$ and (b) $ZnO/TiO_2:Eu^{3+}$ nanocomposites.

The excitation spectrum of 0.4 mol% Dy^{3+}/0.75 mol% Eu^{3+} co-doped ZnO-TiO_2 nanocomposites phosphor for emission at 613 nm is shown in figure 7.6. The excitation spectrum consists of a broad band ranging from 200 nm to 310 nm which is well known as charge transfer band (CTB) and it assigned to the transition between O^{2-} ligands and rare-earth ($Eu^{3+}$and Dy^{3+}) co-activators 4*f* state [6,7]. There are narrow absorption peaks at 398 nm, 426 nm, 456 nm, 470 nm and 480 nm corresponding to the bands of both Eu^{3+} and Dy^{3+} co-activators and they are similar to those shown in figure 7.5 (a) and (b). The peaks centred 398 and 457 nm correspond to intrinsic *f*→*f* transitions, $^5F_0 \rightarrow {}^5L_6$ and $^5F_0 \rightarrow {}^5D_2$ of Eu^{3+} ions in the host, respectively [23, 24]. The peaks centred at 426,457, 470 and 480 nm are due to *f*→*f* transitions, $^6H_{15/2} \rightarrow {}^4G_{11/2}$, $^4I_{15/2}$, $^4F_{9/2}$ and $^4F_{9/2}$ of Dy^{3+} ions. In the excitation spectrum, Dy^{3+} ions contain more absorption bands than Eu^{3+} ions suggesting that Dy^{3+} can act as a sensitizer (energy donor) with Eu^{3+} as activator (energy acceptor) whereby there is a possible energy transfer that can proceed from Dy^{3+} to Eu^{3+} ions. Based on Dieke's energy level diagram, the energy transfer phenomenon among rare-earth ions from a sensitizer (donor) to an activator (acceptor) in phosphors may takes place through energy transfer between rare-earth ions with high fluorescence state and with low lying fluorescent states [8, 9].

The photoluminescence emission spectra for Eu^{3+}/Dy^{3+} co-doped ZnO-TiO_2 nanocomposites excited at 248 nm is shown in figure 7.6 (a) for various Eu^{3+} concentrations at fixed concentration of Dy^{3+} (0.4 mol%). As can be seen in figure 7.6 (a), four emissions bands centred at 496, 584, 593 and 614 nm were observed. The first two emission peaks centred at 496 nm and 584 nm are assigned to $^4F_{9/2} \rightarrow {}^6H_{15/2}$ and $^4F_{9/2} \rightarrow {}^6H_{13/2}$ *f*→*f* transitions of Dy^{3+} transitions. The other two emission peaks centred at 593 nm and 614 nm are assigned to $^5D_0 \rightarrow {}^5F_1$ and $^5D_0 \rightarrow {}^5F_2$ *f*→*f* transitions of Eu^{3+} activator, respectively [8]. From figure 7.6 (b) and the inset in figure 7.6 (a), it can be seen that intensity of the of two emissions transitions of Eu^{3+} ions ($^5D_0 \rightarrow {}^5F_1$ and $^5D_0 \rightarrow {}^5F_2$) increase whereas that of Dy^{3+} ions ($^4F_{9/2} \rightarrow {}^6H_{15/2}$ and $^4F_{9/2} \rightarrow {}^6H_{13/2}$) are simultaneously found quenching with increasing concentration of Eu^{3+}. Figure 7.8 depicts the decay curves Dy^{3+} ions in the ZnO-TiO_2: Dy^{3+},Eu^{3+} nanocomposites. The curve pattern show very small differences suggesting that the lifetimes of Dy^{3+} did not decrease. Therefore it is safe to conclude that there was no energy transfer from Dy^{3+} to Eu^{3+}. We therefore attribute energy transfer from charge transfer bands (CTB) to Dy^{3+} and Eu^{3+} ions as explained in figure 7.9. The fact that there is no energy transfer between Dy^{3+} and Eu^{3+} shows that the increase in the PL emission of Eu^{3+} was a function of doping concentration as observed in chapter 6.

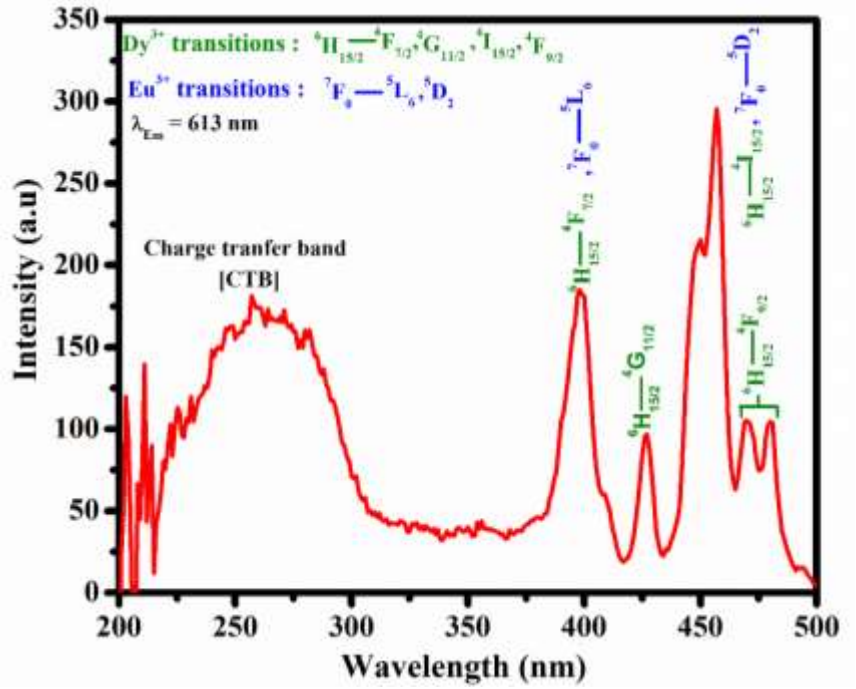

Figure 7.6 Excitation spectra of Eu^{3+}/Dy^{3+} co-doped ZnO-TiO_2 nanocomposites.

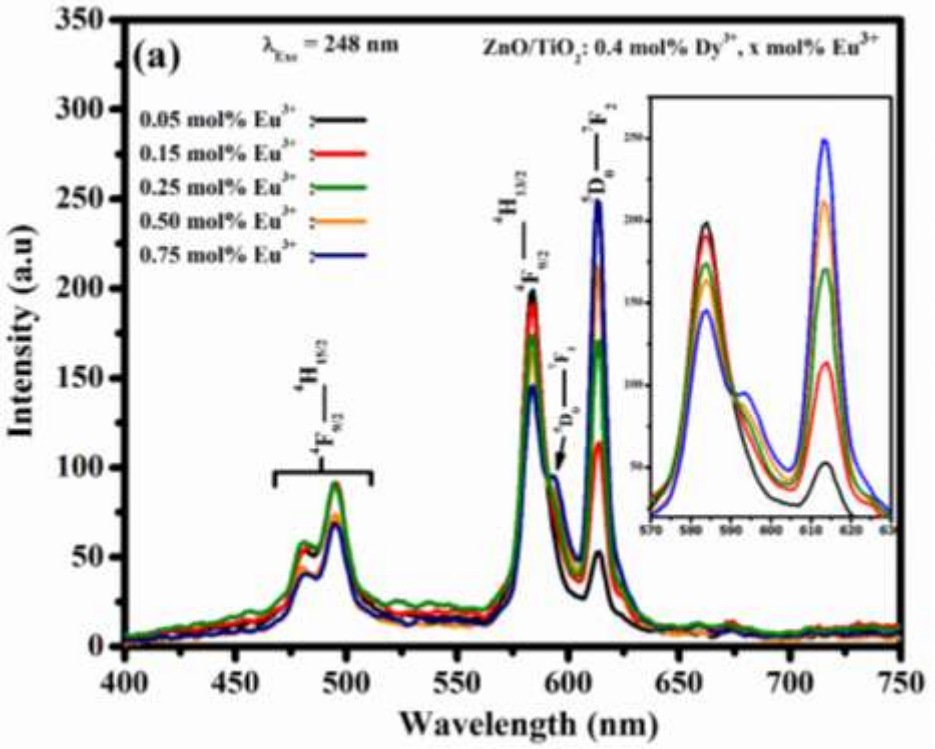

Figure 7.7 (a) PL emission spectra of Eu^{3+}/Dy^{3+} co-doped ZnO-TiO_2 nanocomposites for different concentration of Eu^{3+} ions doping for 248 nm excitation.

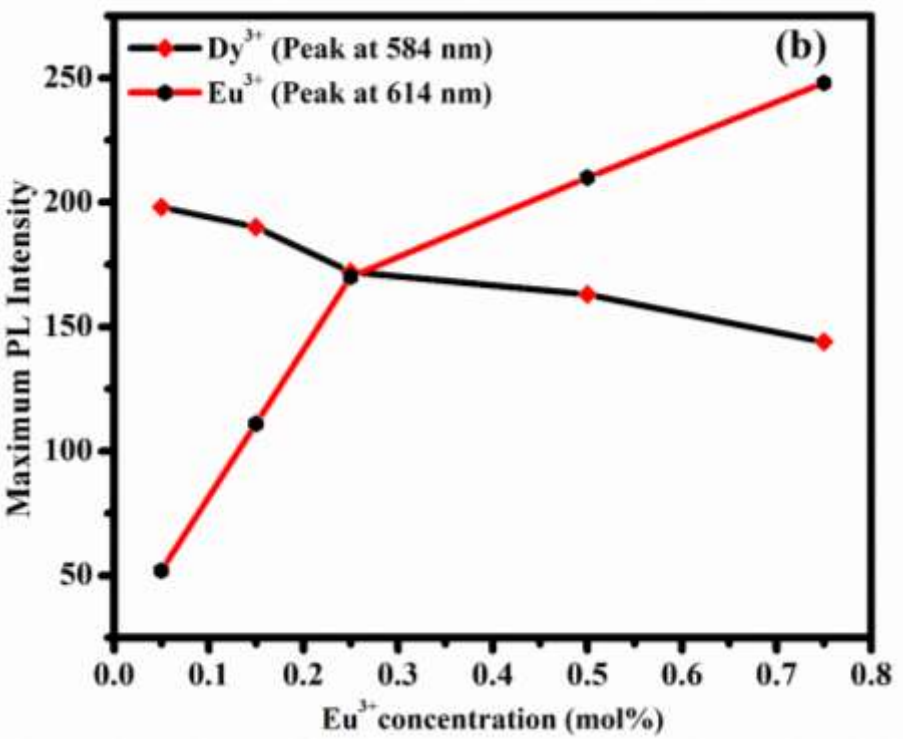

Figure 7.7 (b) Concentration-dependent emission intensity of Eu^{3+}/Dy^{3+} co-doped ZnO-TiO_2 nanocomposites for different concentration of Eu^{3+} ions doping for 248 nm excitation.

The possible mechanism of energy transfer occurring in Dy^{3+}/Eu^{3+} co-doped ZnO-TiO_2 nanocomposites phosphors is shown in figure 7.8. Both $O \rightarrow Eu^{3+}/Dy^{3+}$ charge transfer band and Zn^{2+}/Ti^{4+} groups make contributions to the emission of Eu^{3+} and Dy^{3+} ions when ZnO-TiO_2: Eu^{3+}/Dy^{3+} nanocomposites were excited at 248 nm. The excitation wavelength 248 nm raises electrons from O2p valence to the Eu^{3+}/Dy^{3+} (5d6s) conduction band and then electrons get back to lower energy levels once again by transferring energy to Eu^{3+} and Dy^{3+} ions. Similarly, transition from ground state of Zn^{2+}/Ti^{4+} groups to the excited state take place and the excited electrons are then trapped through non-radiative decay process and the Zn^{2+}/Ti^{4+} groups transfer energy to Eu^{3+} and Dy^{3+} ions in the de-excitation process. The transferred energy in the highest energy state of Dy^{3+} relax to $^4F_{9/2}$ state through non-radiative decay which is then decay radiatively to $^6H_{15/2}$ and $^6H_{13/2}$ states. Similarly, energy at the highest energy state of Eu^{3+} is then relaxes to intermediate $^5D_0$ state and finally decay radiatively to $^7F_1$ and $^7F_2$ states.

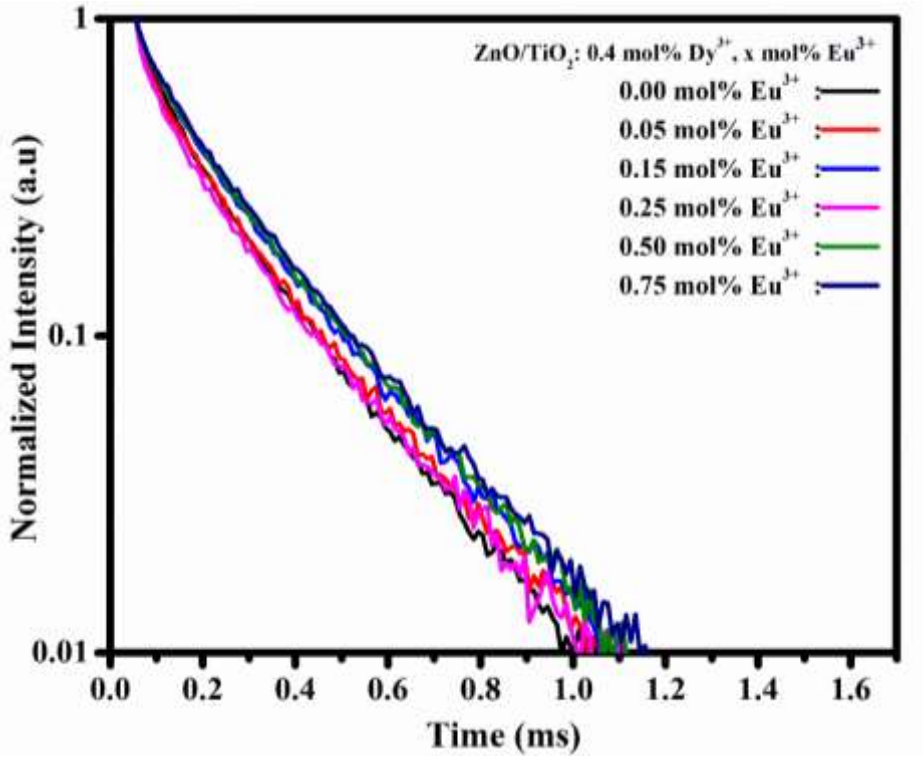

Figure 7.8 Decay curves of luminescence of Dy^{3+} ions in ZnO–TiO_2: Eu^{3+}/Dy^{3+} nanocomposites.

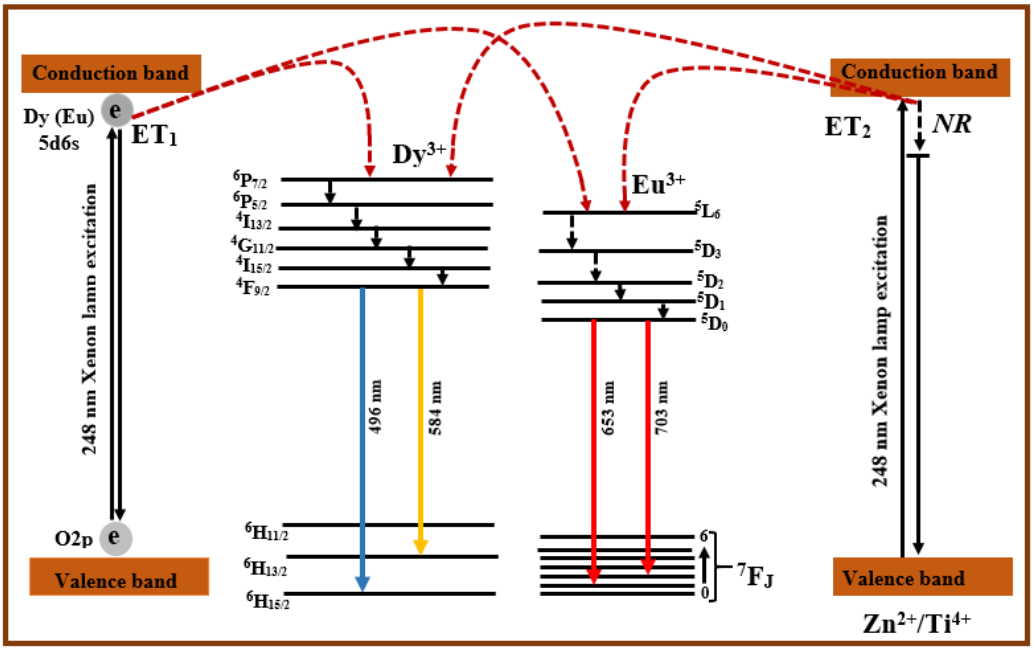

Figure 7.9 Schematic diagram of the energy level diagram for ZnO–TiO_2: Eu^{3+}/Dy^{3+} nanocomposites. ET and NR is the energy transfer and non-radiative decay.

7.4 Conclusion

The undoped and Eu^{3+}/ Dy^{3+} co-activates ZnO-TiO_2 nanocomposites were successfully synthesized by the sol-gel method. XRD results indicate that the reaction between ZnO and TiO_2 results in the formation of new phases of zinc titanium oxide, namely $ZnTiO_3$ and Zn_2TiO_4. The luminescence spectra (excitation and emission) have been recorded for Eu^{3+}/ Dy^{3+} co-doped ZnO-TiO_2 nanocomposites to investigate the potential of Eu^{3+} and Dy^{3+} for down conversion. The results shows that Dy^{3+} emissions quenched and Eu^{3+} emissions increased due to Eu^{3+} concentration and this shows lack of energy transfer from Dy^{3+} to Eu^{3+} in Eu^{3+}/ Dy^{3+} co-doped ZnO-TiO_2 nanocomposites. Comparing the relative intensities for the $^4F_{9/2} \rightarrow {}^6H_{13/2}$ and $^5D_0 \rightarrow {}^5F_2$ emissions spectra confirm that down conversion is not efficient for this lanthanides couple in ZnO-TiO_2 nanocomposites as a host.

7.5 References

[1] N. Enteria, H. Yoshino, R. Takaki, A. Mochida, A. Satake, S. Baba, H. Ishihara, R. Yoshie. Solar energy, 105 **(2015)** 243 – 263.

[2] T. Trupke, M. Green, and P. Würfel, Journal of applied physics. 92 **(2002)**1668.

[3] S.C. Singh, D.P. Singh, J. Singh, P.K. Dubey, R.S. Tiwari and O.N. Srivastava. pp. 2-167.

[4] L.Z.R. Hoye, K.P. Musselman and J.L. MacManus-Driscoll. APL materials, 1 **(2013)** 060701.

[5] J.A. Noor, A. Madzlan and R.M.Y. Abdul. Prosiding Seminar Kimia Bersama UKM-ITB VIII (**2009)** 339 - 347.

[6] Y. Liu, G. Liu, X. Dong, J. Wang and W. Yu. Royal society of chemistry, 17 **(2015)** 1-7.

[7] P. Du and J.S. Yu. Journal of alloys and compounds, 653 **(2015)** 468-473.

[8] D. Rajesh, K. Brahmachary, Y.C. Ratnakaram, N. Kiran, A.P. Baker and G.G. Wang. Journal of alloys and compounds, 646 **(2015)** 1096-1103.

[9] H. Guan, G. Liu, J. Wang, X. Dong and W. Yu. Royal Society of Chemistry, 38 **(2014)** 4901.

[10] S. Dongfeng, W. Kai, X. Zhijian and L. Ruixing., Journal of rare earths, 33(5) **(2015)**P.491

[11] Vinod Kumar, Vijay Kumar, S. Som, M.M. Duvenhage, O.M. Ntwaeaborwa and H.C. Swart. Applied Surface Science, 308 **(2014)** 419–430.

[12] F. Gu, S.F. Wang, M.K Lu¨, G.J. Zhou, D. Xu, and D.R. Yuan. American Chemical Society, 20 **(2004)** 3528-3531.

[13] R.E. Kroon. Nanoscience and the Scherrer equation versus the 'Scherrer–Gottingen equation'. S Afr J Sci. 2013:109(5/6), Art. #a0019, 2 pages. http://dx.doi. org/10.1590/sajs.2013/a0019.

[14] T.B. Iveti´c, M.R. Dimitrievska, I.O. Gu´th, Lj.R. -Da˘canin and S.R. Luki´c-Petrovi´c, 36(1) **(2012)** 43 – 51.

[15] L.F. Koao, F.B. Dejene, R.E. Kroon and H.C. Journal of Luminescence, 147 **(2014)** 85–89.

[16] Z.W. Zhang, A.J. Song, Y. Yue, H. Zhong, X.Y. Zhang, M.Z. Ma and R.P. Liu. Journal of Alloys and Compounds, 650 **(2015)** 410- 414.

[17] J. Feng, H.J. Zhang, S.Y. Song, Z.F. Li, L.N. Sun, Y Xhing and X.M. Guo. Journal of Luminescence, 128 **(2008)** 1957-1964.

[18] D.C. Yu, S. Ye, M.Y. Peng, Q.Y. Zhang,J.R. J. Wang and L. Wondraczek. Solar Energy Materials and Solar Cells, 95 **(2011)** 1590 – 1593.

[19] P.Kr. Baitha and J. Manam. Optik, 126 **(2015)** 4916–4923.

[20] T.Q. Leow, R. Hussin, Z. Ibrahim, K. Deraman, W.N.W. Shamsuri and H.O. Lintang. Sains

Malaysiana, 44(5) **(2015)** 753–760.

[21] M.R. Dousti and S.R. Hosseinian. Journal of Luminescence, 154 **(2014)** 218–223.

[22] K. Lemański, M. Stefański, D. Stefańska and P.J. Dereńn. Journal of Luminescence, 159 **(2015)** 219–222.

[23] X. Zeng, J. Yuan, and L. Zhang, J. Phys. Chem. C, 112 **(2008)** 3503-3508.

[24] B. Han, P. Li, J. Zhang, J. Zhang, Y. Xue, X. Suo, Q. Huang, Y. Feng, H. Shi. Materials Letters, 158 **(2015)** 208–210.

Chapter 8 Summary and conclusion

8.1 Summary and conclusion

In this thesis, $TiO_2:Eu^{3+}$ and $ZnO:Eu^{3+}$ nanoparticulate phosphors were prepared by co-precipitation method with different concentration of Eu^{3+} ions. Furthermore, sol-gel preparation of $ZnO/TiO_2:Eu^{3+}$ and $ZnO\text{-}TiO_2:Dy^{3+},Eu^{3+}$ nanocomposites phosphor with different concentration of Eu^{3+} ions have been reported. The structure and morphology of all samples were analyzed using XRD and FE-SEM. The photoluminescent properties were recorded by a 325 nm He-Cd laser and a Cary Eclipse fluorescence spectrophotometer. UV-Vis spectrometer was used to measure the diffuse reflectance of nanoparticulate and nanocomposite phosphors. Stretching vibrations were recorded using Fourier Transform Infrared (FTIR) spectroscopy.

The tetragonal anatase and rutile phases of $TiO_2:Eu^{3+}$ nanoparticulate phosphor were observed from XRD pattern and the morphological properties of TiO_2 showed nanorod structures with average length and diameter of approximately 410 and 73 nm. The hexagonal wurtzite structure form of ZnO was confirmed by XRD. However, the morphological properties of ZnO showed an agglomerated flake-like nanostructures and changed to oval-like shaped by incorporation of Eu^{3+} ions. The XRD from the $ZnO–TiO_2$ nanocomposites prepared by sol-gel method confirmed new phases in the nanocomposites, suggesting that the secondary phases were formed. $ZnO–TiO_2$ nanocomposites activated with Eu^{3+} did not influence the morphology of undoped nanocomposite but single activated with Dy^{3+} and co-activated with Dy^{3+} and Eu^{3+} showed small spherical shaped particles residing on the surface of nanocomposites. One can therefore conclude that these spherical nanoparticles are associated with Dy^{3+} ions whereby they lie on the surface of bigger grain boundaries unlike Eu^{3+} ions that are well dispersed in the host lattice.

For 325 nm He-Cd laser excitation, the emission spectra TiO_2 nanoparticulate phosphor showed a broad emission from 350 to 800 nm which we associated with surface states, radiative recombination of self-trapped excitons and oxygen vacancies. From PL spectra of ZnO nanoparticulates we observed broad emission with strong deep level emission (DLE) and weak exciton emission. The strong emission of ZnO were attributed to different kinds of defects. The luminescent properties of Eu^{3+} activated TiO_2, ZnO and ZnO–TiO_2 nanocomposites were investigated and the nanocomposites were excited at 466 nm. The excitation and emission spectra showed absorption and emissions attributed to $f \rightarrow f$ transitions of Eu^{3+} ions. An increase in Eu^{3+} concentration enhanced the emission intensity of Eu^{3+} and decrease at some point due to concentration quenching effects. Photoluminescence from ZnO–TiO_2:Dy^{3+}, Eu^{3+} nanocomposites showed the simultaneous emissions attributed to both Dy^{3+} and Eu^{3+} ions. An increase in Eu^{3+} concentration enhanced emission of Eu^{3+} and subsequently decreased the emission of Dy^{3+} pointing to the occurrence of energy transfer from Dy^{3+} to Eu^{3+}. We can therefore conclude that Dy^{3+} is a good sensitizer for Eu^{3+} ions.

The optical properties of the samples were investigated and it was found that nanoparticulate and nanocomposites phosphors exhibited strong absorptions that are attributed to interband transitions. Eu^{3+} activated TiO_2 and ZnO nanoparticulate phosphors showed $f \rightarrow f$ absorptions of Eu^{3+} in the visible region in addition to strong absorption of TiO_2 and ZnO. Similarly, UV-Vis reflectance from ZnO–TiO_2:Dy^{3+}, Eu^{3+} nanocomposites showed $f \rightarrow f$ absorptions of both Eu^{3+} and Dy^{3+} in the visible region in addition to strong absorption of ZnO. The band gaps was estimated using Tauc's plot. When evaluating the effect of Eu^{3+} and Dy^{3+}, the band gaps increased and decreased respectively. Energy transfer did not occur from Dy^{3+} to Eu^{3+} in ZnO-TiO_2 nanocomposites. In conclusion, the results imply that these phosphors are not suitable for down-conversion improvement of solar cells.

8.2 Future work

Future work will be done on the ZnO–TiO_2:Dy^{3+}, Eu^{3+} nanocomposites by sol-gel method. The XRD analysis on the nanocomposites phosphor prepared by sol-gel method showed high crystalline of ZnO in the nanocomposite, therefore it is important to vary the molar ratio that is

expected to influence the crystallinity of both ZnO, TiO_2 and ZnO-TiO_2 nanocomposites. This would assist in determining whether or not the composite can be a good host for down-conversion method. Furthermore it is imperative to investigate the effects of temperature on the emission intensity and the rate of energy transfer from Dy^{3+} to Eu^{3+} and compare the results with the ZnO–TiO_2:Dy^{3+}, Eu^{3+} nanocomposites that were reported in this study. A further synthesis of other nanocomposites host doped with Dy^{3+} and Eu^{3+} ions for down-conversion method. The study could also be extended on the energy transfer from Dy^{3+} ion to other rare earths ions in order to efficiently down-convert UV light to visible light. Future work will also include varying the Dy^{3+} concentration (fixed in this study) and also varying the Ti:Zn ratio of the nanocomposites (also fixed in this study) and also applying the phosphor to Si solar cells to assess the change in efficiency.